MEASURING THE GROWTH OF STRUCTURE WITH MULTI-WAVELENGTH SURVEYS OF GALAXY CLUSTERS

BY NEELIMA SEHGAL

A dissertation submitted to the

Graduate School—New Brunswick

Rutgers, The State University of New Jersey

in partial fulfillment of the requirements

for the degree of

Doctor of Philosophy

Graduate Program in Physics and Astronomy

Written under the direction of

Professor John P. Hughes

and approved by

_____

_____

_____

_____

_____

New Brunswick, New Jersey

May, 2008

ABSTRACT OF THE DISSERTATION

Measuring the Growth of Structure with Multi-Wavelength Surveys of Galaxy Clusters

by Neelima Sehgal

Dissertation Director: Professor John P. Hughes

Current and near-future galaxy cluster surveys at a variety of wavelengths are expected to provide a promising way to obtain precision measurements of the growth of structure over cosmic time. This in turn would serve as an important precision probe of cosmology. However, to realize the full potential of these surveys, systematic uncertainties arising from, for example, cluster mass estimates and sample selection must be well understood. This work follows several different approaches towards alleviating these uncertainties.

Cluster sample selection is investigated in the context of arcminute-resolution millimeter-wavelength surveys such as the Atacama Cosmology Telescope (ACT) and the South Pole Telescope (SPT). Large-area, realistic simulations of the microwave sky are constructed and cluster detection is simulated using a multi-frequency Wiener filter to separate the galaxy clusters, via their Sunyaev-Zel'dovich signal, from other contaminating microwave signals. Using this technique, an ACT-like survey can expect to obtain a cluster sample that is 90% complete and 85% pure above a mass of $3 \times 10^{14} M_{\odot}$.

Cluster mass uncertainties are explored by comparing X-ray and weak-lensing mass estimates for shear-selected galaxy clusters in the Deep Lens Survey (DLS) to study possible biases in using cluster baryons or weak-lensing shear as tracers of the cluster total mass. Results are presented for four galaxy clusters that comprise the top-ranked shear-selected system in the DLS, and for three of these clusters there is agreement between X-ray and weak-lensing mass estimates. For the fourth cluster, the X-ray mass estimate is higher than that from weak-lensing

by 2σ and X-ray images suggest this cluster may be undergoing a merger with a smaller cluster, which may be biasing the X-ray mass estimate high.

The feasibility of measuring galaxy cluster peculiar velocities using an ACT-like instrument is also investigated. Such a possibility would allow one to measure structure growth via large-scale velocity fields and circumvent the uncertainties associated with measuring cluster masses. We show that such measurements are possible and yield statistical uncertainties of roughly 100 km/sec given either a temperature prior with 1σ errors of less than 2 keV or additional lower frequency millimeter-band observations.

Acknowledgements

I have undergone a transformation while at Rutgers both professionally and personally, and I have many many people to thank for their influence and support.

I must start at the beginning with Jessica Warren, Karen Spaleta, Jackie Bondell, and the card game Euchre. There is no way I would have gotten through the first year (or the qualifying exams) without them. I have seen each change their last names and their lives since that first year, and they are fully intertwined with my memories of this place.

I am also grateful for endless dinner parties which made every frustration bearable. Thank you Matthew, Meredith, Eric, Daibhid, Jackie, Howie, Jes, Aaron, Karen, and Jef.

I would like to thank Ruadhan O′Flanagan and Gia Peradze who helped me navigate my detour into string theory and Arthur Kosowsky who first opened my eyes to research in cosmology. I am also especially grateful for Arthur's initial faith in me and continued support throughout this process.

I need to acknowledge the people of 10 Handy Street for giving me a welcome home away from home, Anita McLean for her continual wisdom, and Diane Soyak for her continual kindness.

This thesis would be nothing without my collaborators so I must thank Gil Holder for being a great person to work with on a first project and Kevin Huffenberger who generously shared his knowledge. I would also like to thank Hy Trac, Paul Bode, and Dave Wittman who made working with them a pleasure.

I am also deeply appreciative of the guidance provided by Jack Hughes. I thank him for showing me how to reduce X-ray data, write grant proposals, and for having enough confidence in me to allow me to steer my own course. I would also like to thank Jerry Sellwood, Terry Matilsky, Ted Williams, and Tad Pryor for always being available to answer questions or lend a hand.

The astro grad offices would not have been nearly as much fun without Juntai Shen, Ricardo Sanchez, Kristine Spekkens, Matthew Francis, Carlos Badenes, and Ross Fadely. But most especially I am indebted to Jessica Warren and Naseem Rangwala, whose laughter and friendship has enriched each day.

Sincerest thanks to Eric Gawiser, Andrew Baker, Chuck Keeton, and Saurabh Jha for invaluable postdoc advice, to the high-energy theory grad students for being my second grad student family, and to the various flight instructors at Princeton Airport who made clear skies on weekends so much better.

I must also thank Toby Marriage, Amir Hajian, and Sudeep Das for their continued collaboration and support on ACT research, and Lyman Page and David Spergel for allowing me every opportunity at Princeton. I am especially grateful to David Spergel for his support and encouragement.

I thank my sister, Sheetal Sehgal, for her good-heartedness and my high-school physics teacher, Doc, for first making physics fun. I also thank my virtual mother, Linda Champagnie, for her ever-open arms, and my parents for setting a good example with their careers and allowing me to believe I could be just as capable.

Lastly, I would like to thank Rouven Essig for showing up at the right time and brightening the rest of my journey.

Dedication

For Rouven

Table of Contents

List of Tables

List of Figures

Chapter 1
Introduction

1.1 The Growth of Structure: a New Precision Probe of Cosmology

Measuring the growth of structure over cosmic time has the potential to open a new window through which we can view and understand the nature of our Universe. Current precision probes of cosmology, such as the primordial microwave background radiation, type Ia supernovae, and galaxy surveys, measure the expansion rate of the Universe. Since general relativity provides a relation between the expansion rate of the Universe and its matter and energy content, these measurements have informed us about our Universe's dark sector. We have learned that at present the expansion of the Universe is accelerating, which implies one (or more) of the following three possibilities: Either the Universe is currently dominated by a dark energy field with negative pressure, or there is a non-zero cosmological constant, or general relativity is incorrect on the largest scales. However, measurements of the expansion rate alone are not able to distinguish between an additional component of our Universe (dark energy/cosmological constant) and a failure of general relativity.

The primordial soup of our infant Universe also consisted of small density fluctuations, which gave rise to the temperature fluctuations we observe in the microwave background. As the Universe cooled and expanded, these density fluctuations grew. The growth rate of these structures was determined by both gravitational collapse, which accelerated their growth, and the expansion rate, which suppressed it. General relativity provides a relation between the growth rate of structure and the expansion history of the Universe. Since the density fluctuations of the infant Universe are accurately determined by microwave background observations, measuring the subsequent amplitude of matter fluctuations probes structure growth and provides an additional observable through which we can measure the properties of the dark sector. Most importantly, any inconsistency between the cosmological parameters implied by the growth of structure and those inferred from previous observations of the expansion rate would signal a breakdown of the underlying general relativity theory (Wang et al. 2007; Albrecht et al. 2006, and references therein). Whether these observations confirm a dark energy component of our

Universe or uncover a flaw in our theoretical understanding of gravity, a fundamental revision of our foundational theories of physics will be required.

1.1.1 Techniques for Measuring the Growth Rate of Structure

Currently there are two promising techniques that can be used to precisely measure structure growth. One is to use large-area surveys of galaxy clusters to observe the evolution over cosmic time of the number density of galaxy clusters as a function of their mass. This technique has several advantages. Galaxy clusters are large enough that their number abundance can still be predicted by linear perturbation theory, and techniques to measure their redshift and mass using multiple observables across the electromagnetic spectrum are well established. Moreover, X-ray, optical, and microwave surveys of galaxy clusters are already underway and much data is already in hand or will be available shortly. However, there are possible hurdles that need to be overcome in order to realize the full potential of cluster surveys, with systematic errors arising from, for example, cluster mass estimates and the cluster selection function.

The other promising technique is to measure the cosmic shear from weak gravitational lensing using optical surveys of galaxies. This allows one to map out the mass distributions between us and the most distant visible galaxies in the survey. This technique relies on measuring the apparent distortion of distant galaxy shapes, statistically averaged over many galaxies, caused by the gravity of the intervening matter. These surveys have the advantage that the cosmic-shear pattern can be measured in several ways, and this makes it possible to detect and to correct for many potential sources of systematic error by the internal comparison of different observables (Albrecht et al. 2006, and references therein). However, weak-lensing surveys still have other systematic errors that are harder to correct for, such as the biases in photometrically-derived redshifts. Moreover, the data from these large-area surveys is projected to become available on a longer timescale (five to ten years). Cosmic-shear observations will nonetheless be an important cross-check of current cluster surveys.

1.2 Measuring Structure Growth with Galaxy Cluster Surveys

My thesis research has focused on measuring the growth of structure using the galaxy cluster data currently available or near at hand from cluster surveys. My work makes progress towards understanding the main sources of systematic uncertainty that plague cluster surveys so that they can be utilized as precision cosmological probes.

In Chapters 2 and 4, I focus on millimeter wavelength cluster surveys like those being

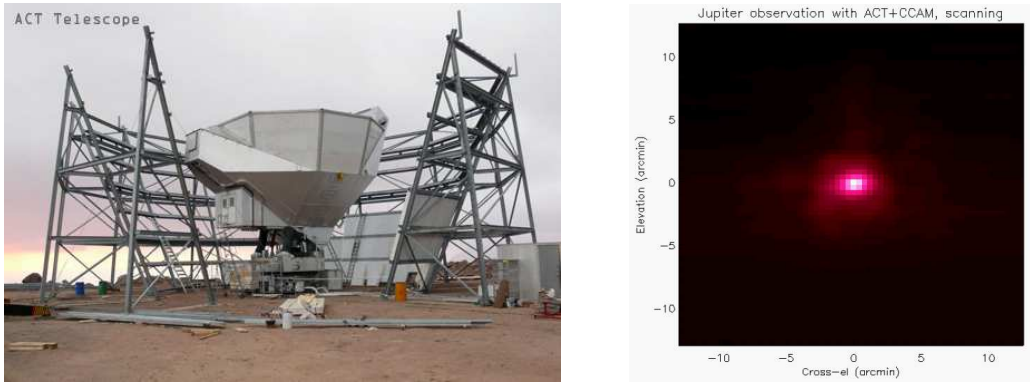

Figure 1.1 Left: ACT telescope in Chile in early 2007. The truss structure in the image is the ground screen, which is completely assembled as of September 2007. Right: ACT first light image of Jupiter observed in June 2007. Pictures from ACT website (http://www.physics.princeton.edu/act/).

carried out by the Atacama Cosmology Telescope (ACT) located in Chile (Kosowsky 2006) and the South Pole Telescope (SPT) (Ruhl et al. 2004). ACT and SPT both saw first light in 2007 (see Figure 1.1) and plan to survey several hundreds to thousands of square degrees over the next three years. One goal of these projects is to detect hundreds to thousands of galaxy clusters by their microwave signal. Optical follow-up of these clusters with, for example, the Southern African Large Telescope (SALT) (for ACT) or the Dark Energy Survey (DES) (for SPT) will yield cluster redshifts. In this way the cluster number density evolution can be precisely measured, provided that potential systematic uncertainties are understood and corrected for.

In Chapter 3, I focus on weak-lensing cluster surveys such as the Deep Lens Survey (DLS), which detects clusters by their weak-lensing shear signal. In particular, I focus on the X-ray follow-up of these shear selected clusters using the *Chandra* and *XMM-Newton* X-ray satellites to compare cluster mass estimates from X-ray and weak-lensing observations.

1.2.1 Galaxy Cluster Number Density Evolution and its Uncertainties

The measured cluster number density today as a function of mass has already put important constraints on our standard cosmological model (e.g., Bahcall et al. 2003). The exciting new application of this technique is to precisely measure the cluster number density as a function of mass and redshift out to redshifts greater than 1. How this density changes with cosmic time depends on the growth rate of structure. Galaxy clusters can be detected in a variety of

different ways at different wavelengths. Millimeter-waveband surveys enable galaxy clusters to be detected via their Sunyaev-Zel'dovich (SZ) distortion. The SZ effect arises when microwave background photons encounter a galaxy cluster between the last scattering surface and us. The hot ionized gas in the galaxy cluster ($T \approx 10^8$ K) inverse Compton scatters the photons and boosts their energy. This results in a decrease in intensity of microwave photons below 217 GHz and an increase in intensity above this frequency. In microwave images spanning several frequencies around 217 GHz, this tell-tale intensity decrement and corresponding increment makes galaxy clusters relatively easy to detect. At a given frequency, the SZ signal of a cluster is roughly proportional to the product of the cluster's gas density and temperature (i.e., its gas pressure). This signal is also independent of the cluster's redshift (unlike X-ray and optical signals), making it ideal for finding clusters out to redshifts where they first began to form.

Optical weak-lensing cluster surveys also utilize a promising technique as they detect clusters by measuring how much a cluster's gravitational potential distorts the apparent shapes of background galaxies. This technique is sensitive to a cluster's total mass as opposed to its trace baryons which are subject to the details of gas and stellar evolution. Finally, optical surveys can also detect clusters by measuring over-densities of galaxies, and X-ray surveys detect thermal bremsstrahlung emission from the hot cluster gas.

Cluster Mass Uncertainties

Upcoming cluster surveys, such as ACT and SPT, together will have the statistical power to constrain the dark energy equation of state to 5% by measuring cluster number density evolution (Carlstrom et al. 2005) (see Figure 1.2, left panel). However, these tight constraints hinge on being able to relate the cluster observable (SZ flux, X-ray flux, galaxies, or weak-lensing shear) to the cluster mass. For an ACT/SPT-like survey, optimistic theoretical predictions suggest that both cosmology and the relation between cluster observable and cluster mass can be jointly constrained by measuring the cluster redshift distribution, the cluster power spectrum (obtained at no extra observational cost), and the masses of roughly a hundred clusters in the sample, each with a 1σ accuracy of 30% (Carlstrom et al. 2005, and references therein). These predictions suggest that surveys of clusters can yield dark sector constraints of similar precision to those from the future microwave background satellite *Planck* and future supernovae Ia observations, including a constraint on the dark energy equation of state to 5-10% (see Figure 1.2, right panel). However, a great deal of further work via simulations and observations needs to be carried out both to verify the potential suggested by these claims and to make them a reality. This need has motivated my thesis research, which makes progress along these lines.

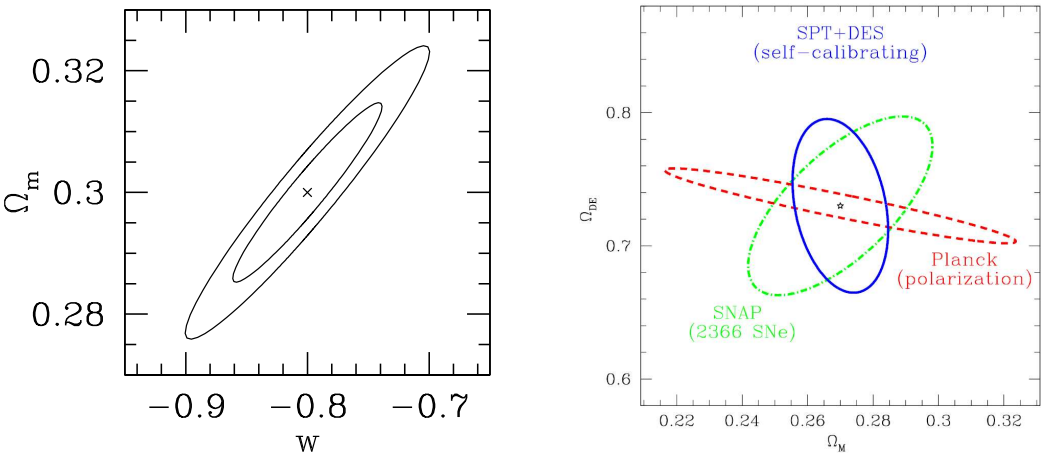

Figure 1.2 Left: Cosmological constraints on the Universe's matter density (Ω_M) and dark-energy equation of state (w) from an SPT/ACT-like millimeter wavelength cluster survey of thousands of square degrees, assuming only statistical uncertainty (Carlstrom et al. 2002). Right: Theoretical forecasts for the same survey as before including some systematic errors, assuming 100 clusters in the sample have well-determined masses, and jointly fitting for cosmology and the SZ flux - mass scaling relation (solid curve) (Carlstrom et al. 2005). Constraints shown are for the dark energy density (Ω_{DE}) and matter density of the Universe today.

Cluster Selection Uncertainties

The cluster selection function describes the cluster sample completeness and contamination. For interesting cosmological constraints one needs to know both the fraction of undetected clusters in a given mass and redshift range and the fraction of false detections to the few percent level (Carlstrom et al. 2005). The cluster sample selection is a function of the contaminating astrophysical signals unique to the detection method of choice. It is also a function of the physics of the intergalactic medium, the sensitivity and resolution of the instrument, and the particular data reduction techniques employed. Much work still needs to be done using both simulations and observations to determine the selection function of any of the above mentioned cluster detection techniques to the required accuracy. Again, this has motivated my thesis research, which makes progress towards understanding the cluster selection function for millimeter-waveband surveys.

1.2.2 Chapter 2: Projections for Galaxy Cluster Detection with ACT

In Chapter 2, I examine the potential of a microwave survey such as ACT to detect galaxy clusters via the SZ effect. This is studied via realistic simulations of the microwave sky, in the development of which I played a major role. These simulations include the primary microwave

background, galactic dust emission, radio and submillimeter galaxies uncorrelated with galaxy clusters, and the SZ signal from galaxy clusters. They are also currently used by the ACT team to develop data analysis techniques and are publicly available[1]. In the work described in this chapter, a Wiener filter is employed to separate the SZ cluster signal from other contaminating millimeter-wavelength signals, and the completeness and purity of the recovered cluster sample is investigated by comparing the recovered sample to the catalog of halos originally input in the simulations. From this analysis, it is shown that ACT can potentially recover a sample that is 90% complete and 85% pure down to $3 \times 10^{14} M_{\odot}$. (This mass is that contained within a radius within which the mean density is 200 times the critical density of the Universe at the cluster redshift.) The relation between SZ flux and cluster mass is also investigated in this chapter via simulations. It is shown that the scaling relation between integrated SZ flux and cluster mass follows a power-law with an index that is steeper than that for self-similar cluster models. Some evolution of the power-law index and normalization with redshift is also suggested (Sehgal et al. 2007).

1.2.3 Chapter 3: Comparison of X-ray and weak-lensing cluster mass estimation techniques

In Chapter 3, I investigate the robustness of and biases inherent in X-ray and weak-lensing cluster mass estimates using the deep optical lensing data from the 20 deg^2 Deep Lens Survey (DLS) (Wittman et al. 2006). To do this I analyze X-ray follow-up observations of shear-selected clusters from the DLS. Since X-ray, SZ, and optical richness measures of cluster mass all depend on the cluster's baryons, which are more sensitive to physical processes such as cluster mergers, shocks, cooling, and feedback, it is instructive to compare these mass estimates to those from weak lensing, which directly probes a cluster's total matter content. This allows one to quantify the possible biases in cluster mass estimates arising from the use of cluster baryons as tracers of mass as opposed to the total matter potential itself. This benefits not only X-ray, SZ, and shallow optical cluster surveys but also informs future large-area weak-lensing cluster surveys, which have other potential sources of mass systematic error to deal with.

In this chapter, I focus on the comparison of X-ray and weak-lensing masses for four galaxy clusters that comprise the top-ranked shear-selected cluster system in the Deep Lens Survey. The weak-lensing observations of this system, which is associated with Abell 781, are from the Kitt Peak Mayall 4-m telescope, and the X-ray observations are from both *Chandra* and

[1] http://www.astro.princeton.edu/∼act/

XMM-Newton. We find that for three of these clusters, there is agreement between X-ray and weak-lensing masses. For the other cluster, the X-ray mass is higher than that from weak lensing by 2σ. X-ray images suggest that this cluster may be undergoing a merger with a smaller cluster (Sehgal et al. 2008), and it is possible that this merger is causing the discrepancy in mass estimates using these two techniques.

1.2.4 Chapter 4: Prospects for Measuring Galaxy Cluster Peculiar Velocities with ACT

In Chapter 4, I explore a new and potentially powerful technique to measure structure growth using galaxy cluster peculiar velocities. An object's peculiar velocity is its velocity with respect to the primary microwave background reference frame. The SZ signal is not only sensitive to the density and temperature of a galaxy cluster but also to its peculiar velocity, as a cluster's peculiar motion Doppler shifts the energy of Compton scattering microwave photons. Usually, measuring the peculiar velocity of any object farther than $z \approx 0.01$ is hampered by needing to know the object's distance away from us, independent of the Hubble constant, to an accuracy of order 10%. This distance measurement allows for the accurate removal of the Hubble expansion from a measured redshift to arrive at the component due to the peculiar motion (i.e., Doppler shift) of the object. Extracting clusters' peculiar velocities from their SZ signal would allow us to map out the velocity field to much higher redshifts ($z>1$) without requiring independent distance information. This could provide better constraints on structure growth and cosmology than from cluster number density evolution because the velocity field is sensitive to the derivative of the growth of structure and is not hampered by relying on cluster masses, for which the systematic errors can be large as discussed above. It has been shown that if galaxy cluster peculiar velocities can be measured to an accuracy of 100 km/sec for all clusters above $10^{14} M_{\odot}$ in a large-area millimeter survey (≈ 1000 deg^2), then the normalization of the matter power spectrum and the dark energy equation of state can be measured to better than 10% (Bhattacharya & Kosowsky 2007).

However, the peculiar velocity contribution to the SZ signal is an order of magnitude smaller than the primary contribution, which is proportional to the cluster density times its electron temperature. Moreover, the entire SZ signal is buried under contaminating signals (primary microwave background, radio and submillimeter galaxies etc.). In Chapter 4, I show that three-frequency millimeter observations at 145, 215, and 280 GHz, with an ACT-like instrument, do not provide sufficient information to disentangle a cluster's peculiar velocity from its full SZ

signal given an ideal measurement of this signal with no contaminants. However, the addition of a temperature estimate from another source with 1σ error bars less than 2 keV or the addition of lower frequency millimeter observations, does allow the cluster peculiar velocity to be measured with a statistical error of ≈ 100 km/sec (Sehgal et al. 2005).

Bibliography

Albrecht, A., et al. 2006, ArXive-prints (astro-ph/0609591)

Bahcall, N. A., et al. 2003, ApJ, 585, 182

Bhattacharya, S., & Kosowsky, A. 2007, ApJ, 659, L83

Carlstrom, J. E., et al. 2005, http://spt.uchicago.edu/spt/depot/pdf/force.pdf

Carlstrom, J. E., Holder, G. P., & Reese, E. D. 2002, ARA&A, 40, 643

Kosowsky, A. 2006, New Astronomy Review, 50, 969

Ruhl, J., et al. 2004, in Millimeter and Submillimeter Detectors for Astronomy II. Edited by Jonas Zmuidzinas, Wayne S. Holland and Stafford Withington Proceedings of the SPIE, Volume 5498, pp. 11-29 (2004)., ed. C. M. Bradford, P. A. R. Ade, J. E. Aguirre, J. J. Bock, M. Dragovan, L. Duband, L. Earle, J. Glenn, H. Matsuhara, B. J. Naylor, H. T. Nguyen, M. Yun, & J. Zmuidzinas, 11

Sehgal, N., Hughes, J. P., Wittman, D., Margoniner, V., Tyson, J. A., Gee, P., & dell'Antonio, I. 2008, ApJ, 673, 163

Sehgal, N., Kosowsky, A., & Holder, G. 2005, ApJ, 635, 22

Sehgal, N., Trac, H., Huffenberger, K., & Bode, P. 2007, ApJ, 664, 149

Wittman, D., Dell'Antonio, I. P., Hughes, J. P., Margoniner, V. E., Tyson, J. A., Cohen, J. G., & Norman, D. 2006, ApJ, 643, 128

Wang, S., Hui, L., May, M., & Haiman, Z., 2007, Phys. Rev. D, 76, 063503

Chapter 2

Microwave Sky Simulations and Projections for Galaxy Cluster Detection with the Atacama Cosmology Telescope

The material in this chapter also appears in print as "Microwave Sky Simulations and Projections for Galaxy Cluster Detection with the Atacama Cosmology Telescope", Sehgal et al. 2007, ApJ, 664, 149.

2.1 Introduction

Cluster catalogs provide valuable information on the evolution and distribution of matter over cosmic time. It has long been realized that the abundance of galaxy clusters as a function of redshift is a sensitive probe of the underlying cosmology (e.g. Oukbir & Blanchard 1992; Eke et al. 1996; Viana & Liddle 1996; Barbosa et al. 1996; Bahcall & Fan 1998; Rosati et al. 2002). It has also been appreciated that a large sample of galaxy clusters can provide important constraints on the dark energy density and equation of state which are complementary to those obtained from microwave background and type Ia supernovae measurements (e.g. Wang & Steinhardt 1998; Haiman et al. 2001; Weller et al. 2002; Weller & Battye 2003; Majumdar & Mohr 2003; Wang et al. 2004; Lima & Hu 2005). This has prompted efforts to obtain cluster catalogs from wide, deep surveys.

Searches for clusters based on their Sunyaev-Zel'dovich (SZ) effect (Sunyaev & Zeldovich 1970, 1972) have a particular advantage over X-ray and optical searches since the SZ signal does not dim at high redshifts (z>1), where the cluster abundance is strongly dependent on cosmology. (For reviews on the SZ effect see Birkinshaw (1999) and Carlstrom et al. (2002)). In light of this, there are a host of ground-based bolometer array instruments (ACBAR, ACT, APEX, SPT) and interferometers (AMI, AMiBA, SZA) either online or scheduled to come online in the next few years that potentially will detect hundreds to thousands of clusters at microwave frequencies via their SZ effect (Runyan et al. 2003; Kosowsky 2003; Güsten et al. 2006; Ruhl et al. 2004; Kneissl et al. 2001; Li et al. 2006). The *Planck* satellite, to be launched in 2008, should also provide an all-sky map of massive clusters in the microwave band (Tauber

2004).

Using cluster catalogs to constrain cosmology requires a solid understanding of the cluster selection criteria. A given survey's cluster selection function is intimately tied to characteristics of the instrument and data reduction techniques. Considerable attention has been devoted to exploring various data reduction methods for different SZ surveys. This has been pursued in an effort to study both the optimal detection of clusters and the optimal recovery of the cluster SZ flux. The former consists of maximizing the completeness and minimizing the contamination of a given cluster sample. The latter is necessary to properly identify the observable (SZ flux) with mass, or to employ self-calibration schemes to fit for the SZ flux - mass relation and cosmology simultaneously (Majumdar & Mohr 2004; Younger et al. 2006).

Various filtering approaches have been utilized to isolate the SZ signal and extract clusters in simulations. Such techniques have employed matched filters (Herranz et al. 2002a,b), Wiener filters (Aghanim et al. 1997), wavelet filters (Pierpaoli et al. 2005), and maximum entropy methods (Stolyarov et al. 2002). Several papers have implemented versions of these filters and begun careful study of selection functions for upcoming SZ surveys (Schulz & White 2003; White 2003; Melin et al. 2005; Vale & White 2006; Melin et al. 2006; Schaefer & Bartelmann 2006; Juin et al. 2007). With this in mind, we have created a large-scale simulation of the microwave sky on which these data reduction techniques can be refined.

To model the SZ flux accurately generally requires expensive, high-resolution hydrodynamic simulations to realistically model the small scale cluster physics. However, it is a challenge to create such simulations in a large enough volume so that one is not limited by cosmic variance when performing statistical studies. To overcome this challenge, we create a cluster catalog using an N-body simulation combined with a gas prescription given by Ostriker et al. (2005). The N-body code only needs to be run once for a given cosmology, and the small scale cluster physics (including non-spherically symmetric gas distributions, star formation, and feedback) are added afterward via the gas prescription. As a result, the cluster physics can be varied easily without having to redo expensive runs.

These cluster simulations were incorporated within microwave-sky simulations consisting of two strips of the sky, each 4 degrees wide in declination and 360 degrees around in right ascension. One strip is centered at a declination of -5 degrees, and the other is centered at a declination of -55 degrees, to match the portion of sky that the Atacama Cosmology Telescope (ACT) will observe. The galaxy clusters within this simulation have halo masses down to 5×10^{13} $M_{\odot}$, and the N-body simulation employs the latest cosmological parameters derived from a combination of WMAP3, SDSS, HST, and SN Astier observations (Ω_m=0.26, Ω_Λ=0.74, Ω_b=0.044, n=0.95,

σ_8=0.77, h=0.72) (see Spergel et al. 2006, and references therein). We include the full SZ effect, with relativistic corrections, as well as infrared and radio point sources (uncorrelated with clusters), using number counts given by Borys et al. (2003) (infrared) and Knox et al. (2004) (radio). Galactic dust and primary microwave background fluctuations are also modeled, the later generated using the WMAP ILC map (Bennett et al. 2003a; Hinshaw et al. 2006). These sky simulations were made at the observing frequencies of 145, 215, and 280 GHz and are in a cylindrical equal area sky projection (Calabretta & Greisen 2002). The final sky maps are in a standard FITS format and have a pixel size of $\approx 0.2' \times 0.2'$ and units of Jy/ster. A catalog of all the cluster halos in the simulation is also provided, specifying each halo's basic properties. These microwave-sky simulations are available at http://www.astro.princeton.edu/∼act/.

We use these simulations to study the scaling relation between SZ flux and cluster mass, as well as prospects for cluster detection with ACT. Roughly 10^5 clusters are used to determine the simulated SZ flux - mass scaling relation. We compare cluster M_{200} to Y_{200}, which we take to be the SZ Compton-y parameter integrated over a disk of radius R_{200}. These clusters are fit to a power-law relation between $Y_{200} \times E(z)^{-2/3}$ and M_{200}, and estimates of the power-law index and normalization are given.

We also employ a multi-frequency Wiener filter and simple peak-finding algorithm to forecast cluster detection given ACT instrument specifications. Since there has been considerable interest of late in how point source contamination affects cluster detection (e.g. Melin et al. (2006)), this is investigated under three different contamination assumptions: no point sources, only infrared point sources, and both infrared and radio point sources. Completeness of our recovered cluster sample is given as both a function of M_{200} and Y_{200} (in units of arcmin^2), the latter being directly obtainable from microwave observations. We also give the purity of our projected cluster sample, where purity is one minus the percentage of false-positive detections. The issue of optimal SZ flux recovery for individual clusters is left to later work.

The outline of this paper is as follows. In §2.2, we give the simulation details. §2.3 consists of an investigation of the Y-M relation as suggested by our simulations, and §2.4 gives cluster detection projections for ACT. In §2.5, we discuss directions for future work, and, in §2.6, we summarize and conclude.

2.2 Simulations

2.2.1 Simulated Clusters

The Dark Matter Run

Initial conditions for the N-body run were generated with the GRAFIC2 code (Bertschinger 2001), available at http://web.mit.edu/edbert/. As written, this code uses a spherical Hanning filter on small scales. However, we have found that this filter significantly suppresses power on these scales, so we removed it from use. GRAFIC2 perturbs particles from a regular grid using the Zel'dovich approximation. The simulation started at redshift z=35.3, when the initial density fluctuation amplitude on the scale of this grid was 10%. $N = 1024^3 \approx 10^9$ particles were contained in a periodic box of size $L = 1000h^{-1}$Mpc, so the particle mass is thus $6.72\times10^{10}h^{-1}M_\odot$. The cubic spline softening length was set to $\epsilon = 16.276h^{-1}$kpc. The simulation was carried out with the TPM code (Bode et al. 2000; Bode & Ostriker 2003), modified slightly from the publicly available version (at http://www.astro.princeton.edu/∼bode/TPM/). Particle positions and velocities were followed at double precision, though acceleration was kept at single precision. Also, no lower limit was set to the parameter B used in domain decomposition (see eq. 5 of Bode & Ostriker 2003), which at late times results in more particles being followed at full force resolution. The initial domain decomposition parameters used are $A = 1.9$ and $B = 9.2$. The PM mesh contained 2048^3 cells, and the maximum sub-box was 256 cells. By the end of the run, 5×10^6 trees containing 54% of the particles were followed at full resolution. More details of the simulation are in Bode et al. (2007).

At each PM time step, the matter distribution in a thin shell is saved. The radius of the shell corresponds to the light travel time from a $z = 0$ observer sitting at the origin of the box, and its width corresponds to the time step interval. The portion of a spherical shell covering one octant of the sky was saved, so for comoving distances larger than $1000h^{-1}$Mpc there can be some duplication in structures as the periodic box is repeated. However, while there are repeated dark matter halos in the simulations, the repetition is usually at a different redshift, so the dynamical state is different. In cases where a cluster appears twice at the same redshift, it is viewed at two different angles, making each projected image unique. At the end of the simulation, the full matter distribution in a light cone extending to $z = 3$ was saved in 417 time slices. Dark matter halos in this light cone were identified with the Friends-of-Friends (FoF) algorithm using a linking parameter $b = 0.2$ (i.e. the linking length is one fifth of the mean interparticle separation of the simulation, or $195h^{-1}$kpc comoving). A $5 \times 10^{13}h^{-1}M_\odot$ cluster

contains 744 particles.

As shown in Figure 2.1, the halo mass functions measured from the simulated light cone agree well with the semi-analytic fitting formula from Jenkins et al. (2001) for a FoF linking length $b = 0.2$. The number of halos above a minimum mass per unit redshift per 100 square degrees is plotted for three minimum masses $M_{\rm min} = (1, 2, 4) \times 10^{14} M_\odot/h$. The data points are measured using all halos in the octant to minimize sample variance, but then are normalized to 100 square degrees. For any cluster survey, the minimum detectable mass is likely to be a function of redshift, and the three values chosen reflect the range expected for the upcoming SZ surveys.

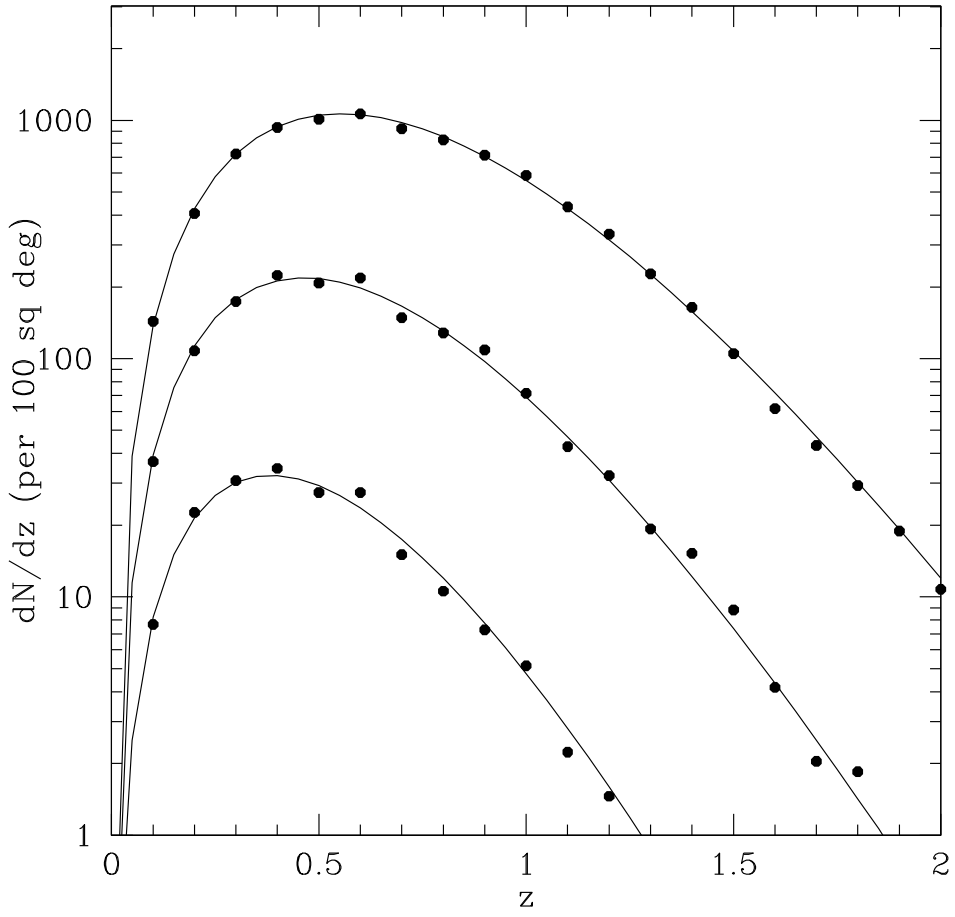

Figure 2.1 The halo abundance above a minimum mass per unit redshift per 100 square degrees measured from the simulation is compared with the semi-analytic fitting formula from Jenkins et al. (2001). From top to bottom, the three sets of points are for the minimum masses $M_{\rm min} = (1, 2, 4) \times 10^{14} M_\odot/h$.

Adding Gas to Dark Matter Halos

Gas is added to each cluster following the prescription of Ostriker et al. (2005) and Bode et al. (2007). For each dark matter halo, the gravitational potential is found on a mesh with cell size $2\epsilon = 32.552h^{-1}$kpc. The gas density and pressure (or temperature) are found in each cell by assuming it is in hydrostatic equilibrium and has a polytropic equation of state with adiabatic index $\Gamma = 1.2$. It is also assumed that initially the baryon fraction inside the virial radius is Ω_b/Ω_m, and that the energy per unit mass of the baryons equals that of the dark matter. To specify the central density and pressure with these assumptions requires two constraints.

The first constraint is the pressure at the virial radius, which is the radius enclosing the virial overdensity calculated from spherical tophat collapse (this is a slight change from Ostriker et al. 2005, which used an overdensity of 200 times critical). The dark matter kinetic energy is found in a buffer region extending for nine cells outside of the virial radius. This is then translated into a surface pressure, P_s, by assuming the velocity dispersion is isotropic and the baryon fraction in this region equals the cosmic mean. The second constraint is conservation of energy. The final energy of the gas must equal this initial energy, after adjusting for any of the effects that can cause changes in energy.

One such effect is that the gas distribution inside the cluster can expand or contract. This can, for example, reduce the baryon fraction inside the virial radius if the gas distribution expands further out. This would also reduce the energy of the gas as it does mechanical work pushing against the surface pressure. The surface pressure is assumed to remain at P_s wherever the final gas radius ends up.

Star formation will also affect gas energy. At $z = 0$, it is assumed that the stellar to gas mass ratio is 0.10. The star formation rate is assumed to follow a delayed exponential model (eq. 1 of Nagamine et al. 2006) with decay time $\tau = 1$ Gyr, so at higher redshift the star/gas mass ratio can be calculated. To make stars, the gas with the largest initial binding energy is removed, thus changing the total energy budget. Furthermore, some fraction of the rest mass turned into stars is taken to be converted into thermal energy in the gas, via supernovae and AGN. The energy added to the intracluster medium by these processes can be written as $\epsilon_f M_* c^2$, where M_* is the stellar mass and the feedback efficiency is estimated to be $\epsilon_f = 5 \times 10^{-5}$. This value is determined by fitting to X-ray observations of nearby clusters (Bode et al. 2007); at z=0, this added energy amounts to roughly 3 keV per particle.

The upper panel of Figure 2.2 shows the resulting $M_{500} - T$ relation for all the clusters in the light cone at low redshift, $z < 0.2$. The temperature used is the X-ray emission-weighted

temperature inside R_{500}. The $kT > 5$keV clusters are shown as open circles, and, for clarity, the median value of the clusters below 5 keV is shown as a line, with the shaded region enclosing 90% of the clusters. Shown for comparison is data derived from X-ray clusters over the same redshift range, taken from Reiprich & Böhringer (2002) as adjusted by McCarthy et al. (2004). The simulated sample reproduces the observed $M_{500} - T$ relation quite well. The gas temperature (or pressure) is fairly insensitive to the exact choice of ϵ_f. Feedback has much more of an effect on gas density, making the $L_X - T$ relation a more exacting comparison (Bode et al. 2007). This relation is shown in the bottom panel of Figure 2.2, along with data points taken from the ASCA cluster catalog (Horner 2001) as described in McCarthy et al. (2004). Again, the simulated clusters agree with the observed relation.

2.2.2 Simulated SZ Signal

For each of the simulated clusters, the gas prescription gives us the electron number density n_e, temperature T_e, and velocity v fields with which to model the SZ effect, including relativistic corrections. We assume that the gas is fully ionized with a helium mass fraction equal to 0.24. The change in the microwave background intensity after passing through a path length dl in the direction $\hat{n}$ is given by

$$\begin{aligned}\frac{\Delta I_\nu}{I_0} = &\frac{X^4 e^X}{(e^X-1)^2}\mathrm{d}\tau\theta_e\left[Y_0 + \theta_e Y_1 + \theta_e^2 Y_2 + \theta_e^3 Y_3 + \theta_e^4 Y_4\right] \\ &+ \frac{X^4 e^X}{(e^X-1)^2}\mathrm{d}\tau(\frac{v}{c})^2\left[\frac{1}{3}Y_0 + \theta_e(\frac{5}{6}Y_0 + \frac{2}{3}Y_1)\right] \\ &+ \frac{X^4 e^X}{(e^X-1)^2}\mathrm{d}\tau\frac{v_{\mathrm{los}}}{c}\left[1 + \theta_e C_1 + \theta_e^2 C_2\right], \end{aligned} \tag{2.1}$$

where

$$I_0 \equiv 2(k_B T_{CMB})^3/(hc)^2, \tag{2.2}$$

$$X \equiv h\nu/k_B T_{CMB}, \tag{2.3}$$

$$\theta_e \equiv k_B T_e/m_e c^2, \tag{2.4}$$

and the Y's and C's are known frequency-dependent coefficients (Nozawa et al. 1998). The usual Compton y-parameter is given by

$$y \equiv \int \theta_e \mathrm{d}\tau = \frac{k_B \sigma_T}{m_e c^2}\int n_e T_e \mathrm{d}l, \tag{2.5}$$

where $\mathrm{d}\tau = \sigma_T n_e \mathrm{d}l$ is the optical depth through a path length dl. The first-order (non-relativistic) thermal and kinetic SZ signals are given by

$$\left(\frac{\Delta T}{T_{\mathrm{CMB}}}\right)_{\mathrm{tsz}} \equiv y Y_0 = y\left(X\coth(X/2) - 4\right) \tag{2.6}$$

and

$$\left(\frac{\Delta T}{T_{CMB}}\right)_{\rm ksz} \equiv \int \left(\frac{v_{\rm los}}{c}\right) {\rm d}\tau = \sigma_T \int n_e \left(\frac{v_{\rm los}}{c}\right) {\rm d}l, \tag{2.7}$$

respectively, where $v_{\rm los}$ is the line-of-sight component of the peculiar velocity field. For a 10 keV cluster with $v_{\rm los} = 1000$ km/sec, the correction to the first-order thermal SZ from the $O({\rm d}\tau\theta_e^2)$ term at 145 GHz is about 7.5%, but it becomes considerably more substantial near the null of the thermal SZ. The terms $O({\rm d}\tau v_{\rm los}\theta_e)$ and $O({\rm d}\tau v_{\rm los}\theta_e^2)$ give about 8% and 1% corrections to the first-order kinetic SZ (Nozawa et al. 1998). Note that the factor $X^4 e^X/(e^X-1)^2$ in equation 2.1 converts between $\Delta T/T_{CMB}$ and $\Delta I_\nu/I_0$.

Sky maps at the ACT observing frequencies of 145, 215, and 280 GHz are made by tracing through the clusters and projecting them onto a cylindrical equal-area grid. Two strips of the sky, each 4 degrees wide in declination and 360 degrees around in right ascension, are constructed and centered at $\delta = -5$ and $\delta = -55$ degrees, respectively. Since the simulation light cone covers an octant, only a quarter of the strip is unique and the other three-quarters are mirrored. The accompanying cluster catalog contains the following information: redshift, right ascension, declination, $M_{\rm FoF}$, M_{200}, M_{500}, R_{200}, R_{500}, and integrated SZ and X-ray properties. ($M_{\rm FoF}$ is the FoF derived mass and M_{200} and M_{500} are the cluster masses within R_{200} and R_{500} respectively, where the latter are the radii at which the cluster mean density is 200 and 500 times the critical density at the cluster redshift.) Figure 2.3 is a sample image showing the fully relativistic SZ signal at 145 GHz. This image is 33 degrees across in right ascension and 4 degrees wide in declination, centered at $\delta = -55$ degrees. Black represents $\Delta T/T_{CMB}$ greater than -6×10^{-6}, and white represents $\Delta T/T_{CMB}$ less than -10×10^{-6}. The former value is chosen to be representative of ACT instrument noise in 0.2' pixels.

In Figure 2.4, the first-order thermal SZ power spectrum from the simulated map at 145 GHz is compared with a semi-analytic prediction derived following the prescription of Komatsu & Seljak (2002). On large angular scales, $l \sim 100$, the two spectra are in agreement, but deviations on smaller scales are found. This is to be expected, since our gas prescription accounts for star formation and feedback which reduce the gas density within clusters (Ostriker et al. 2005; Bode et al. 2007), resulting in a suppression of power on small ($l \gtrsim 1000$) scales. In addition, the feedback pushes the gas out to larger radii and increases the overall temperature of the cluster, leading to an enhancement of power on scales $l \lesssim 1000$. This demonstrates that one must have a good understanding of baryonic physics within clusters in order to extract cosmology from the SZ power spectrum. Conversely, if the cosmology is well determined, then one can learn about cluster physics from the detected SZ signal.

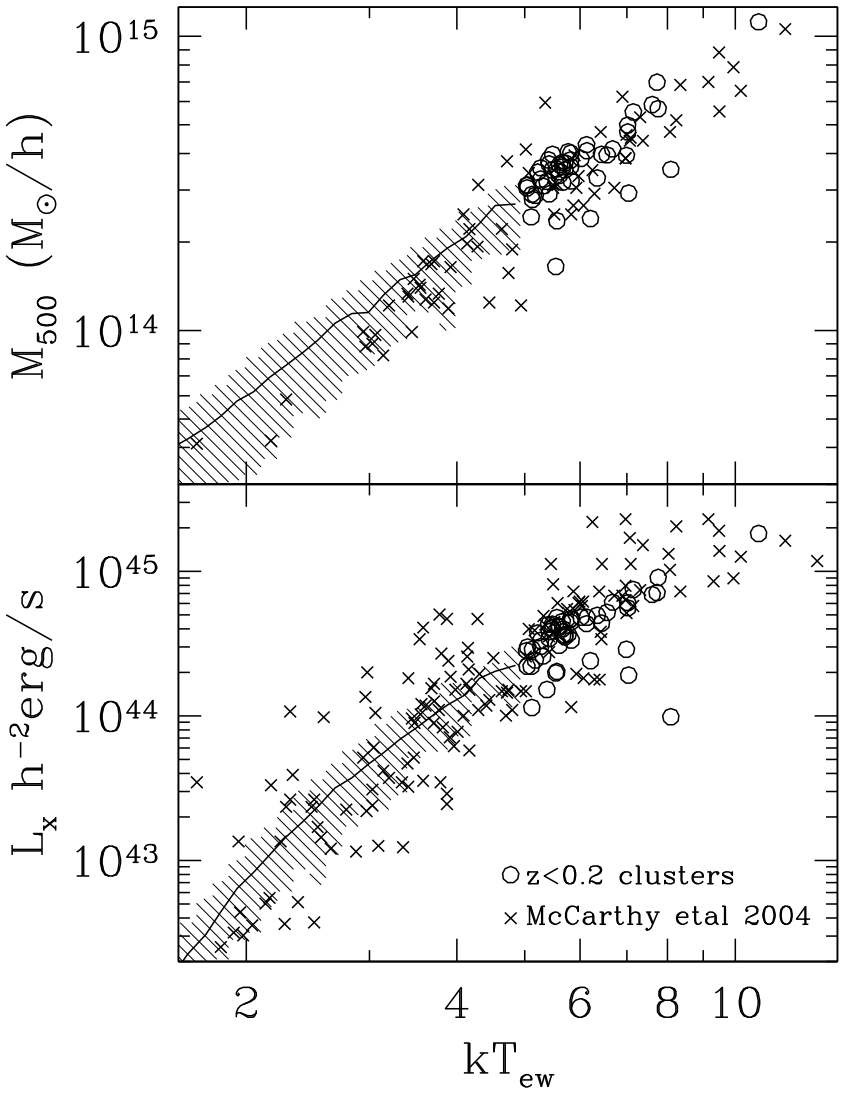

Figure 2.2 The panels show the $M_{500} - T$ and $L_X - T$ relations for the simulated clusters below $z = 0.2$ compared to those from observed X-ray clusters. The open circles are the simulated clusters above $kT_{\rm ew} = 5$keV. The median value of the simulated clusters below 5 keV is represented by a solid line, with the shaded region enclosing 90% of the clusters. $T_{\rm ew}$ is the emission-weighted X-ray temperature.

Figure 2.3 A sample image showing the fully relativistic SZ signal at 145 GHz. The image dimensions are 33 degrees across in right ascension by 4 degrees wide in declination centered at $\delta = -55$ degrees. Black represents $\Delta T/T_{CMB}$ greater than -6×10^{-6}, and white represents $\Delta T/T_{CMB}$ less than -10×10^{-6}. The former value is chosen to be representative of ACT instrument noise in 0.2' pixels.

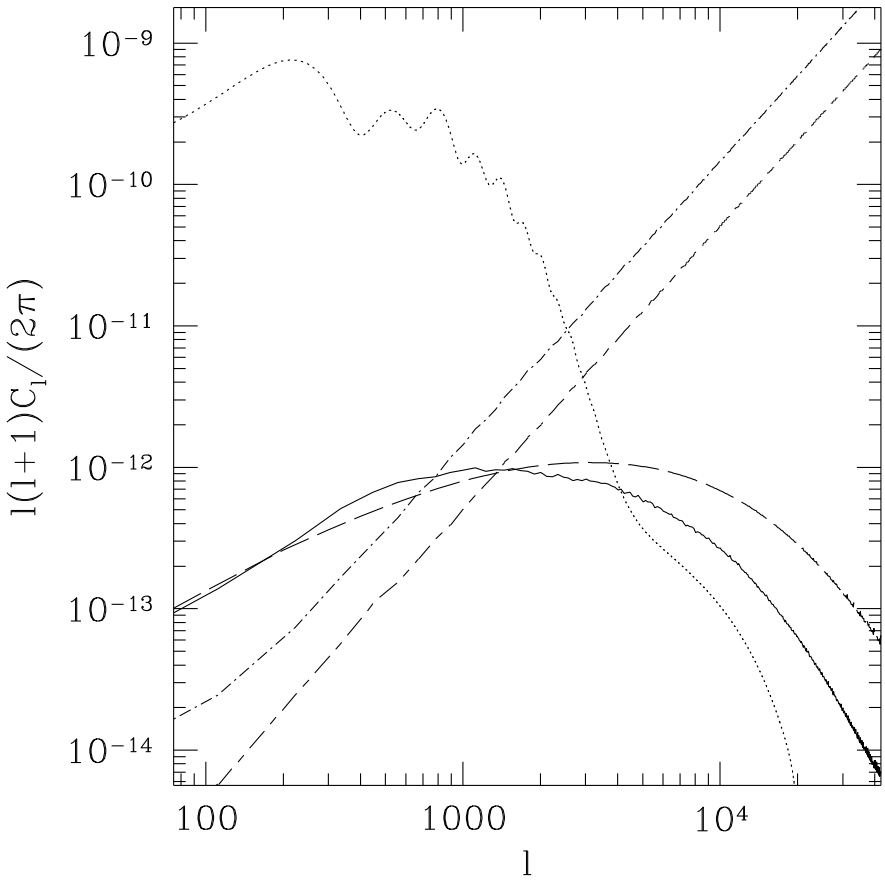

Figure 2.4 Solid curve is the first-order thermal SZ power spectrum at 145 GHz from the simulation. Dashed curve is the first-order thermal SZ power spectrum at 145 GHz derived analytically from Komatsu & Seljak (2002). For comparison, we include the lensed primary microwave background power spectrum derived from CAMB (Challinor & Lewis 2005) for our input cosmology (dotted) and the power spectrum of infrared (dot-dashed) and radio (dash-dashed) point sources from the simulation, also at 145 GHz. The radio source power spectrum includes only sources fainter than 35 mJy. Note that C_l is in dimensionless units of $(\Delta T/T)^2$.

2.2.3 Simulated Primary CMB, Point Sources, and Galactic Dust

A primary microwave background map is constructed to have the same large scale structure as we observe on the sky and small scale structure consistent with theoretical expectations. For our large scale map, we use the WMAP ILC map (Bennett et al. 2003a; Hinshaw et al. 2006). For $l < 20$, the a_{lm}'s are taken from the ILC map with no modification. At smaller scales, the ILC map is smoothed, so a Gaussian random field is added such that the ensemble average power equals the theoretical power spectrum taken from the WMAP LAMBDA website (http://lambda.gsfc.nasa.gov/product/map/dr2/ params/lcdm_all.cfm). We generate a map with HEALPix parameter $N_{\rm side} = 4096$ (totaling 201,326,592 pixels). This is then interpolated onto the cylindrical coordinate system using the bilinear interpolation subroutine included in the HEALPix distribution (Górski et al. 2005).

The point sources are drawn from prescribed number counts. For a given flux bin of width ΔS, the number of sources in the survey is drawn from a Poisson distribution with mean $|dN(> S)/dS|\Delta S\Delta\Omega$. Within the bin, each source is assigned a random flux. We choose logarithmic bins that are narrow compared to the range of source fluxes. Each set of sources has flux counts tallied at some reference frequency ν_0. We scale the source flux from this frequency using a power law, $S \propto (\nu/\nu_0)^\alpha$. Here α is a random variable, chosen for each source from a Gaussian distribution with mean $\bar{\alpha}$ and variance σ_α^2 unique to each source population. For radio sources we use Knox et al. (2004) number counts and choose $\bar{\alpha} = -0.3$ and $\sigma_\alpha = 0.3$ for scaling parameters. WMAP found a flatter spectrum with similar variance, but counts are expected to steepen above 100 GHz. For infrared sources we use Borys et al. (2003) number counts and choose $\bar{\alpha} = 3$ and $\sigma_\alpha = 0.5$.

For the contribution of galactic thermal dust emission, we use the "model 8" prediction from Finkbeiner et al. (1999), an extrapolation to microwave frequencies of the dust maps of Schlegel et al. (1998). This model is a two-component fit to IRAS, DIRBE, and FIRAS data, and is shown by Bennett et al. (2003b) to be a reasonable template for dust emission in the WMAP maps. We create these galactic dust emission maps for completeness of the simulations. However, we do not currently include these dust maps when we investigate cluster detection.

2.3 Y-M Scaling Relation

We would like to better understand the relation between SZ flux and mass because this relation reflects cluster physics and also provides the link between SZ cluster catalogs and cosmological parameters, which are constrained by the cluster distribution as a function of mass. A more

informed understanding about how changes in cluster physics and cosmology alter the $Y - M$ relation will allow for more information about cosmological parameters to be derived from cluster surveys.

To investigate the SZ flux - mass cluster scaling relation, the integrated Compton-y parameter is compared to cluster mass for the clusters in our simulation. The integrated Compton-y parameter is the Compton-y parameter integrated over the face of the cluster, i.e. $Y = (\int y d\Omega) d_A^2(z)$, where $d_A^2(z)$ is the angular diameter distance. In the self-similar model, a virialized halo of mass $M_{\rm vir}$ has a virial temperature equal to

$$T_{\rm vir} \propto [M_{\rm vir} E(z)]^{2/3}, \tag{2.8}$$

where for a flat ΛCDM cosmology

$$E(z) = [\Omega_m (1+z)^3 + \Omega_\Lambda]^{1/2}. \tag{2.9}$$

If clusters were isothermal, we would expect them to satisfy the relation

$$Y \propto f_{\rm gas} M_{\rm halo} T, \tag{2.10}$$

where $f_{\rm gas}$ is the cluster gas mass fraction. Thus we find

$$Y \propto f_{\rm gas} M_{\rm vir}^{5/3} E(z)^{2/3}, \tag{2.11}$$

for the self-similar SZ flux - mass scaling relation. Since clusters are not isothermal and not always in virial equilibrium, deviations from the self-similar relation are expected. Moreover, variation of $f_{\rm gas}$ with redshift and cluster processes such as star formation and feedback can also cause deviations from self-similarity.

From the cluster catalog described in §2.2, we choose a sub-sample with $M_{200} > 7.5 \times 10^{13} M_\odot$ to stay well above our catalog mass limit of $5 \times 10^{13} M_\odot$ and ensure catalog completeness. This leaves us with a sample of about 10^5 clusters. For each cluster, we calculate Y_{200}, which is the projected SZ Compton-y parameter in a disk of radius R_{200}. Clusters are then ranked by mass, and for bins of 250 clusters each, the mean of M_{200} as well as the mean and standard deviation on the mean of $Y_{200} \times E(z)^{-2/3}$ are calculated in each bin. These values are plotted in Figure 2.5. We then fit these values to the power-law relation

$$\frac{Y_{200}}{E(z)^{2/3}} = 10^\beta \Big(\frac{M_{200}}{10^{14} M_\odot} \Big)^\alpha. \tag{2.12}$$

We find $\alpha = 1.876 \pm 0.005$ and $\beta = -5.4774 \pm 0.0009$ with a reduced χ^2 of 1.004. This suggests that the $Y - M$ relation is close to a power-law. This slope is steeper than that for the self-similar model given in equation 2.11. This steepening is expected since we assume feedback is

independent of total cluster mass. Energy input of roughly 3 keV per particle will clearly have a relatively larger effect on small clusters with lower virial velocities than on more massive ones. The feedback reduces the gas mass fraction more in lower mass clusters, as more gas is pushed out in proportion to the cluster's total mass (i.e., the gas fraction inside R_{200} is smaller). As a result, Y_{200} is also decreased more in the lower mass clusters. The power-law index that we find is slightly steeper than that found by some hydrodynamic simulations (e.g. Nagai (2006); Motl et al. (2005); White et al. (2002)). This is understandable since we include feedback from active galactic nuclei as well as supernovae, which is different from the hydrodynamic simulations, and the increased level of feedback steepens the slope. It has been estimated that the feedback from active galactic nuclei may be roughly an order of magnitude larger than that from supernovae (Ostriker et al. 2005), so it potentially has a significant effect. The slope we find is also in between that found by da Silva et al. (2004) for their hydrodynamic simulations including radiative cooling alone and cooling plus preheating.

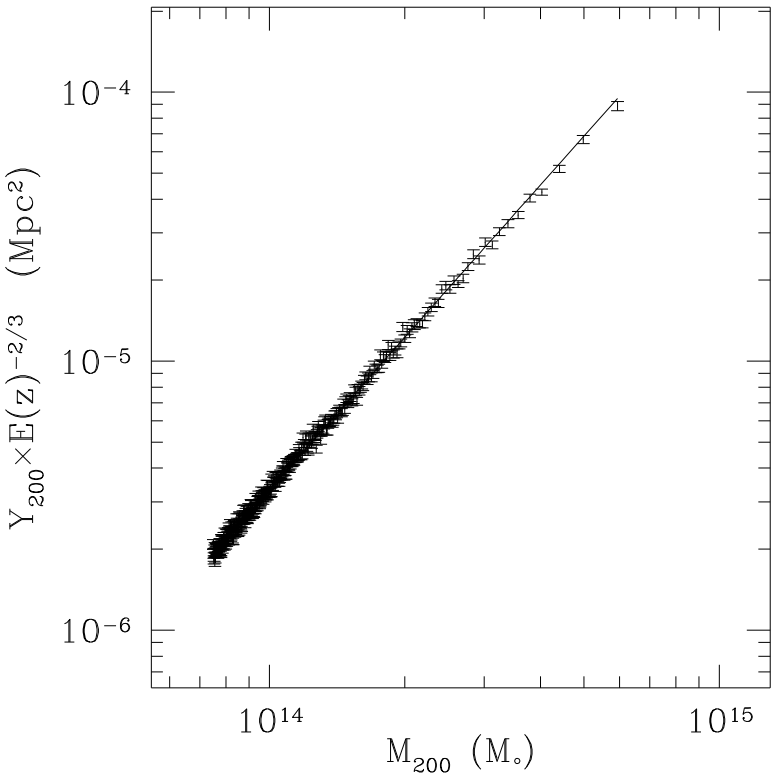

Figure 2.5 $Y_{200} \times E(z)^{-2/3}$ vs. M_{200} for $\approx 10^5$ clusters within the N-body plus gas simulation. Each point represents the mean value for 250 clusters, and error bars represent the error on the mean. The parameters and reduced χ^2 for the best-fit line are given in Table 2.2.

A departure from a power-law is observed when we restrict our cluster sample to have

$M_{200} > 2 \times 10^{14}$ $M_\odot$	α	σ_α	β	σ_β	reduced χ^2	clusters	bins
$z > 0$	1.81	0.02	-5.463	0.009	1.14	7960	398
$z < 0.3$	1.85	0.05	-5.48	0.02	1.05	940	47
$z = 0.3 - 0.6$	1.78	0.03	-5.44	0.01	1.11	3080	154
$z = 0.6 - 0.9$	1.85	0.04	-5.49	0.02	1.48	2420	121
$z = 0.9 - 1.5$	1.82	0.05	-5.46	0.02	0.78	1400	70

Table 2.1 Best-fit parameters for clusters with $M_{200} > 2 \times 10^{14}$ $M_\odot$, fit using the power-law given in equation 2.12.

higher minimum masses. As the minimum mass of the sample is increased, the power-law index gets flatter, illustrating the important effect of feedback on low-mass clusters as well as the fact that the lowest mass clusters dominate the slope of the $Y - M$ relation because their numbers increase rapidly as mass is decreased. The comparison of Table 2.1 and Table 2.2 illustrates this departure, where we have performed a similar analysis as above for clusters with $M_{200} > 2 \times 10^{14} M_\odot$, this time using bins of 20 clusters each. We find $\alpha = 1.81 \pm 0.02$ and $\beta = -5.463 \pm 0.009$ with a reduced χ^2 of 1.14. This departure indicates that while the $Y - M$ relation is close to a power-law, there is some curvature.

We also divide our clusters above $M_{200} > 0.75 \times 10^{14} M_\odot$ into four different redshift bins ($z < 0.3, z \in (0.3, 0.6), z \in (0.6, 0.9)$, and $z \in (0.9, 1.5)$) to see the evolution of the power-law index and normalization with redshift. The best-fit lines to $Y_{200} \times E(z)^{-2/3}$ versus M_{200} are shown in Figure 2.6, and the best fit α and β are given in Table 2.2. Some slight evolution of the power-law index and normalization with redshift is apparent. This is expected since clusters are not perfectly self-similar. Furthermore, the stellar to gas mass ratio is a function of redshift in our simulations, and thus the feedback, which is proportional to the star formation, is also a function of redshift. Since more feedback lowers Y disproportionately at the low-mass end, we find the steepest slope for the clusters with $z < 0.3$, which have undergone more star formation and feedback. We find the flattest slope for the clusters in the highest redshift bin. Examining only the higher mass clusters, $M_{200} > 2 \times 10^{14} M_\odot$, we see little obvious evolution with redshift of the slope and normalization considering their respective error bars (cf. Table 2.1). This again suggests that the higher mass clusters are less sensitive to feedback processes.

The scatter that we find for this $Y - M$ relation is most likely underestimated, as we assume that the gas is described by hydrostatic equilibrium, a single constant polytropic index, and the same amount of feedback per stellar mass for all clusters. Also, we have not included other sources of non-thermal pressure support which may contribute non-negligibly to the total pressure. Some of these effects, such as turbulent pressure (see Rasia et al. (2004)), are included

in all current high-resolution hydrodynamic simulations of galaxy clusters. Initial attempts have also been made to include such effects as magnetic fields (e.g. Dolag et al. (1999)) and cosmic rays (Pfrommer et al. 2006). Hydrodynamic simulations can provide a robust check and calibration for semi-analytic models, but continuing work is required to include all of the relevant gas physics in both methods. Possible changes in the parameters of the predicted $Y - M$ relation can be expected as models achieve greater realism.

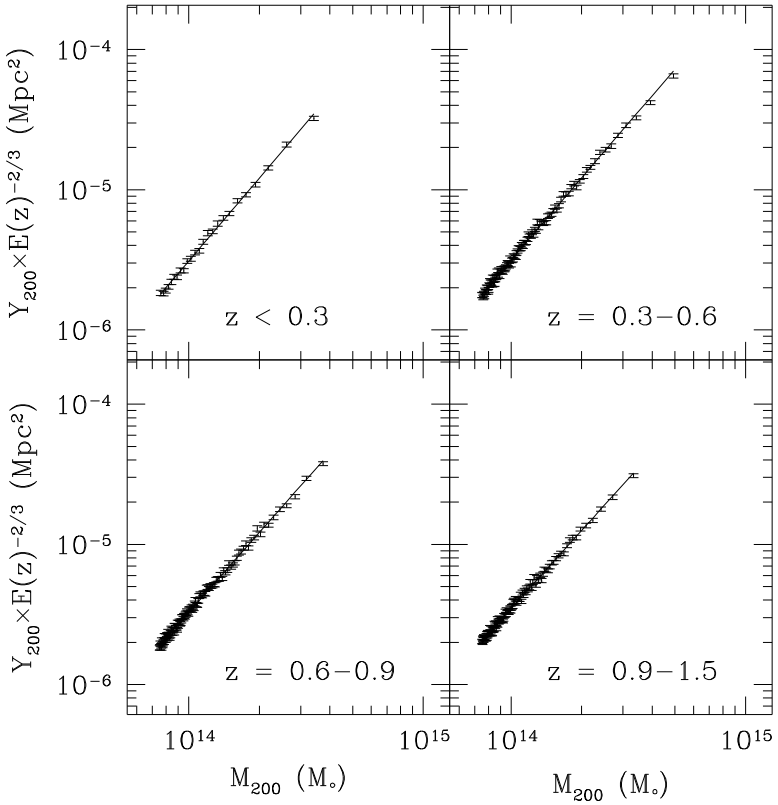

Figure 2.6 $Y_{200} \times E(z)^{-2/3}$ vs. M_{200} for four different redshift regions. As in Figure 2.5, each point represents the mean of 250 clusters, and error bars represent the error on the mean. The parameters and reduced χ^2 for the best-fit lines are given in Table 2.2.

2.4 Cluster Detection

To study cluster detection, three maps of the ACT strip are first created (combining the primary microwave background, infrared and radio point sources, and the full SZ effect) at the frequency channels of 145, 215, and 280 GHz. The ACT instrument is simulated by convolving the ACT strip maps at 145, 215, and 280 GHz with a Gaussian beam of full-width at half-maximum equal to 1.7', 1.1', and 0.93' respectively. Gaussian random noise is then added to the maps of

$M_{200} > 0.75 \times 10^{14}\ M_\odot$	α	σ_α	β	σ_β	reduced χ^2	clusters	bins
$z > 0$	1.876	0.005	-5.4774	0.0009	1.004	90750	363
$z < 0.3$	1.96	0.02	-5.509	0.004	1.18	6250	25
$z = 0.3 - 0.6$	1.944	0.009	-5.502	0.002	1.38	24750	99
$z = 0.6 - 0.9$	1.88	0.01	-5.484	0.002	1.14	27250	109
$z = 0.9 - 1.5$	1.85	0.01	-5.457	0.002	1.02	27500	110
$z > 1.5$	1.82	0.05	-5.421	0.004	0.66	4250	17

Table 2.2 Best-fit parameters for the best-fit lines depicted in Figures 2.5 and 2.6, fit using the power-law given in equation 2.12.

σ equal to 2μK, 3.3μK, and 4.7μK per beam for the three frequencies respectively. The above are preliminary detector noise estimates for extensive dedicated observations of the ACT strip. We produce a single map of the SZ clusters by applying a multi-frequency Wiener filter to the three ACT maps. This filter requires a model power spectrum of the first-order thermal SZ signal from the clusters (see eq. 2.6). We first use a spectrum derived from the simulations themselves, and then one derived from the analytic prescription given by Komatsu & Seljak (2002) to test the sensitivity of the filter performance on the input cluster model. Clusters are then identified within the filtered map using a simple peak-finding algorithm. These clusters are matched to a catalog documenting the input map. From this matching process, we determine the completeness and purity of our detected cluster sample.

2.4.1 Multi-Frequency Wiener Filter

In the literature, a number of different filters have been employed to extract the SZ signal from microwave simulations (see introduction for references). Two commonly employed filters are matched or scale-adaptive filters and Wiener filters. Matched filters make an explicit assumption about cluster profiles while Wiener filters assume knowledge of the SZ power spectrum. Both have qualitatively similar shapes: they suppress the primary microwave background at large scales and noise at small scales. Our motivation for choosing to use a Wiener filter stems from the fact that it recovers the minimum variance SZ map and is simple to implement. We compare our results with Melin et al. (2006) who employ a scale-adaptive filter and find a Wiener filter yields comparable results. We also use two different Wiener filters and find the differences are minor.

Below we describe the map filter in detail. We wish to recover one filtered map (of clusters) from several ACT maps (at three different frequencies). The latter are described by the data vector $\boldsymbol{d}$. We write $\boldsymbol{d} = \mathrm{R}\boldsymbol{s} + \boldsymbol{n}$, where R is the instrument response to the Compton-y signal

map $\boldsymbol{s}$ (see eq. 2.5), and $\boldsymbol{n}$ is the noise. In this notation, R includes both the frequency dependence of the first-order thermal SZ signal (see eq. 2.6) and the convolution with the beam. The noise $\boldsymbol{n}$ includes detector noise, primary microwave background, point sources, and contributions to the SZ signal other than from the first-order thermal SZ. We denote the covariance of the signal, noise, and data by $\mathrm{S} = \langle \boldsymbol{s}\boldsymbol{s}^\dagger \rangle$, $\mathrm{N} = \langle \boldsymbol{n}\boldsymbol{n}^\dagger \rangle$, and $\mathrm{D} = \langle \boldsymbol{d}\boldsymbol{d}^\dagger \rangle = \mathrm{RSR}^\dagger + \mathrm{N}$, assuming signal and noise are largely uncorrelated.

The multi-frequency Wiener filter is given by

$$\mathrm{W} = \mathrm{SR}^\dagger \left[\mathrm{RSR}^\dagger + \mathrm{N}\right]^{-1} = \mathrm{SR}^\dagger \mathrm{D}^{-1}, \tag{2.13}$$

and it gives the least-squares signal map reconstruction via $\hat{\boldsymbol{s}} = \mathrm{W}\boldsymbol{d}$. Here we are assuming statistically homogeneous signal and noise, so all the covariances are (block) diagonal in the Fourier representation: they are the auto and (frequency) cross-spectra. This makes the application of the Wiener filter straightforward: we Fourier transform the ACT maps, apply the filter, and inverse Fourier transform to obtain the SZ cluster map. (See Tegmark & Efstathiou (1996) for a useful reference on Wiener filtering.)

2.4.2 Filtering Maps

To filter the maps, we divide the ACT strip (with SZ, primary microwave background, and point sources combined) into roughly $4^\circ \times 3.25^\circ$ patches. The above dimensions are chosen to give square patches in pixel space. To compute D, the power and cross-power spectra for each patch are calculated and averaged over the whole strip. For the first model cluster power spectrum (S), we compute the spectrum from the simulations in a similar fashion. Later we also use the semi-analytic spectrum of Komatsu & Seljak (2002).

To avoid aliasing of signal at the edges of each patch, we use an overlap-and-save method to filter overlapping pieces of the map. This permits us to discard all the vertical edges (edges of constant right ascension) on the patch borders (Press et al. 1997). In this way, we remove any discontinuities in the filtered map at the boundaries of the patches. The horizontal edges are less of a concern since they can be discarded after the whole strip is filtered. This filtering procedure provides a filtered map of the entire ACT strip consisting of the recovered SZ signal.

2.4.3 Identifying Clusters

Clusters are identified by searching for all peaks in the filtered map above a given threshold value. The threshold cuts we apply are 1, 2, and 3 times the standard deviation of the filtered

map. A peak is identified simply as a pixel with a larger value than any pixel within a radius $r = 6p$ around it, where p is the pixel size ($p \approx 0.21'$ for these maps). We choose this radius both because $\approx 1.3'$ is a typical cluster size and in an effort to be consistent with Melin et al. (2006) for comparison purposes. Once a list of peaks is compiled, the peaks are matched to clusters in the input cluster catalog. We identify a match if the peak and catalog cluster are within a distance r of one another. Multiple peaks matching a single catalog cluster are allowed, as are multiple catalog clusters matching a single peak. Follow-up observations to determine cluster redshifts should sort these cases out. Any peak that is not within r of any catalog cluster, is flagged as a false detection.

It is possible that some peaks match catalog clusters just by chance alignment. However, since clusters down to only $5 \times 10^{13} M_{\odot}$ are included, all the clusters in the simulation are comparable to or above ACT instrument noise, and thus are in principle detectable. So we accept that some small fraction of the simulation clusters may be detected by chance alignment with spurious peaks and do not try to distinguish these cases from real matches.

2.4.4 Results

First we examine the case when the three-frequency ACT strip maps contain no radio or infrared point sources. The completeness and number of detected clusters per deg^2 are given in Figure 2.7 as a function of both M_{200} and Y_{200} (the latter measured as a solid angle in units of arcmin^2). The dashed, dotted, and dash-dotted curves represent the 1-σ, 2-σ, and 3-σ threshold cuts respectively, and the solid line represents the simulation mass function. The purity of each cluster sample is given in the legend (purity = 1 - fraction of false-positive detections; completeness = number of detected clusters/number of input clusters). In the absence of point sources, using a 3-σ threshold cut, our sample of detected clusters is 96% complete down to $2 \times 10^{14} M_{\odot}$ with only 4% contamination from false positives. The completeness as a function of Y_{200} and purity are comparable to that found by Melin et al. (2006) when they investigated a no-point-source case for the South Pole Telescope (SPT) using a matched filter and simulated clusters that perfectly matched their filter.

In the completeness versus Y_{200} plot, there is a sharp decrease in the completeness from 1 to 0.8 at $Y_{200} = 2 \times 10^3$ arcmin^2. This effect is caused by a single cluster at $z \approx 0.04$ with $M_{200} \approx 8 \times 10^{13} M_{\odot}$. Since this cluster is so nearby, it extends over many pixels, and thus has a large Y_{200} in units of arcmin^2. However, its signal in each pixel is below that of the 1-σ threshold cut, so it is not detected. If the plot had been made with Y_{200} in units of physical area

(Mpc^2), this feature would disappear. Therefore, this feature is an artifact reflecting the fact that arcmin^2 is not a unit intrinsic to a cluster. It also suggests that for detecting extended, low-redshift clusters, searching for a peak pixel is not the best method. Profile-fitting may provide a better alternative in this case.

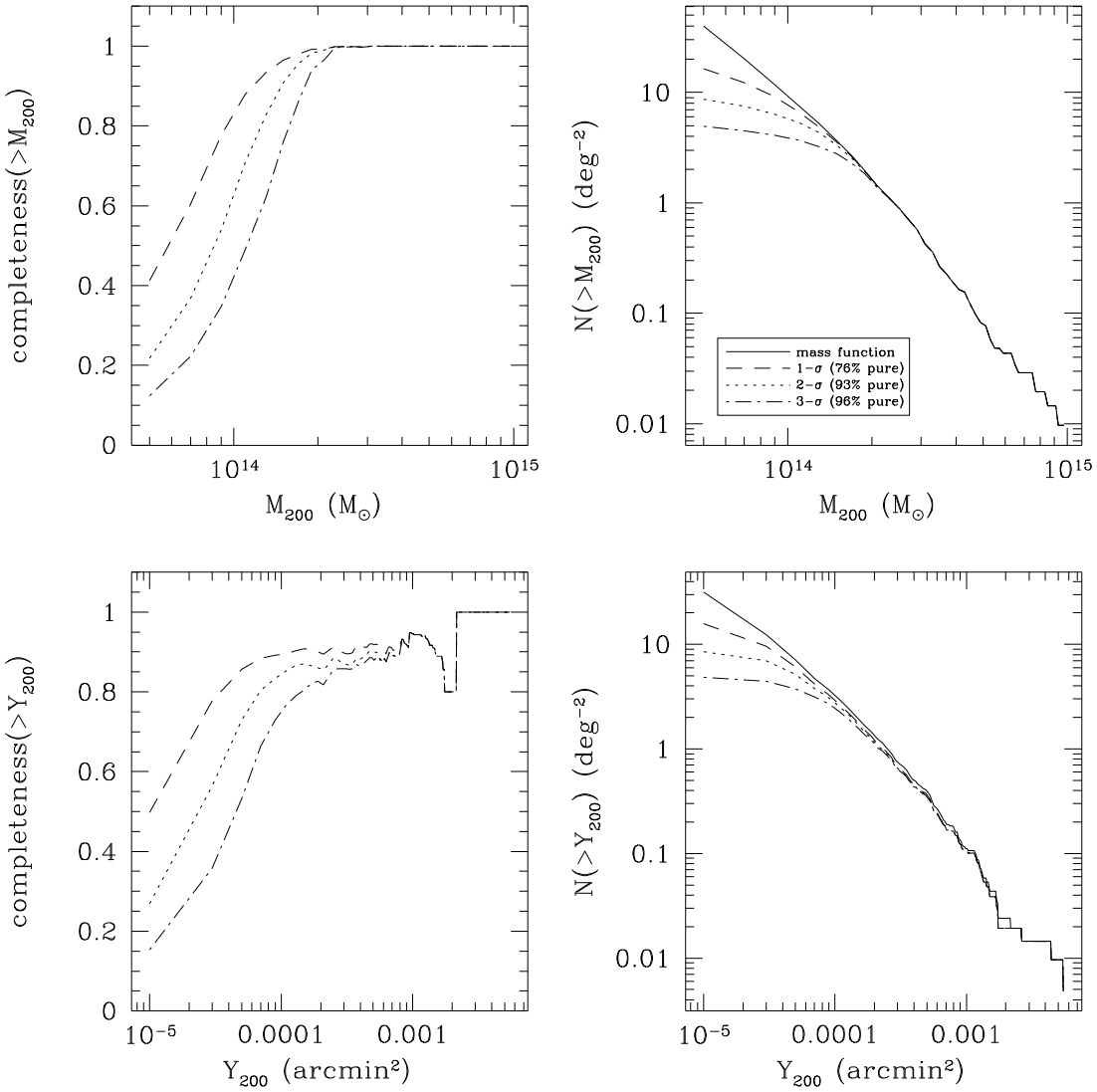

Figure 2.7 Completeness and purity of the detected cluster sample with ACT instrument specifications, in the case of no point sources. Different curves represent 1-σ, 2-σ, and 3-σ threshold cuts in the detection algorithm, where σ is the standard deviation of the filtered map. The solid curve represents the simulation mass function. The purity of each cluster sample is given in the legend. See text for further details.

Next, infrared point sources are added to the three-frequency ACT maps following the prescription described in §2.2.3. Infrared sources up to a flux limit of ≈ 0.4 Jy at 145 GHz are included since the number of sources with higher flux is effectively zero for the area of the

ACT strip given the above prescription. Figure 2.8 shows the cluster detection results after adding this population of point sources. For this case, using a 3-σ threshold cut, the detected cluster sample is 95% complete down to $3 \times 10^{14} M_{\odot}$ with 14% contamination from false-positive detections. The percentage of false-positives is comparable to that found by Melin et al. (2006) when they used N-body, as opposed to spherical, clusters for their no-point-source case. A direct comparison of completeness, including infrared point sources, with their work is difficult because we do not use isothermal, spherical clusters and we include clusters down to a lower mass limit, which crowds the field and increases confusion.

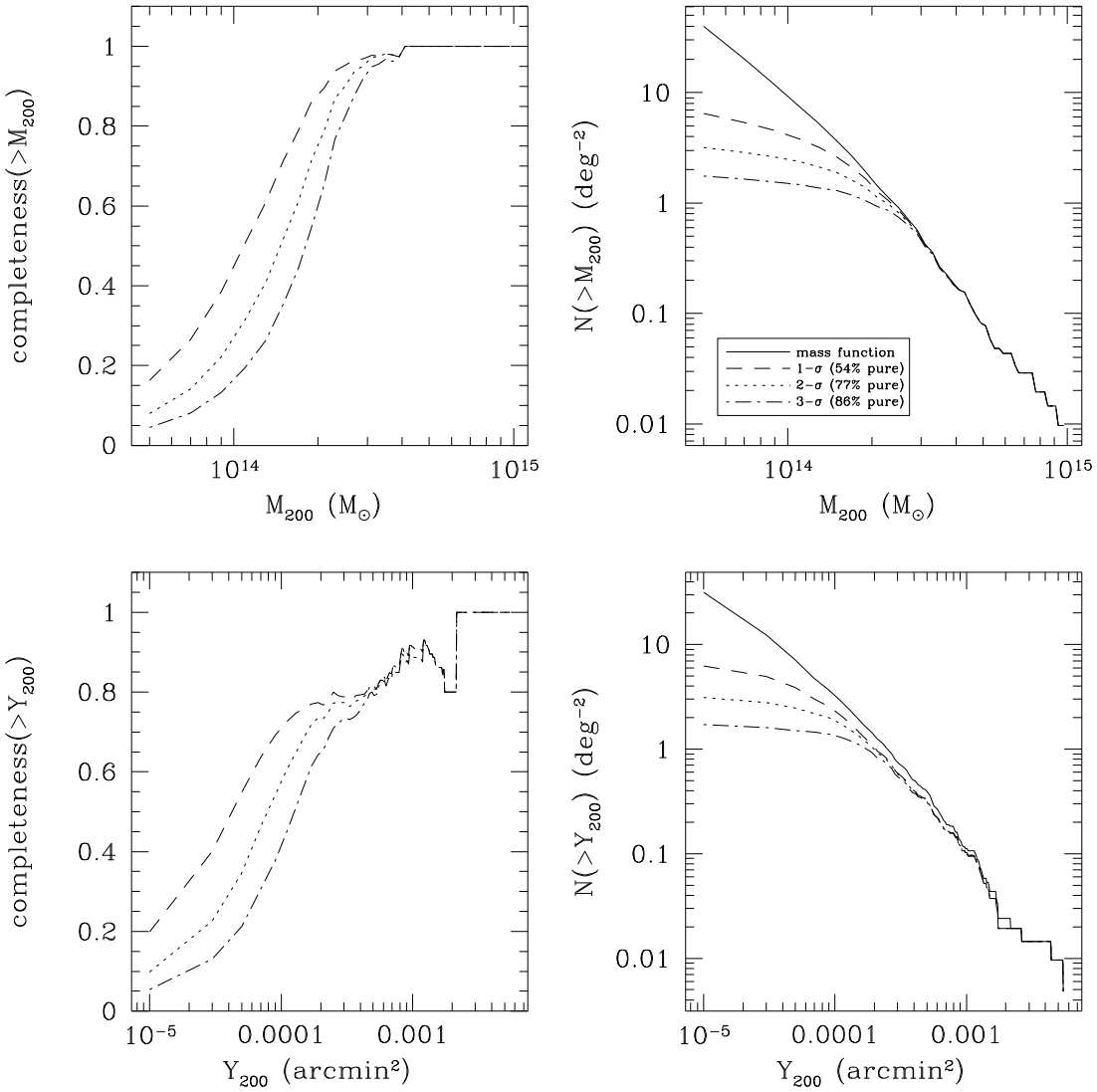

Figure 2.8 Completeness and purity of the detected cluster sample in the case of infrared point sources only.

We further investigate the case where both infrared and radio point sources are added to

the three-frequency ACT strip maps. The radio sources follow the prescription described in §2.2.3. Figure 2.9 shows the cluster detection results including radio sources in the ACT maps below three different flux limits (3.5 mJy, 35 mJy, and 350 mJy at 145 GHz). All the curves correspond to cluster detection using a 3-σ threshold cut. The dashed curve shows that if all the radio sources above 3.5 mJy at 145 GHz are removed from the three-frequency ACT maps, the infrared-point-source-only case is recovered, depicted in Figure 2.8. If all the radio sources above 35 mJy at 145 GHz are removed from the three ACT maps, we obtain results that are of only slightly lower quality than the previous case. These results can be understood by noting that the inclusion of radio sources below 35 mJy and infrared sources increases the average power in the simulated ACT strip on scales of a few arcminutes by roughly an order of magnitude, as compared to not including point sources. The inclusion of all the radio sources above 35 mJy increases the power on these scales by several orders of magnitude more. This large increase in noise power is why these few very bright sources limit cluster detection with this technique. For an arcmin^2 beam at 145 GHz, 3.5 mJy and 35 mJy correspond to $\approx 100\mu$K and $\approx 1000\mu$K respectively. Thus achieving the removal of radio sources above the former flux limit may require interferometric observations of the ACT strip at a lower frequency (e.g. with the Australia Telescope Compact Array (ATCA) at $\approx$ 20 GHz). Achieving the latter flux limit of radio sources is most likely possible with ACT alone. (Sources of $\approx 1000\mu$K should be easy to identify, and we find $\approx$ 700 of them in our simulations of the ACT strip, which is not an unmanageable number to remove.) Assuming removal of radio sources above 35 mJy at 145 GHz, our detected cluster sample is 90% complete down to $3 \times 10^{14} M_{\odot}$ and 84% pure.

The filter used in obtaining the above results was created using the Compton-y power spectrum from the simulations themselves. Since we shall not know beforehand the true cluster power spectrum, we remake the filter using a Compton-y power spectrum derived analytically from the prescription in Komatsu & Seljak (2002). With this filter, we repeat the above exercise. Figure 2.10 displays the cluster detection results using this filter and adding both infrared and radio point sources. The different curves again correspond to the three different flux cuts of radio sources, and a 3-σ threshold cut is used for them all. For the three flux cut cases, there is a slight increase in completeness of the cluster sample as compared to Figure 2.9. However, there is also a slight decrease in the purity of the cluster sample. If we compare the first-order thermal SZ power spectrum from the simulations and derived analytically (Fig. 2.4), we see that the filter made with the analytic power spectrum leaves more small scale power in the filtered map. This increases the sample completeness, but also decreases its purity, as more point sources are left in the map as well. Overall, however, the difference in using the analytic

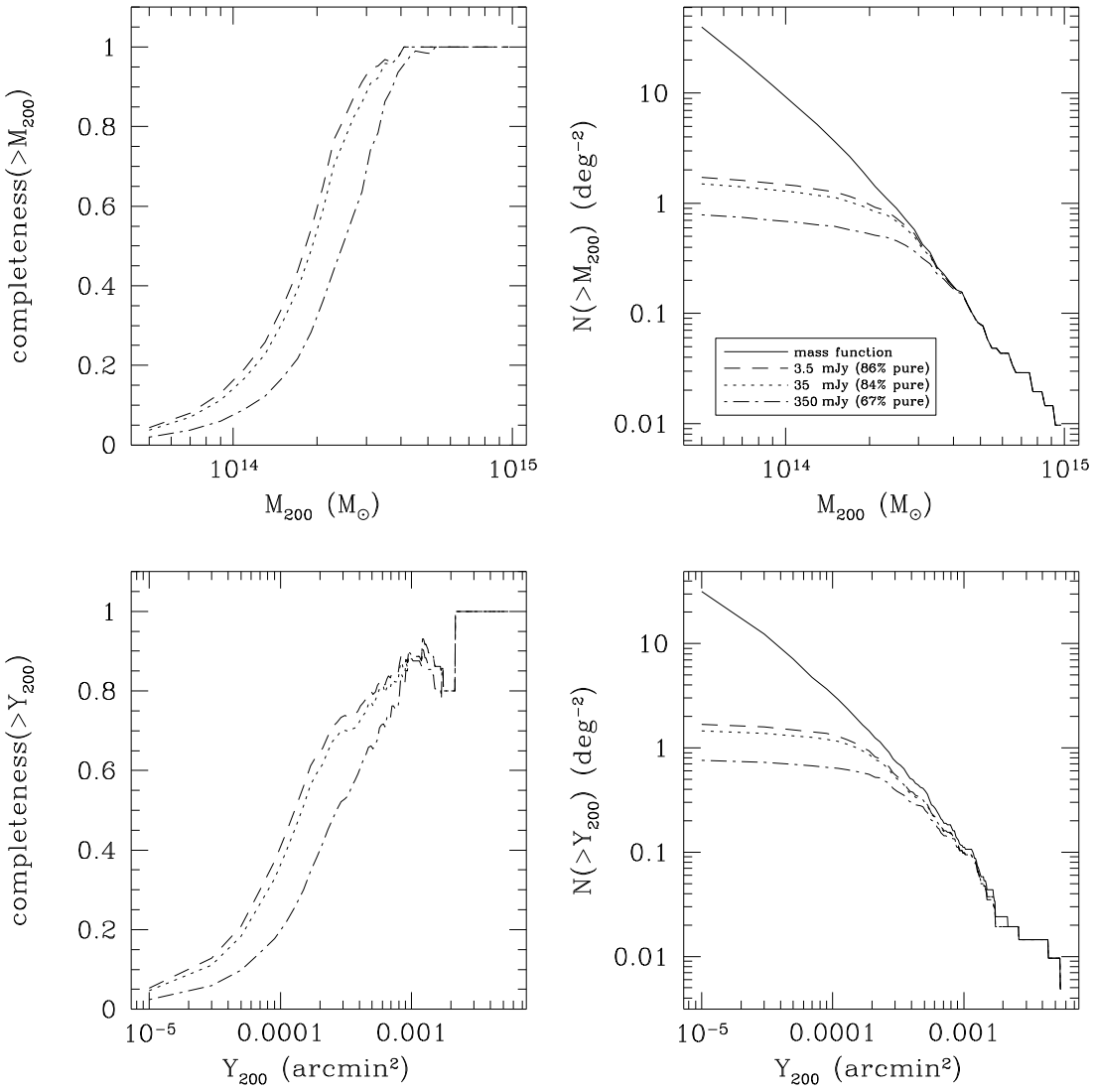

Figure 2.9 Completeness and purity when both infrared and radio sources are included. A 3-σ cut is used for all the curves. The different curves represent different flux cuts at 145 GHz for the radio sources. If all the radio sources above 3.5 mJy at 145 GHz are removed from the three-frequency ACT maps, then we recover the results with only infrared point sources included. Removing all sources above 35 mJy at 145 GHz gives results that are only slightly degraded compared to the former case.

power spectrum in the filter, as compared to the power spectrum from the simulations, is small. This suggests that the performance of the filter is not overly sensitive to how the cluster physics is modeled when constructing it.

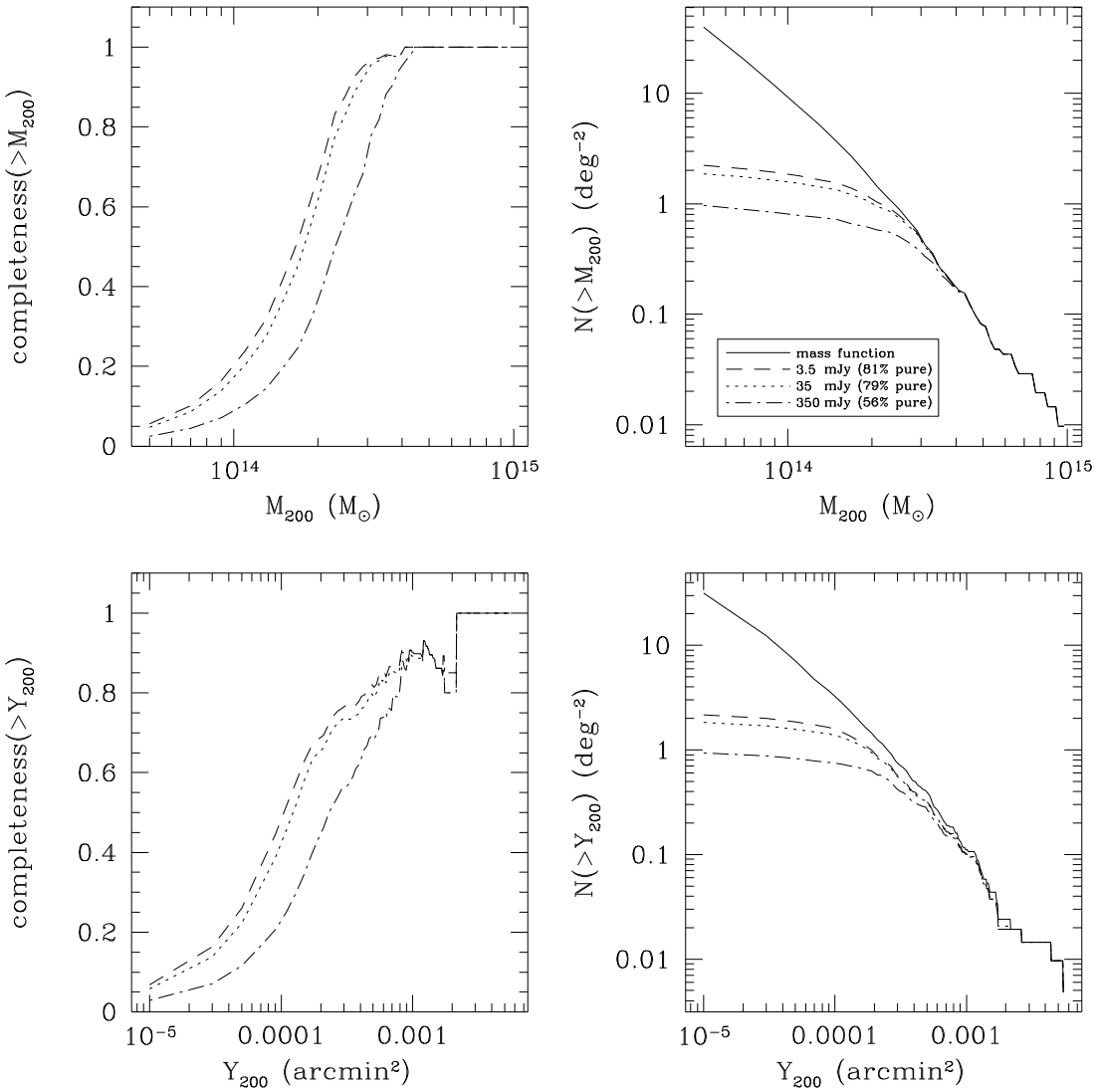

Figure 2.10 Completeness and purity of the detected cluster sample for the cases described in Figure 2.9, but this time using a filter constructed with a cluster Compton-y power spectrum derived analytically from Komatsu & Seljak (2002), instead of taken directly from the simulations. The completeness is slightly increased and the purity slightly decreased as compared to the previous Figure, but overall the difference is small.

2.5 Future Work

In this work, we did not correlate the radio and infrared point sources with the clusters. This was due to a lack of observational data regarding these correlations. If either population is both strongly correlated with clusters and exhibits a relatively flat spectrum between the infrared/radio regime and the microwave, then some further percentage of clusters may fail to be detected. Recent BIMA and OVRO observations targeting massive galaxy clusters at 28.5 GHz suggest an overabundance of mJy radio sources in these massive clusters as opposed to non-cluster fields (Coble et al. 2007). However, they also find a steeper spectral index for these sources as compared to the brighter, rarer population of radio sources found by WMAP (Bennett et al. 2003b). If their spectral index steepens further above 30 GHz, these former sources may not be an issue. But if their slope flattens out, some of these sources may fill-in the SZ decrement of some percentage of clusters at 145 GHz. Without a better understanding of these correlations and observations of these point sources in the range of 145 to 280 GHz, it is difficult to model both infrared and radio sources more realistically. Upcoming microwave surveys and follow-up or concurrent radio and infrared observations overlapping the survey areas will hopefully clarify these current unknowns. It is useful to keep in mind that, for constraining cosmology, obtaining a large number of detected clusters is less important than obtaining a solid understanding of the selection criteria. So if point sources affect cluster detection more significantly than anticipated, as long as this effect can be accurately characterized, it should not pose an overwhelming hurdle for cosmological investigations.

Some further avenues of investigation that we did not cover in this work include the following. The instrument noise can be more realistically modeled than we have done here, and atmospheric noise can be included. The lensing of the primary microwave background and point sources by clusters can be modeled to study its effect on cluster detection and SZ flux recovery. Moreover, the optimal recovery of cluster SZ flux, which is an issue distinct from cluster detection, should be investigated. This will aid in flux - mass identifications and SZ component separation. Some recent work addressing the later issue can be found in Melin et al. (2006). We also by no means suggest that Wiener filtering is the ideal cluster detection tool, and further study in this direction is also warranted.

2.6 Conclusion

New microwave instruments have the potential to detect many galaxy clusters out to redshift z=1 and beyond by their SZ signature. These galaxy clusters provide information about the

growth of structure, which in turn constrains cosmology. However, the SZ signal is embedded within the signals from the primary microwave background, radio and infrared point sources that still have significant flux in the microwave regime, and galactic emission. Thus, in an effort to study the detection of clusters via their SZ effect, we simulated the microwave-sky over both the proposed ACT observing region and a parallel strip centered at $\delta = -5$ degrees. To realistically model the small scale cluster physics, which affects the SZ signal, we combined an N-body simulation with an analytic gas model (Ostriker et al. 2005; Bode et al. 2007). This allowed us to model cluster processes such as star formation and feedback over much larger volumes than can currently be achieved by hydrodynamic simulations. One product of these cluster simulations is that we are also able to study features in the SZ flux - mass scaling relation, such as its slope and normalization and their evolution with redshift. Knowledge of this relation is necessary to connect SZ flux to cluster mass, which is the quantity of interest for cosmology.

In investigating the relation between SZ flux and mass, roughly 10^5 clusters from our N-body plus gas simulations are fit to the power-law relation given in equation 2.12. The best-fit power-law index is found to be $\alpha = 1.876 \pm 0.005$, and the reduced χ^2 to be 1.004. This slope is steeper than 5/3, which is the expectation for the self-similar model. This steeper slope is consistent with the inclusion of feedback from both active galactic nuclei and supernovae in these simulations which serves to lower the SZ flux more for lower-mass clusters. This slope is understandably steeper than that for hydrodynamic simulations, which do not include feedback from active galactic nuclei and thus have a lower amount of overall feedback than in this simulation. We find some redshift dependence for both the power-law index and normalization of this relation. This is expected since clusters are not in fact self-similar, and because star formation and cluster feedback are redshift dependent in our simulations. The steepening of the power-law index at lower redshifts is consistent with more star formation and feedback occurring at later times. Considering only the higher mass clusters, $M_{200} > 2 \times 10^{14} M\odot$, we find a flatter slope of $\alpha = 1.81 \pm 0.02$ with a reduced χ^2 of 1.14. We also see less obvious evolution of the slope and normalization with redshift. This is consistent with the higher mass clusters being less sensitive to feedback processes. It should be noted that the details of this $Y - M$ relation can change as additional sources of non-thermal pressure support such as magnetic fields, cosmic rays, and turbulence are included in semi-analytic gas models.

Our projections for cluster detection with the ACT instrument are also promising. Cluster detection was investigated under varying levels of point source contamination utilizing a multi-frequency Wiener filter and peak-finding algorithm. These results suggest that in the absence

of point sources, considering only peaks above 3-σ in the filtered map, ACT can obtain a cluster catalog that is 96% complete above $2 \times 10^{14} M_{\odot}$ and 96% pure (4% false-detections). The inclusion of infrared sources results in a catalog that is 95% complete above $3 \times 10^{14} M_{\odot}$, and 86% pure. When all radio sources are included in addition, with no flux cutoff, we find that the noise from the brightest radio sources interferes significantly with cluster detection using this technique. However, if the brightest sources are removed from the ACT maps, there is a considerable improvement. Removing all radio sources above 35 mJy at 145 GHz from the three-frequency ACT maps results in a catalog that is 90% complete above $3 \times 10^{14} M_{\odot}$ and 84% pure. Removing all radio sources above 3.5 mJy at 145 GHz gives the same results as the inclusion of only infrared point sources. These results are encouraging, since 35 mJy sources should be easily identifiable and removable from ACT maps without need for further observations at alternate frequencies.

This study was repeated using a cluster model in our filter that differed from that in our simulations. Doing this produced only a small change in the cluster detection results. This suggests that the filter performance is not very sensitive to the details of the cluster model used to create it. As a result, efforts to characterize the selection function are made easier.

The potential of new microwave instruments to provide knowledge about cluster physics and cosmology is substantial, as our results further confirm. It is hoped that the simulations created to pursue the above studies will serve as a useful tool for future investigations toward making this potential a reality.

Bibliography

Aghanim, N., de Luca, A., Bouchet, F. R., Gispert, R., & Puget, J. L. 1997, A&A, 325, 9

Bahcall, N. A., & Fan, X. 1998, ApJ, 504, 1

Barbosa, D., Bartlett, J. G., Blanchard, A., & Oukbir, J. 1996, A&A, 314, 13

Bennett, C. L., et al. 2003a, ApJS, 148, 1

Bennett, C. L., et al. 2003b, ApJS, 148, 97

Bertschinger, E. 2001, ApJS, 137, 1

Birkinshaw, M. 1999, Phys. Rep., 310, 97

Bode, P., Ostriker, J. P., Weller, J., & Shaw, L. 2007, ApJ, 663, 139

Bode, P., & Ostriker, J. P. 2003, ApJS, 145, 1

Bode, P., Ostriker, J. P., & Xu, G. 2000, ApJS, 128, 561

Borys, C., Chapman, S., Halpern, M., & Scott, D. 2003, MNRAS, 344, 385

Calabretta, M. R., & Greisen, E. W. 2002, A&A, 395, 1077

Carlstrom, J. E., Holder, G. P., & Reese, E. D. 2002, ARA&A, 40, 643

Challinor, A., & Lewis, A. 2005, Phys. Rev. D, 71, 103010

Coble, K., Bonamente, M., Carlstrom, J. E., Dawson, K., Hasler, N., Holzapfel, W., Joy, M., La Roque, S., Marrone, D. P., & Reese, E. D., 2007, AJ, 134, 897

da Silva, A. C., Kay, S. T., Liddle, A. R., & Thomas, P. A. 2004, MNRAS, 348, 1401

Dolag, K., Bartelmann, M., & Lesch, H. 1999, A&A, 348, 351

Eke, V. R., Cole, S., & Frenk, C. S. 1996, MNRAS, 282, 263

Finkbeiner, D. P., Davis, M., & Schlegel, D. J. 1999, ApJ, 524, 867

Górski, K. M., Hivon, E., Banday, A. J., Wandelt, B. D., Hansen, F. K., Reinecke, M., & Bartelmann, M. 2005, ApJ, 622, 759

Güsten, R., et al. 2006, in Ground-based and Airborne Telescopes. Edited by Stepp, Larry M.. Proceedings of the SPIE, Volume 6267, pp. 626714 (2006).

Haiman, Z., Mohr, J. J., & Holder, G. P. 2001, ApJ, 553, 545

Herranz, D., Sanz, J. L., Barreiro, R. B., & Martínez-González, E. 2002a, ApJ, 580, 610

Herranz, D., Sanz, J. L., Hobson, M. P., Barreiro, R. B., Diego, J. M., Martínez-González, E., & Lasenby, A. N. 2002b, MNRAS, 336, 1057

Hinshaw, G., et al. 2006, ArXiv Astrophysics e-prints

Horner, D. 2001, Ph.D. thesis, University of Maryland

Jenkins, A., Frenk, C. S., White, S. D. M., Colberg, J. M., Cole, S., Evrard, A. E., Couchman, H. M. P., & Yoshida, N. 2001, MNRAS, 321, 372

Juin, J. B., Yvon, D., Réfrégier, A., & Yèche, C. 2007, A&A, 465, 57

Kneissl, R., Jones, M. E., Saunders, R., Eke, V. R., Lasenby, A. N., Grainge, K., & Cotter, G. 2001, MNRAS, 328, 783

Knox, L., Holder, G. P., & Church, S. E. 2004, ApJ, 612, 96

Komatsu, E., & Seljak, U. 2002, MNRAS, 336, 1256

Kosowsky, A. 2003, New Astronomy Review, 47, 939

Li, C.-T., et al. 2006, in Millimeter and Submillimeter Detectors and Instrumentation for Astronomy III. Edited by Zmuidzinas, Jonas; Holland, Wayne S.; Withington, Stafford; Duncan, William D.. Proceedings of the SPIE, Volume 6275, pp. 62751I (2006).

Lima, M., & Hu, W. 2005, Phys. Rev. D, 72, 043006

Loh, M., et al. 2005, p. 1225

Majumdar, S., & Mohr, J. J. 2003, ApJ, 585, 603

Majumdar, S., & Mohr, J. J. 2004, ApJ, 613, 41

McCarthy, I. G., Balogh, M. L., Babul, A., Poole, G. B., & Horner, D. J. 2004, ApJ, 613, 811

Melin, J.-B., Bartlett, J. G., & Delabrouille, J. 2005, A&A, 429, 417

Melin, J.-B., Bartlett, J. G., & Delabrouille, J. 2006, A&A, 459, 341

Motl, P. M., Hallman, E. J., Burns, J. O., & Norman, M. L. 2005, ApJ, 623, L63

Nagai, D. 2006, ApJ, 650, 538

Nagamine, K., Ostriker, J. P., Fukugita, M., & Cen, R. 2006, ApJ, 653, 881

Nozawa, S., Itoh, N., & Kohyama, Y. 1998, ApJ, 508, 17

Ostriker, J. P., Bode, P., & Babul, A. 2005, ApJ, 634, 964

Oukbir, J., & Blanchard, A. 1992, A&A, 262, L21

Pfrommer, C., Ensslin, T. A., Springel, V., Jubelgas, M., & Dolag, K. 2006, ArXiv Astrophysics e-prints

Pierpaoli, E., Anthoine, S., Huffenberger, K., & Daubechies, I. 2005, MNRAS, 359, 261

Press, W. H., Teukolsky, S. A., Vetterling, W. T., & Flannery, B. P. 1997, Numerical Recipes in C (2nd ed.; Cambridge: Cambridge University Press)

Rasia, E., Tormen, G., & Moscardini, L. 2004, MNRAS, 351, 237

Reiprich, T. H., & Böhringer, H. 2002, ApJ, 567, 716

Rosati, P., Borgani, S., & Norman, C. 2002, ARA&A, 40, 539

Ruhl, J., et al. 2004, in Millimeter and Submillimeter Detectors for Astronomy II. Edited by Jonas Zmuidzinas, Wayne S. Holland and Stafford Withington Proceedings of the SPIE, Volume 5498, pp. 11-29 (2004)., ed. C. M. Bradford, P. A. R. Ade, J. E. Aguirre, J. J. Bock, M. Dragovan, L. Duband, L. Earle, J. Glenn, H. Matsuhara, B. J. Naylor, H. T. Nguyen, M. Yun, & J. Zmuidzinas, 11

Runyan, M. C., et al. 2003, ApJS, 149, 265

Schaefer, B. M., & Bartelmann, M. 2006, ArXiv Astrophysics e-prints

Schlegel, D. J., Finkbeiner, D. P., & Davis, M. 1998, ApJ, 500, 525

Schulz, A. E., & White, M. 2003, ApJ, 586, 723

Spergel, D. N., et al. 2006, ArXiv Astrophysics e-prints

Stolyarov, V., Hobson, M. P., Ashdown, M. A. J., & Lasenby, A. N. 2002, MNRAS, 336, 97

Sunyaev, R. A., & Zeldovich, Y. B. 1970, Comments on Astrophysics and Space Physics, 2, 66

Sunyaev, R. A., & Zeldovich, Y. B. 1972, Comments on Astrophysics and Space Physics, 4, 173

Tauber, J. A. 2004, Advances in Space Research, 34, 491

Tegmark, M., & Efstathiou, G. 1996, MNRAS, 281, 1297

Vale, C., & White, M. 2006, New Astronomy, 11, 207

Viana, P. T. P., & Liddle, A. R. 1996, MNRAS, 281, 323

Wang, L., & Steinhardt, P. J. 1998, ApJ, 508, 483

Wang, S., Khoury, J., Haiman, Z., & May, M. 2004, Phys. Rev. D, 70, 123008

Weller, J., & Battye, R. A. 2003, New Astronomy Review, 47, 775

Weller, J., Battye, R. A., & Kneissl, R. 2002, Physical Review Letters, 88, 231301

White, M. 2003, ApJ, 597, 650

White, M., Hernquist, L., & Springel, V. 2002, ApJ, 579, 16

Younger, J. D., Haiman, Z., Bryan, G. L., & Wang, S. 2006, ApJ, 653, 27

Chapter 3

Probing the Relation Between X-ray-Derived and Weak-Lensing-Derived Masses for Shear-Selected Galaxy Clusters: I. A781

The material in this chapter also appears in print as "Probing the Relation Between X-ray-Derived and Weak-Lensing-Derived Masses for Shear-Selected Galaxy Clusters: I. A781", Sehgal et al. 2008, ApJ, 673, 163.

3.1 Introduction

Galaxy clusters have the potential to open a new window on cosmology by serving as precision tracers of the growth of structure over cosmic time. The growth of structure can provide independent constraints on the matter density ($\Omega_{\rm M}$), the dark energy density (Ω_Λ), and the dark energy equation of state (ω), that would both verify our standard cosmological picture and take us further into understanding the nature of dark energy (e.g., Carlstrom et al. (2002)). Utilizing galaxy clusters as tracers of structure growth largely relies on knowledge of cluster masses. Ideally cluster samples would have selection criteria based on mass, and mass estimates of clusters would be based on probes of their gravitational potential. However, most large samples of clusters that exist to date are selected on the basis of their trace baryons (i.e., visible light from galaxies or X-ray emission from hot intracluster gas). Moreover, traditional probes of cluster mass (X-ray and optical) depend on the cluster's star formation history, baryon content, and assumptions about its dynamical state. Only recently have we obtained samples of clusters of significant size unbiased with respect to baryons and instead selected on the basis of their weak gravitational lensing shear.

One such sample is provided by the Deep Lens Survey (DLS), a deep BVRz' imaging survey of 20 square degrees (Wittman et al. 2002). The observations were taken with the Cerro Tololo Blanco and Kitt Peak Mayall 4-m telescopes. The primary goal of this survey is to study the growth of mass clustering over cosmic time using weak lensing. The DLS team has shown it is capable of finding new galaxy clusters using their weak-lensing signal alone (Wittman et al.

2001, 2003), and it has presented its first sample of cluster candidates from the first 8.6 square degrees of the survey (Wittman et al. 2006). The DLS survey should find ∼40 clusters when completed. The CFHT Legacy Survey Deep has also presented shear-selected clusters from a 4 square degree region and the Garching-Bonn Deep Survey has presented a sample from 19 square degrees (Gavazzi & Soucail 2007; Schirmer et al. 2007).

We have been following-up a shear-ranked sample of DLS clusters with *Chandra* and *XMM-Newton*. One goal of this X-ray follow-up is to confirm that the DLS shear-selected cluster candidates are in fact true virialized collapsed structures. Preliminary analysis for five of these clusters is presented in Hughes et al. (2004). A further goal of this X-ray follow-up is to characterize the robustness of X-ray and weak-lensing cluster mass estimates and the biases inherent in X-ray and shear-selected samples. This understanding is necessary in order to lay the groundwork for precision cosmology via larger X-ray and weak-lensing cluster surveys (utilizing, for example, Constellation-X [1] and LSST [2]). Such characterizations are facilitated by comparing weak-lensing mass estimates with X-ray mass estimates, as we elaborate on in §3.2.

Below we report our weak-lensing and X-ray mass estimates for our top ranked shear-selected cluster, Abell 781, and three surrounding clusters. We discuss details of the weak-lensing and X-ray observations in §3.3, and the details of the weak-lensing and X-ray mass estimation methods in §3.4 and §3.5. In §3.6 we discuss our results, and in §3.7 we summarize our conclusions.

3.2 Benefits of Investigating the Relation Between X-ray- and Weak-Lensing-Derived Masses for Shear-Selected Clusters

An important issue for shear-selected clusters is projection bias. The weak-lensing shear signal is sensitive to all the intervening matter between the background galaxies and the observer. This leads to a possible projection bias of shear mass estimates as non-cluster line-of-sight matter contaminates the shear signal (e.g., Metzler et al. (1999); White et al. (2002); de Putter & White (2005)). X-ray observations provide an independent way to estimate the mass. Thus to quantify the extent of this contamination, we wish to compare X-ray mass estimates to weak-lensing mass estimates for clusters that are dynamically relaxed. X-ray observations are uniquely suited to this because they offer clear indications of a cluster's dynamical state via X-ray images and temperature measurements. We impose the condition of relaxation because X-ray mass estimates are based on an assumption of hydrostatic equilibrium and are likely

[1] http://constellation.gsfc.nasa.gov/

[2] http://www.lsst.org/lsst_home.shtml

invalid for highly unrelaxed systems. The comparison of X-ray to weak-lensing mass estimates will indicate how significantly projection bias affects the latter.

To study the bias (or absence of bias) inherent in X-ray and shear-selected cluster surveys, we first note that optical selection depends on star formation history and X-ray/Sunyaev-Zel'dovich selection depends on the heating of the intracluster medium. It has been proposed that up to 20% of shear-selected clusters have not yet heated their intracluster medium enough to be visible by current X-ray satellites (Weinberg & Kamionkowski 2002). This is because a significant fraction of cluster-mass overdensities are likely nonvirialized and still in the process of gravitational collapse. These nonvirialized overdensities should produce much weaker X-ray emission than that from a fully virialized cluster of the same mass. Differentiating this population from false-positive shear signals due to unrelated line-of-sight projections that appear as single larger mass concentrations, will be a challenge. Such a 'dark lens' cluster candidate was reportedly found by Erben et al. (2000) via weak-lensing observations centered on Abell 1942. This detection was followed-up by Gray et al. (2001) in the infrared with no obvious luminous counterpart detected. Several more apparent 'dark lenses' are reported in Koopmans et al. (2000), Umetsu & Futamase (2000), and Miralles et al. (2002). If such 'dark lenses' exist, there should exist a continuum of clusters between those which just satisfy $M_{xray} < M_{weaklens}$ and those which simply show no detectable X-ray counterpart to their weak-lensing signal. Characterizing and quantifying the clusters for which $M_{xray} < M_{weaklens}$ will allow greater understanding of which clusters are missed by traditional samples and the percentage of false-positive detections that are inherent in shear surveys.

The ratio of $M_{xray}/M_{weaklens}$ may also prove to be a good diagnostic of the dynamical relaxation of a cluster. Recent findings based on 22 high X-ray luminosity, low-redshift ($0.05 < z < 0.31$) clusters, selected on the basis of their high X-ray emission and targeted for weak-lensing follow-up with the ESO VLT, suggest X-ray cluster mass estimates larger than weak-lensing mass estimates positively correlate with clusters being dynamically unrelaxed (Cypriano et al. 2004). Naively one would expect this theoretically because events (such as mergers) that disrupt a cluster's equilibrium introduce transient shock heating of its intracluster gas. Calculating X-ray cluster masses using an assumption of hydrostatic equilibrium and a higher temperature than the cluster would have if relaxed, results in an overestimate of the true mass. However, recent work based on hydrodynamic cluster simulations suggests X-ray mass estimates are biased low for unrelaxed clusters because only a portion of the kinetic energy of the merging system is converted into thermal energy of the intracluster medium, for even an advanced merger, while the mass of the merging system has already increased (e.g., Kravtsov et al. 2006).

Comparing M_{xray} to $M_{weaklens}$ for our shear-selected clusters would determine whether X-ray mass estimates are biased high or low for unrelaxed clusters and whether this ratio can be used as a universal diagnostic of cluster dynamical state. Such a universal diagnostic would prove useful in investigating cluster evolution.

Finally, there have been several reported instances of clusters that have an X-ray signal but no apparent weak-lensing counterpart (Cypriano et al. 2004; Dahle et al. 2002). We have detected such a cluster while following-up our highest shear-ranked cluster with *XMM-Newton*. This cluster did not appear in the original shear maps made for the DLS survey but is readily apparent in *XMM-Newton* observations. The inverse of 'dark lenses', negative weak-lensing detections are not unexpected since weak lensing is a less sensitive method of cluster searching as many galaxies need to be detected behind a cluster. Also mergers could potentially boost the X-ray signal of clusters otherwise below both current X-ray and weak-lensing thresholds. It is important for understanding the limitations of weak-lensing surveys to explore what is occurring in cases such as these.

3.3 Observations

3.3.1 Weak-Lensing Observations

The Deep Lens Survey consists of five fields, each $2^\circ \times 2^\circ$ and isolated from each other. The two northern fields were observed using the Kitt Peak Mayall 4-m telescope, and the three southern fields were obtained with the Cerro Tololo Blanco 4-m telescope. Observing began in November 1999 at Kitt Peak and in March 2000 at Cerro Tololo. The deep BVRz' images were taken with 8k $\times$ 8k Mosaic imagers (Muller et al. 1998) on each telescope, which provided $35' \times 35'$ fields of view with $0.26''$ pixels and minimal gaps between the CCD devices. The observing strategy was to require better than $0.9''$ seeing in the R band, so that this band would have good, largely uniform resolution. When the seeing was worse than this, B, V, and z' images were taken. The source galaxy shapes were measured in the R band, and B, V, and z' images provided color information and photometric redshifts. Wittman et al. (2002) gives details of the field selection and survey design, and Wittman et al. (2006) gives details regarding the image processing and convergence maps.

A list of cluster candidates was compiled, based on the first 8.6 deg^2 of processed DLS data, and the candidates were ranked by their shear peak values. Multiple peaks within a $16'$ box were considered a single target for purposes of *Chandra* follow-up. A781 emerged as the top-ranked cluster candidate, with both DLS and archived *Chandra* observations indicating that

this cluster was really a complex of several clusters (Wittman et al. 2006). X-ray and optical follow-up of the A781 cluster complex was pursued as part of a larger follow-up program that will encompass a significant sample of DLS cluster candidates.

3.3.2 X-ray Observations

We were awarded 15ks of *XMM-Newton* time in cycle 2 to get a closer look at our top-ranked DLS cluster complex. This observation took place on 04 April 2003 (Obsid# 0150620201). In addition, *Chandra* had observed A781 on 03 October 2000 with the ACIS-I detector for a nominal exposure time of 10 ks (Obsid # 534). The *XMM-Newton* and *Chandra* observations revealed that the A781 cluster complex consists of a large main cluster connected to a subcluster with two smaller clusters to its east and one to its west. We shall call the largest cluster the 'Main' cluster. The subcluster to its southwest appears in the act of merging with it (see Figure 3.1). Just to the east of the Main cluster is another cluster, which we will refer to as the 'Middle' cluster, and within the same pointing, further to the east, is another cluster, hereafter 'East' cluster. The *XMM-Newton* observation also presented us with a surprise. To the west of the Main cluster there appears to be one more cluster, which we will call the 'West' cluster. This cluster did not appear in the original DLS convergence maps made for the survey, and it is also, unfortunately, out of the field of view of the *Chandra* archive observations. Table 3.1 lists the IAU designations of these clusters.

IAU Designation	Nickname
CXOU J092026+302938	Main Cluster
CXOU J092053+302800	Middle Cluster
CXOU J092110+302751	East Cluster
CXOU J092011+302954	Subcluster
XMMU J091935+303155	West Cluster

Table 3.1 IAU Designations for the clusters in the A781 cluster complex.

3.3.3 Optical Spectroscopy

Geller et al. (2005) conducted a magnitude-limited (to $R = 20.5$) spectroscopic survey in this field. They report mean redshifts of 0.302, 0.291, and 0.427 for the Main, Middle, and East clusters respectively (labeled as clusters A, B, and C in Geller et al. (2005)). These redshifts were obtained from 163, 123, and 33 cluster members respectively. No redshift errors are quoted, however given the number of cluster members and the redshift errors in the individual galaxies,

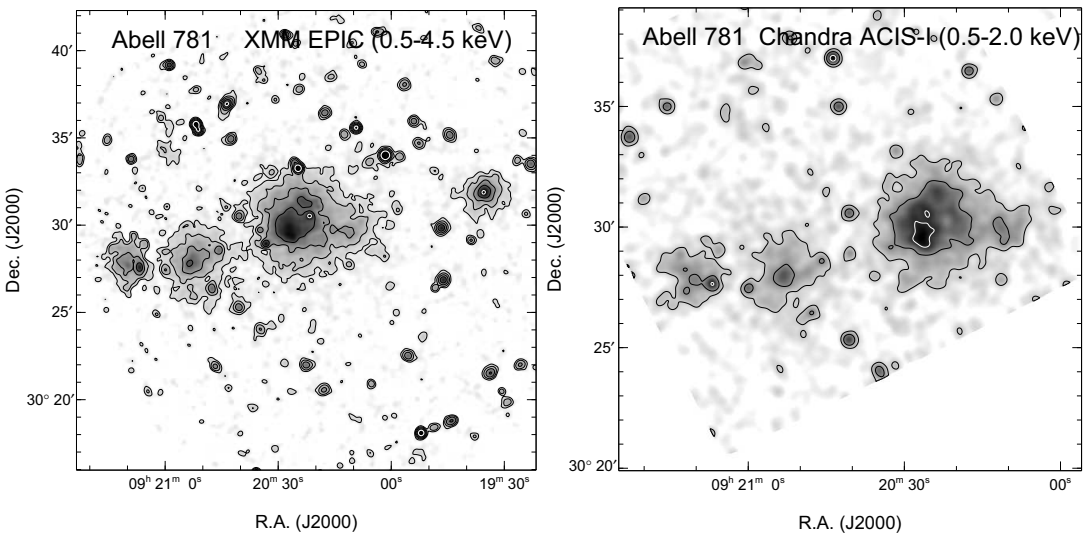

Figure 3.1 *Left panel*: *XMM-Newton* 15 ks image of the A781 cluster complex. We refer to these clusters from left to right as East, Middle, Main, and West. The contours represent 1×10^{-3} (white), 4.5×10^{-4}, 2×10^{-4}, 8.9×10^{-5}, and 4×10^{-5} cts/s/(4" square pixel). *Right panel*: *Chandra* 10 ks image of the A781 cluster complex. The contours represent 2.7×10^{-5} (white), 9.7×10^{-6}, and 3.5×10^{-6} cts/s/(2" square pixel). Note the smaller field of view of the *Chandra* image, which only covers the three clusters to the east.

the systemic redshifts of the systems should be accurate to dz of 0.0002. The rest frame line-of-sight velocity dispersions were found to be $\sigma_A = 674^{+43}_{-52}$ km s^{-1} (Main), $\sigma_B = 741^{+35}_{-40}$ km s^{-1} (Middle), and $\sigma_C = 733^{+77}_{-112}$ km s^{-1} (East) (Geller et al. 2005). According to these velocity dispersions, these cluster components appear to be similar, a result we examine further using our X-ray and weak-lensing data.

The redshift of the West cluster is not reported in Geller et al. (2005). We obtained spectroscopy of this cluster with Keck/LRIS (Oke et al. 1995) in longslit mode on 16 January 2007. We obtained secure redshifts for two member galaxies, at a mean redshift of 0.428±0.001, though clearly the quoted error is itself highly uncertain with only two members. We also observed the East cluster in longslit mode on the same night, finding a mean redshift of 0.426 ± 0.003 based on two members, in agreement with Geller et al. (2005). Thus the East and West clusters are the only two components at the same redshift, but with a transverse separation of $21'$ or 7.0 Mpc. Throughout this work we assume a ΛCDM cosmology of $h = 0.71$, $\Omega_\Lambda = 0.73$, and $\Omega_M = 0.27$ (Spergel et al. 2003).

3.4 Extracted X-ray Temperatures and Gas Density Profiles

To obtain X-ray mass estimates of these clusters, we follow the standard practice of treating the intracluster gas as a hydrostatic fluid. This assumption is reasonable for dynamically relaxed clusters since collision times for ions and electrons in the hot gas are very short compared to times scales over which the gas heats or cools or the cluster gravitational potential varies. Assuming spherical symmetry,

$$M(r) = -\frac{krT(r)}{G\mu m_p}\Big(\frac{d\ln\rho(r)}{d\ln r} + \frac{d\ln T(r)}{d\ln r}\Big), \tag{3.1}$$

where μm_p is the gas mean molecular weight, $T(r)$ and $\rho(r)$ are the gas temperature and density profiles, and $M(r)$ is the total mass within a radius r. We assume the cluster gas follows a β-model,

$$\rho(r) = \rho_{0_g}\big[1 + \big(\frac{r}{r_c}\big)^2\big]^{-\frac{3\beta}{2}}, \tag{3.2}$$

proposed by Cavaliere & Fusco-Femiano (1978). In this model, the core radius, r_c, is where the density is half the central density for a typical β of 2/3. To determine β and r_c, we note that the X-ray emissivity is proportional to the square of the cluster gas density times the cooling function, i.e., $\epsilon(r) \propto \Lambda(T(r))(n_e(r))^2$. Integrating the emissivity through the cluster line of sight gives the X-ray surface brightness Σ. Assuming a β-model for the gas density and noting that the cooling function is close to constant over the range of typical cluster temperatures yields

$$\Sigma(b) \;=\; \int_{-\infty}^{\infty}\epsilon(r)dl \;\propto\; \left(1 + \left(\frac{b}{r_c}\right)^2\right)^{-3\beta+\frac{1}{2}}, \tag{3.3}$$

where $l = \sqrt{r^2 - b^2}$ and b is the projected radius (e.g., Sarazin (1986)). We fit the radial X-ray surface brightness profile with equation 3.3 to obtain estimates for β and r_c (see §3.4.2).

The statistical quality of our data precludes the determination of a radial temperature profile. In lieu of this, we assume an NFW profile for the cluster matter density given by

$$\rho_M(r) = \frac{\rho_0}{(r/r_s)(1 + r/r_s)^2} \tag{3.4}$$

where ρ_0 is the central density and r_s is the scale radius (Navarro et al. 1996, 1997). This gives

$$M(r) = 4\pi\rho_0 r_s^3\Big(\ln(1 + \frac{r}{r_s}) + \frac{1}{1 + r/r_s} - 1\Big) \tag{3.5}$$

for the mass within a radius r. Using equation 3.1, we solve for the cluster temperature profile and then for the emission-weighted, projected, average temperature within a given aperture, which our data allow us to measure relatively precisely. We compare this predicted temperature to our measured temperature determined from X-ray spectroscopy to find the best-fit value for ρ_0 and thus the cluster mass. We describe the details of the X-ray spectroscopy below.

3.4.1 X-ray Temperatures

Analysis of Chandra Data

We downloaded the *Chandra* data from the archive and used CIAO software tools for the initial data reduction steps. The observation was carried out in full-frame timed exposure mode using very faint telemetry mode. The peak X-ray emission of the Main cluster was positioned near the center of chip I3, some 3.5′ from the on-axis "sweet" spot of the high resolution mirror. The merging subcluster to the west was imaged on chip I3, while the two other clusters toward the east were imaged on chip I1. There was no cluster X-ray emission visible on the remaining two chips of the imaging array. We note that chip S2 of the spectroscopic array was also active during this observation, but we did not utilize these data. Event pulse heights were corrected for time-dependent gain, and all grades, other than 0, 2, 3, 4, and 6, were rejected. Information contained in the very faint mode data was used to reject non–X-ray background events. The light curve of the entire imaging array (minus obvious cluster and unresolved emission) was examined and no time intervals of high or excessive background were found. The resulting live-time corrected exposure time was roughly 9900 sec. Figure 3.1 shows the 500-2000 eV band image of the ACIS-I data after exposure correction (for which the vignetting function was calculated at a monochromatic X-ray energy of 1 keV) and smoothing with a Gaussian of $\sigma \approx 10''$.

Spectral extraction regions for the clusters were determined (see Tables 3.2 and 3.3) to optimize the signal to noise ratio of the resulting spectra. Annular regions surrounding each cluster were used to generate background spectra. Obvious point sources were excluded from both source and background regions, and cluster emission was excluded from all background regions. Weighted spectral response functions were generated for each source and matching background region, including instrumental absorption due to contamination build-up on the ACIS filters.

Chandra	source	background annulus (same center as source)
Main Cluster	09:20:24.8 +30:30:20.4 2.4'	3.3' – 4.3' (minus Subcluster)
Middle Cluster	09:20:52.5 +30:28:08.4 1.6'	2.3' – 3.3' (minus East)
East Cluster	09:21:10.9 +30:28:04.2 1.5'	2.0' – 3.0' (minus Middle)
Subcluster	09:20:09.4 +30:30:02.5 0.9'	...

Table 3.2 *Chandra* cluster and background annulus extraction regions. Point sources excluded from the cluster regions are given in Table 3.3.

Xspec (version 11.3) was used for the spectral analysis. Fits were first done to the background

R.A.	Decl.	Radius
09:20:32.590	+30:29:10.49	4”
09:20:29.774	+30:28:55.73	2”
09:20:59.852	+30:27:29.23	8”
09:20:50.765	+30:29:22.97	5”
09:20:45.587	+30:28:39.22	8”
09:21:06.817	+30:27:40.20	11”
09:21:05.684	+30:29:02.13	6”

Table 3.3 Point sources excluded from the *Chandra* cluster regions.

spectra using a phenomenological model consisting of a non-X-ray background component (three gaussian lines and a power law to account for instrumental fluorescence lines and charged particles) and an astrophysical component (an absorbed power-law model to account for the unresolved X-ray background). Inclusion of a soft thermal component (from nearby diffuse Galactic emission, for example) did not significantly improve the background fits, so it was not included. The absorption column density was fixed to a value of $N_H = 1.94 \times 10^{20}$ atoms cm^{-2} based on Galactic HI measurements in this direction (Dickey & Lockman 1990) and the photon index of the astrophysical background component was fixed to $\Gamma = 1.4$. Only the normalization of this power-law model was allowed to vary. For the non-X-ray background, the gaussian line centroids and normalizations as well as the power-law index and normalization were allowed to vary freely. There were a total of nine free parameters for the fits to the background spectra. The source spectra included a redshifted thermal plasma model (mekal, in xspec parlance) to account for the cluster emission as well as the full component of background models just described. In all cases best fits were determined using the “c-stat” fit statistic, which is a likelihood figure of merit function appropriate for Poisson-distributed data.

Each pair of matched source and background spectra was fitted jointly with the background spectral components scaled between the source and background based on the ratio of exposure integrated over the extraction regions. In the joint fits the normalizations of the two background power laws plus the non-X-ray background photon index were allowed to vary. The other background model parameter values were held fixed at values determined from the background fits alone.

The best-fit temperature values and 1-σ statistical uncertainties are given in Table 3.6. For the East and Middle clusters, the metal abundance was held fixed to 0.3 times solar. For the Main cluster, because of its higher statistical level, this was allowed to vary yielding a best fit value of 0.27 ± 0.15 times solar (1-σ error). Redshifts were fixed to the values mentioned above. Figure 3.2 shows the best-fit spectra for these three clusters, where the dashed line represents

the contribution from the background.

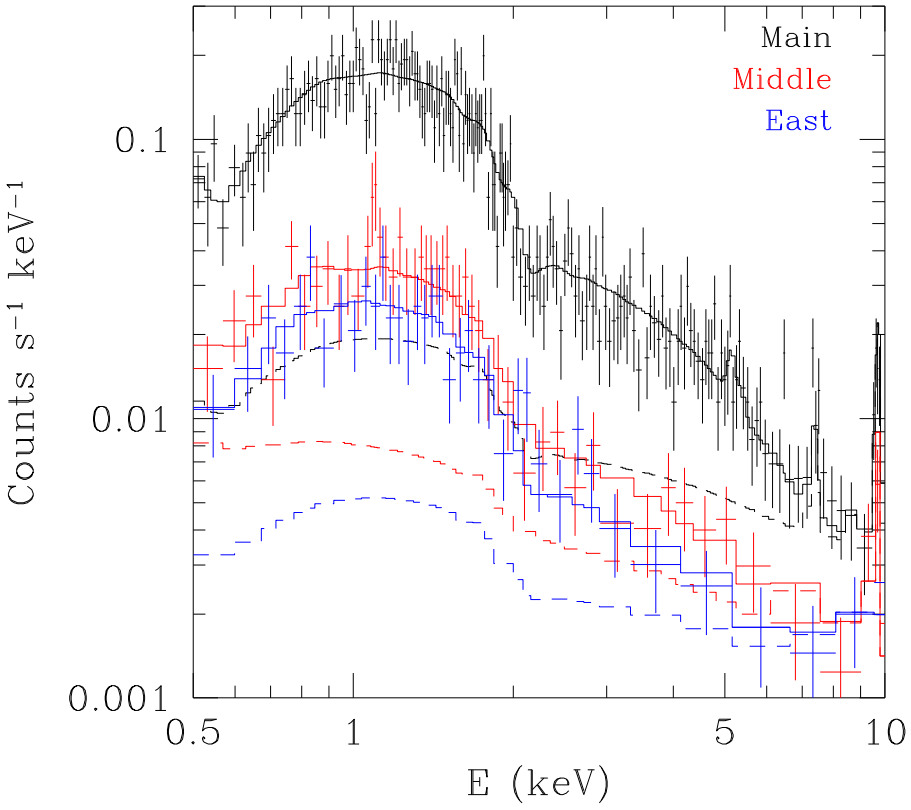

Figure 3.2 From top to bottom, spectra for the Main, Middle, and East clusters from *Chandra*. Solid lines represent the best-fit model, and dashed lines represent the contribution from the background.

Analysis of XMM-Newton Data

The initial data reduction steps for the *XMM-Newton* data were completed using the SAS software tools. The data consists of observations from the three EPIC instruments, MOS1, MOS2, and PN. To model the non-X-ray background from charged particles and instrumental fluorescence lines, we also obtained closed observations (observations with the filter wheel in the closed position) for each of the three EPIC instruments. Thus we were able to use an independent measure of the particle background, differing from our *Chandra* analysis.

Both our cluster data and the closed data were filtered by pattern and energy range. We kept single and double pixel events and events with pulse heights in the range of 300 to 12000 eV for MOS observations. For PN observations, we only kept single pixel events and events with pulse heights between 300 and 15000 eV. We also chose the most conservative screening

criteria (excluding events next to edges of CCDs and next to bad pixels, etc.). Our cluster and closed EPIC data were also filtered for soft solar proton flares.

Figure 3.1 shows the 500-4500 ev band image of the EPIC data after exposure correction and smoothing with a Gaussian of $\sigma = 8''$. Extraction regions for the clusters and point sources were identified along with a background annulus surrounding and away from any of the cluster regions (see Tables 3.4 and 3.5). Spectra were created of the cluster regions and background annulus for both the closed and cluster data, as were spectral response and effective area files. Resolved point sources were excluded from both the source and background regions, and cluster emission was also excluded from the background region.

XMM-Newton	region
Main Cluster	09:20:24.439 +30:30:21.12 2.5'
Middle Cluster	09:20:52.433 +30:28:12.74 1.4'
East Cluster	09:21:09.912 +30:27:58.31 1.1'
Subcluster	09:20:10.046 +30:29:57.17 1'
West	09:19:34.752 +30:32:00.88 1'
Background Annulus	09:20:12.521 +30:29:10.37 10.7' – 13.7' (minus East)

Table 3.4 *XMM-Newton* cluster and background annulus extraction regions. Point sources excluded from the cluster regions are given in Table 3.5.

R.A.	Decl.	Radius
09:20:33.209	+30:28:58.48	17"
09:20:24.600	+30:33:19.12	24"
09:20:21.809	+30:30:35.14	16"
09:20:34.805	+30:29:47.02	12"
09:20:25.531	+30:33:39.11	12"
09:20:45.588	+30:28:39.22	12"
09:21:06.816	+30:27:40.20	11"

Table 3.5 Point sources excluded from the *XMM-Newton* cluster regions.

Xspec was used to fit the spectra of the background annuli in the closed and cluster data using a similar phenomenological model as described for the *Chandra* analysis. The closed data background annulus was fit with several gaussians and three power laws to model the non-X-ray background. This best-fit model was used as a starting model to fit the spectrum of the cluster data background annulus, adding an absorbed power-law to model the unresolved X-ray background and an absorbed soft thermal (mekal) component to model the soft diffuse Galactic emission. The absorption column density and photon index of the astrophysical background model were fixed as mentioned above for the *Chandra* analysis, and the thermal component

was given a fixed plasma temperature of 0.2 keV and a solar metal abundance. We linked the power-law norms of the particle background by the ratio of the power-law norms in the closed background data. This kept the slope and shape of the continuum fixed, but allowed the overall normalization to vary. The spectrum of the cluster data background annulus was fit by allowing the normalizations of the astrophysical background power-law and thermal component to vary as well as the normalization of the non-X-ray particle background.

A best-fit joint model was created to fit the background annulus spectra for the three instruments simultaneously. The parameters of the astrophysical background model were kept in common between the instruments, but the parameters of the particle background differed. A second thermal component was added to the astrophysical background model to better fit the spectra at energies below the aluminum fluorescence line. The normalizations, temperatures, and abundances of the two thermal components were allowed to vary as well as the unresolved X-ray background power law.

The source regions were fit drawing on the closed observations to fit the non-X-ray background and the annulus spectra to fit the astrophysical background. The spectra of the cluster regions in the closed observations were fit using the closed background annulus best-fit model as a starting point. The spectra of the source regions in our data were fit using models starting where the particle background normalization and the normalization of the strongest fluorescence line of each cluster region were set equal to those from the corresponding closed cluster region, scaled by the ratio of the normalizations between the observed and closed background annulus. The normalizations of the weaker fluorescence lines were set equal to the normalization of the strongest line scaled by the ratio of the weak-line norm to the strong-line norm in the corresponding closed cluster region. The astrophysical background model was taken from the best joint-fit model for the background annulus, where the normalizations of the background spectral components were scaled by the ratio of the exposure integrated over the source and background regions. The source spectra were modeled with a redshifted mekal thermal plasma model, with the abundance equal to 0.3 times solar and the temperature and normalization allowed to be free parameters.

We fit the spectra of the source regions using these starting models by first fitting the normalization of the particle background using only events greater than 10 keV, with the cluster model zeroed out. With this normalization frozen, we fit the temperature and norm of the cluster model using only events below 10 keV. The particle background norm was then refit using events larger than 10 keV and this frozen cluster model.

Having fit for the particle background of each source region for each instrument, the best-fit

source models for the three instruments were combined to allow for a joint fit. Again for the joint fit, the astrophysical background model was kept the same for each instrument except that the normalizations differed due to different exposure scalings. This fit was done using the best-fit particle background normalizations described above and those differing by $\pm$ 1-σ for each instrument. In this way, we were able to model the systematic uncertainties arising from the particle background subtraction.

The 1-σ errors on the cluster temperature were obtained using a delta fit statistic of 1.0 for the one interesting parameter. The resulting best-fit temperatures and error bars are given in Table 3.6. We find good agreement between the *Chandra* and *XMM-Newton* best-fit temperatures given the statistical and systematic uncertainties. The *XMM-Newton* spectra for the four main clusters and the best joint-fit models are shown in Figures 3.3 and 3.4.

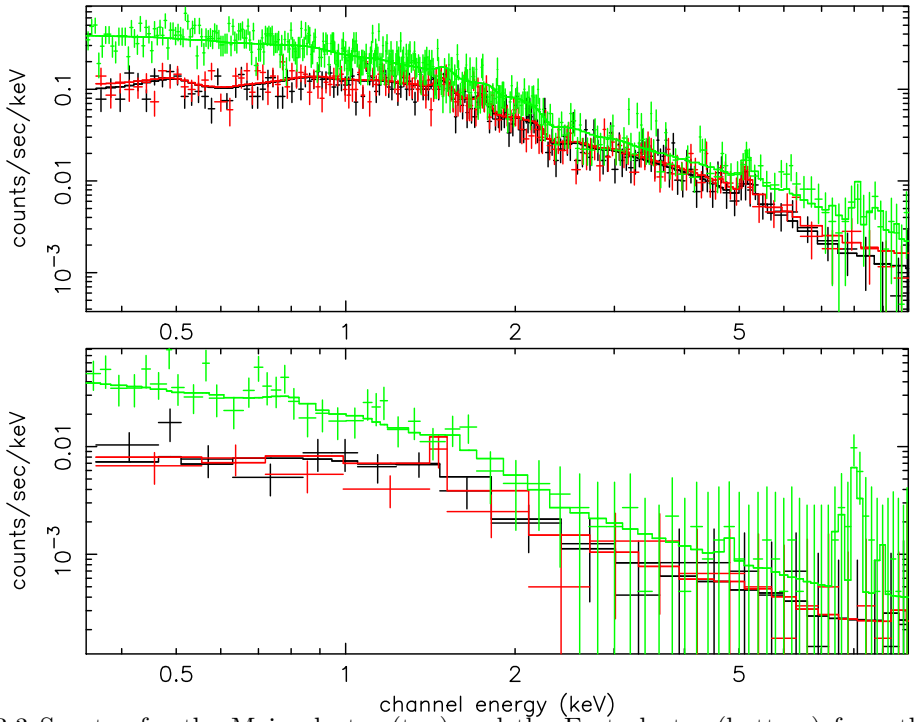

Figure 3.3 Spectra for the Main cluster (top) and the East cluster (bottom) from the three *XMM-Newton* instruments. The Main cluster has the highest, and the East cluster the lowest, signal-to-noise of the four clusters in the pointing. Solid lines represent the best-fit model, and black, red, and green colors correspond to MOS1, MOS2, and PN instruments respectively.

3.4.2 X-ray Surface Brightness Profiles

A surface brightness profile was created by first determining the surface brightness peak of each cluster. This was done with exposure-corrected images in the 500-2000 eV band for each

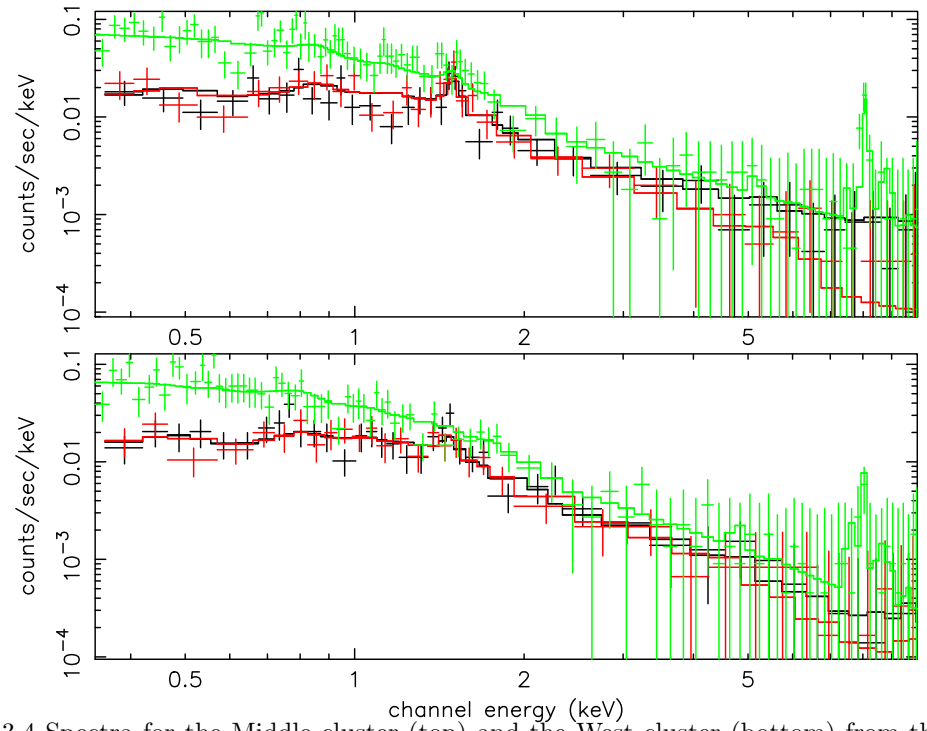

Figure 3.4 Spectra for the Middle cluster (top) and the West cluster (bottom) from the three *XMM-Newton* instruments. Solid lines represent the best-fit model, and black, red, and green colors correspond to MOS1, MOS2, and PN instruments respectively.

instrument smoothed with a Gaussian of $\sigma = 8''$. The vignetting function for the exposure maps was calculated at the monochromatic X-ray energy of 1.25 keV for *XMM-Newton* and 1 keV for *Chandra*.

The unsmoothed images and exposure maps from the three EPIC instruments and *Chandra* were used to generate surface brightness profiles. Images and exposure maps from the separate EPIC focal plane detectors were summed to create a joint *XMM* image and corresponding exposure map. Exposure maps in all cases were made including the effective area, for proper weighting of the *XMM* detectors and for ease of comparing the *XMM* and *Chandra* profiles.

We chose 40 radial bins of $8''$ each, centered around the surface brightness peak of each cluster to find profiles that extend out to 5.3'. In each radial bin, we summed the counts from the *Chandra*/joint *XMM* image and divided this sum by the total exposure in that bin from the corresponding exposure map. We calculated the error on the surface brightness in each radial bin by using the small count statistic $(1+\sqrt{\text{counts}+0.75})/\text{exposure}$ (Gehrels 1986), where units of exposure are given in sec cm^2 arcmin^2.

Using the radial bins farthest from the surface brightness peaks, we inferred the surface brightness due to the background. We then fit the surface brightness profiles to equation 3.3

Cluster	*XMM* counts	*XMM* kT (keV)	*Chandra* counts	*Chandra* kT (keV)
East Cluster	505	$3.6^{+0.6+0.6}_{-0.5-0.7}$	300	$4.7^{+1.4}_{-1.0}$
Middle Cluster	1135	$3.7^{+0.4+0.6}_{-0.3-0.4}$	380	$5.0^{+1.6}_{-1.1}$
Main Cluster	8812	$6.3^{+0.3+0.4}_{-0.3-0.3}$	2400	$7.3^{+1.1}_{-0.7}$
West Cluster	1163	$4.0^{+0.4+0.5}_{-0.3-0.5}$	0	...

Table 3.6 Integrated temperature estimates for the four clusters from fits to the *XMM-Newton* and *Chandra* spectra. Note the first *XMM-Newton* error given is statistical and the second is systematic due to background subtraction.

by fixing the background and allowing β, r_c, and the overall normalization to vary as free parameters. The profiles and best-fit models are displayed in Figures 3.5 and 3.6. Table 3.7 gives the β and r_c best-fit values for each cluster along with their 1-σ statistical error bars. There is good agreement between the *Chandra* and *XMM-Newton* best-fit β and r_c values given the statistical uncertainties.

Cluster	*XMM* β	*XMM* r_c (arcmin)	*Chandra* β	*Chandra* r_c (arcmin)
East Cluster	$0.81^{+0.29}_{-0.15}$	$1.19^{+0.44}_{-0.24}$	$0.68^{+0.39}_{-0.13}$	$0.94^{+0.59}_{-0.29}$
Middle Cluster	$0.51^{+0.05}_{-0.04}$	$0.71^{+0.20}_{-0.15}$	$0.56^{+0.13}_{-0.09}$	$0.99^{+0.49}_{-0.34}$
Main Cluster	$0.87^{+0.06}_{-0.05}$	$1.82^{+0.15}_{-0.15}$	$0.88^{+0.12}_{-0.10}$	$2.01^{+0.34}_{-0.24}$
West Cluster	$0.60^{+0.03}_{-0.02}$	$0.31^{+0.03}_{-0.03}$	...	...

Table 3.7 Best-fit β and r_c values for the four clusters from fitting *XMM-Newton* and *Chandra* surface brightness profiles assuming a β-model for the gas density.

3.5 Mass Estimates

3.5.1 X-ray Masses

To determine each cluster's X-ray derived mass, we use equations 3.1, 3.2, and 3.5 and our best-fit β and r_c values to predict the cluster temperature profile for given values of the central density and scale radius in the NFW profile. The solution of the temperature profile requires a boundary condition. We assume the cluster temperature to be 1.25 keV at 3.5 Mpc for each cluster but allow this outer temperature and radius to vary generously over the range of 0.5 to 2 keV and 2 to 5 Mpc and fold this uncertainty into our error bars. We find that this variation in our boundary conditions contributes a negligible amount (less than 4%) to our error estimates.

To compare each cluster's X-ray and weak-lensing-derived masses in an mutually consistent manner, we must assume the same matter density profile for each method. Since neither the X-ray nor the weak-lensing data is deep enough to well constrain both ρ_0 and r_s in the

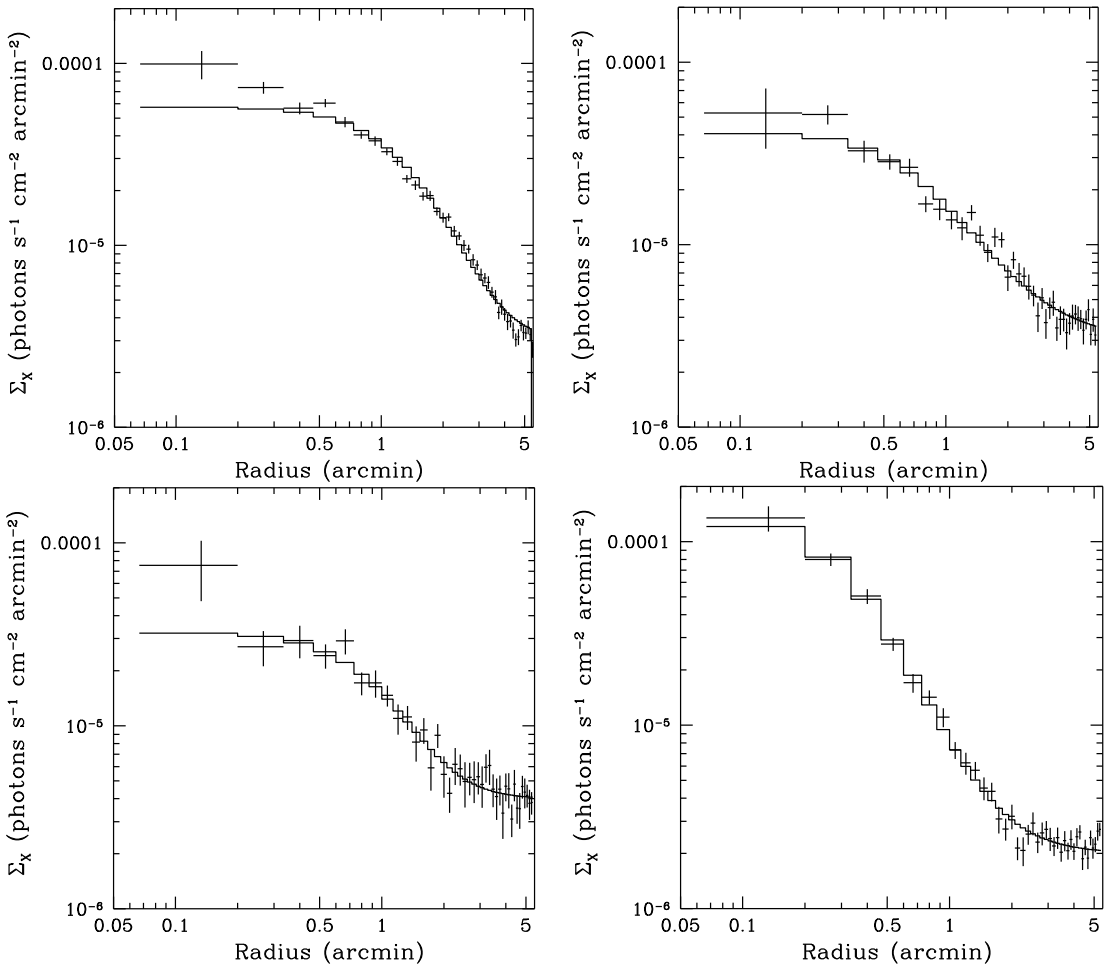

Figure 3.5 *XMM-Newton* surface brightness profiles for the Main (top, left), Middle (top, right), East (bottom, left), and West (bottom, right) clusters and best-fit models. The energy band used is 0.5-2 keV.

NFW profile, we choose to estimate each cluster's concentration parameter, $c \propto 1/r_s$, using results from hydrodynamic simulations and an X-ray estimate of each cluster's mass assuming isothermality. This mass estimate is accurate enough to give a reasonable estimate of the concentration parameter since the concentration is a slowly varying function of cluster mass. The concentration parameter is here defined as r_{500}/r_s, where r_{500} is the radius within which the cluster mean density is 500 times the critical density. We again use the isothermal case to estimate r_{500}, which yields an estimate of r_s. Since we are primarily interested in the comparison between X-ray-derived and weak-lensing-derived masses, the accuracy of the scale radius is less important than the fact that we used the same scale radius in deriving the masses using both methods. A change in the scale radius may introduce a systematic shift in the masses but will

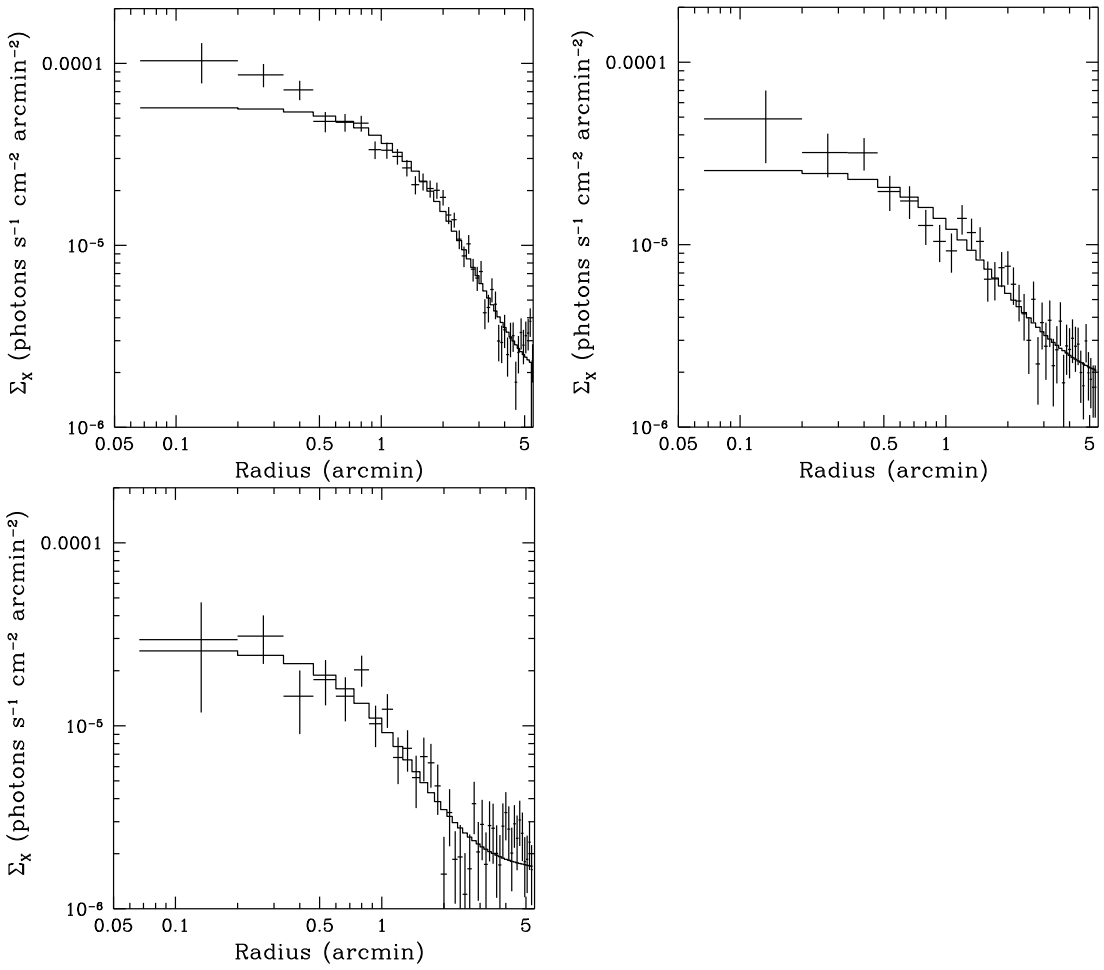

Figure 3.6 *Chandra* surface brightness profiles for the Main (top, left), Middle (top, right), and East (bottom, left) clusters and best-fit models. The energy band used is 0.5-2 keV.

not alter significantly their ratio.

Masses Assuming an Isothermal-β Model

We determine X-ray isothermal β-model mass estimates for these clusters as an intermediate step to estimate the NFW scale radius for each cluster. If we assume that each cluster is isothermal with a gas density given by equation 3.2, then equation 3.1 can be rewritten to give

$$\begin{aligned} M(r) &= 3\beta \frac{kTr}{G\mu m_p} \left[\frac{\left(r/r_c\right)^2}{1+\left(r/r_c\right)^2} \right] \\ &= 1.13 \times 10^{15} \beta \frac{T_X}{10 \text{ keV}} \frac{r}{\text{Mpc}} \left[\frac{\left(r/r_c\right)^2}{1+\left(r/r_c\right)^2} \right] M_\odot, \end{aligned} \tag{3.6}$$

where we set $\mu = 0.59$ for the cluster gas (Evrard et al. 1996). Using the best-fit β, r_c, and T_X for each cluster from *Chandra* and *XMM-Newton* observations, we calculate M_{500} for each cluster, which is the mass within r_{500}. The best-fit r_{500} and M_{500} for each cluster from each X-ray satellite are listed in Table 3.8. This table is without error bars since we only use these values to estimate a reasonable r_s for each cluster.

We use the above *XMM* r_{500} and M_{500} values and predictions for the concentration as a function of mass and redshift derived from hydrodynamic cluster simulations (Dolag et al. 2004) to obtain an estimate of r_s. The $c(M, z)$ relation used here is from the Dolag et al. (2004) ΛCDM cosmological simulation, and we converted our masses and radii to the definitions used in that work to determine r_s. This concentration relation has a reasonable agreement with *Chandra* observations of nearby clusters (Vikhlinin et al. 2006). We choose to use *XMM* β-model masses since we have *XMM* observations for all four clusters. Table 3.9 lists the best estimates of r_s. We hold this scale radius fixed and keep it in common when deriving masses from weak-lensing and X-ray methods and focus on the relative difference in mass estimates using these two methods.

Cluster	*XMM* r_{500} (Mpc)	*XMM* M_{500} ($10^{14} M_{\odot}$)	*Chandra* r_{500} (Mpc)	*Chandra* M_{500} ($10^{14} M_{\odot}$)
East Cluster	0.91	2.5	0.99	3.2
Middle Cluster	0.84	1.7	1.01	3.0
Main Cluster	1.38	7.6	1.48	9.5
West Cluster	0.89	2.4	...	...

Table 3.8 Best-fit *Chandra* and *XMM-Newton* mass estimates within r_{500} assuming an isothermal β-model.

Masses Assuming an NFW Profile

Given an estimate of r_s, β, and r_c for each cluster, we vary ρ_0 and calculate the emission-weighted, projected, average temperature within an aperture (as discussed in §3.4). The apertures for each cluster and instrument are given in Tables 3.2 and 3.4. We match the predicted temperatures to our measured temperatures in Table 3.6 to find the best-fit central densities. The 1-σ errors on ρ_0 are calculated by varying the measured T_X, β, and r_c parameters within their 1-σ error bars and treating β and r_c as correlated variables. The variation in the boundary condition introduces a negligible error on ρ_0 as mentioned above. Best-fit ρ_0 measurements and 1-σ errors for *Chandra* and *XMM* observations are given in Table 3.9. There is good agreement between the two instruments, and we calculate a weighted average to give a combined X-ray ρ_0

for each cluster, which we also list in Table 3.9. Given ρ_0 and r_s, X-ray masses are calculated using equation 3.5 and listed in Table 3.10. These masses are calculated using the combined X-ray ρ_0 for all the clusters except the West cluster, for which only the *XMM* ρ_0 is available.

3.5.2 Weak-Lensing Masses

The weak lensing mass estimates are based on the full DLS exposure time of 18 ks in R and 12 ks in BVz', rather than the partially complete imaging used for cluster discovery in Wittman et al. (2006). Otherwise, image processing was as described in detail in that paper. The R data were taken in good seeing conditions (FWHM $< 0.9''$) and are used to measure the galaxy shapes. The A781 complex spans two contiguous DLS "subfields" or pointing centers. The FWHM of the final R images, after circularizing the PSF and co-adding 20 exposures, is $0.78''$ and $0.74''$ for the two subfields involved. The BVz' data are used only to provide color information for photometric redshifts.

We extracted shear catalogs using a partial implementation of Bernstein & Jarvis (2002). This implementation appeared as the "VM" method in Heymans et al. (2006), which compared different weak-lensing methods on a set of simulated sheared images. After correcting for stellar contamination which was present in that dataset but not here, the VM method yielded 89% of the true shear in those images. In this work, we divide the VM results by 0.89 to more closely approximate the true shear. However, we recognize that this correction factor is likely to be data-dependent, and we therefore assign a systematic error of 10% to the shear calibration.

We derived photometric redshifts using BPZ (Benítez 2000) with the HDF prior. We optimized the templates using a subset of the SHELS (Geller et al. 2005) spectroscopic sample and the procedure of Ilbert et al. (2006). Complete details are discussed elsewhere (Margoniner et al., in preparation). To assess the accuracy of these photometric redshifts, we turn to an independent spectroscopic sample, consisting of all redshifts in DLS field F2 in the literature, as tabulated by the NASA/IPAC Extragalactic Database. We find 328 galaxies with spectroscopic redshifts that match our cleaned photometry (unsaturated, not near bright stars, etc), spanning the redshift range 0.02—0.70. The resulting rms photometric redshift error per galaxy is $0.047(1+z)$, with a bias of $-0.017(1+z)$, and no catastrophic outliers.

Because shear is nonlocal and mass maps tend to be highly smoothed, the presence of one clump may affect the apparent mass density of another clump. This is true of the Wittman et al. (2006) maps, and we eliminate that effect here by simultaneously fitting axisymmetric

NFW profiles to the four X-ray positions. The model fitting takes into account the full three-dimensional position (RA, DEC, z) of each source galaxy. The per-galaxy imprecision in z is not important because the lensing kernel is very broad, and because each galaxy is a very noisy estimator of the shear: a 0.1 shift in source redshift changes the modeled shear by much less than the per-galaxy shear error. For each NFW model, RA and DEC were fixed by the X-ray position, z was fixed by the spectroscopy, and r_s was fixed to the value used for the X-ray fitting. Thus only one parameter, ρ_0, was fit for each model. Wright & Brainerd (2000) give expressions for shear induced by an NFW profile.

Of the ∼350,000 galaxies in the $2^\circ \times 2^\circ$ DLS field containing A781, we limited the fit to galaxies within $15'$ of a clump center, for computational efficiency and because more distant galaxies may be influenced more by other clusters than by those in the A781 complex. We also cut on photometric redshift, because cluster members scattering to higher redshift would reduce the estimated shear (slightly, because of their low inferred distance ratio), while cluster members scattering to lower redshift would have no effect. We did fits with cuts at $z_{\rm phot} > 0.35$ (just behind the richer, lower-redshift clumps) and $z_{\rm phot} > 0.62$ (3σ beyond the higher-redshift clumps), and found a difference of $\leq 0.2\sigma$ in the fitted parameters. The lenient (strict) cut yielded 30137 (22173) galaxies, or 23 (17) arcmin^{-2} over 1320 arcmin^2, although ∼10% of this area was masked due to bright stars. We adopt the strict cut to avoid any question of contamination. The resulting source catalogs show no increased density near the clump centers.

Because shear from an NFW profile is linear in ρ_0, we used singular value decomposition (SVD) as described in Press et al. (1992)). This solves the general linear least squares problem in one pass, with no iteration required. The galaxies were given equal weights in the fit, because the VM shear method does not assign weights to galaxies. However, the importance of a galaxy in determining the fit still depends on its position and redshift, through the model's dependence on position and redshift. We then corrected for the fact that the observable in weak lensing is not the shear γ, but the reduced shear $\gamma/(1-\kappa)$ (where κ is the convergence) as follows. We computed the convergence of the best-fit model at the location of each source galaxy, constructed a reduced-shear model, redid the linear fit, and iterated. In the first iteration, this resulted in a ∼5% correction to the fit parameters. In the second iteration, the correction was only ∼0.2%, much smaller than the fitted parameter statistical uncertainties, and therefore the reduced-shear fit was deemed to have converged.

The fitted ρ_0's and their uncertainties are listed in Table 3.9. The uncertainties output by the SVD routine were confirmed by 1000 bootstrap resampling realizations. Although the fit is not χ^2-driven, we can define a $\Delta\chi^2$ statistic to see how much of the variance in the data

is explained by the model. There are 44326 degrees of freedom because each galaxy has two shear components. For each component of shear, we compute the rms without any fit and define that as the uncertainty associated with each galaxy. This results in an initial χ^2 of 44326, which is decreased by 40.4 when the four-parameter model is subtracted off. The chance of this happening randomly is $< 10^{-7}$ for Gaussian distributions. The remaining variance is due mostly to the intrinsically random distribution of galaxy shapes (shape noise) and shape measurement errors, although a small amount may be attributed to additional structure in the field as indicated by the following mass maps.

We show the fit visually in Figure 3.7. The top panel shows a mass map made using the method described in Wittman et al. (2006) (originally from Fischer & Tyson (1997)), the middle panel shows a similar map made from the model shears, and the bottom panel shows a map made from the residual shear after subtracting off the fit. The Main, Middle, and East clumps have been mostly subtracted, but the West clump has not been well modeled. There is also an unmodeled mass clump just northwest of the East clump (RA $\approx$ 9:21, Dec $\approx$ 30:33), which appears to have some associated galaxies. We caution that the mass map is a sanity check rather than a quantitative indicator of goodness-of-fit, because it does not fold in source redshift information.

In Table 3.9, weak-lensing errors are of two types, the first is statistical and the second is systematic. For the statistical errors, we performed bootstrap resampling to estimate the covariance of the cluster mass estimates. The masses of neighboring clusters (in projection) are anticorrelated, because the observed shear in a region must include the sum of the model shears from the neighbors. The errors given here for each cluster are after marginalizing over the allowed values for the other clusters. Therefore, the error on the total mass of all the clusters would be smaller than the quadrature sum of the errors given here. Also, the covariance will affect the comparison of the lensing ρ_0 for one of the four clusters to that for any of the others.

Systematic errors include shear calibration, source redshift calibration, mass sheet degeneracy, and residual cluster member contamination. We assign a shear calibration systematic uncertainty of 10% as explained above. We explored the effects of source redshift errors by fitting to different source redshift ranges. We find that only if we include photometric redshifts beyond 1.4, where the 4000 Å break redshifts out of the z' filter, do the results change by as much as 10%. Even in that case, the results appear to change randomly rather than systematically, with some clumps increasing in fitted mass and others decreasing. Given these results, and the small bias in photometric redshifts when compared to the spectroscopic sample from the literature, a systematic error of 5% in mass due to redshift calibration errors is very

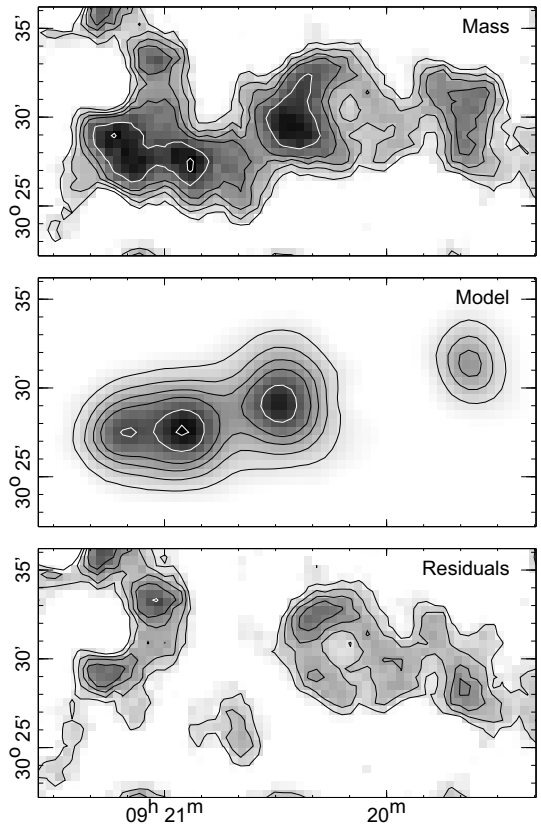

Figure 3.7 Lensing data, model, and residuals. Top: mass map of the area. Grayscale and contours are in arbitrary units, but the same units are used for all the panels. Middle: best-fit lensing mass model. Bottom: mass map made from residual shear after subtracting off the quadruple NFW profile fit shown in the middle panel.

conservative.

We estimate residual cluster member contamination by examining the source galaxy areal density around the richest (Main) clump. There is an excess in the central $2'$ radius. Comparing the redshift distribution in that area to a control annulus, we find 58 excess galaxies at redshifts 0.35–0.42, presumably cluster members with $> 1\sigma$ photometric redshift errors. In the fit, all galaxies were weighted equally, so their relative importance is determined by their proximity (in three dimensions) to where the model reduced shear is large. These galaxies are near the projected center of the lens, but at low inferred distance ratio. We compute their effective weight as the square of the model reduced shear, and compare their total weight to the rest of the galaxies within $5'$ of the Main clump. The summed weight of the interloping galaxies is only 0.010 times that of the valid source galaxies, which presumably resulted in a 1% underestimate of the mass, much smaller than the other systematics.

The last systematic involves mass sheet degeneracy and projection of unrelated structures

near the line of sight. *If* our assumption of an NFW profile is correct, then mass sheet degeneracy is not an issue, because we are fitting the profile rather than empirically determining departures from a baseline. Measuring shear to as large a radius as possible would help check the profile assumption, just as it would help reduce mass sheet degeneracy. However, going to large radii increases the chance of including some unrelated structure projected near the line of sight. Metzler et al. (2001) (hereafter M01) characterized this by measuring lensing masses of clusters in large-scale numerical simulations as a function of data set radius. The truncation radius used in the fitting here, $30'$, corresponds to a transverse separation of about 5 Mpc, for which M01 find a scatter of about 7%. (Note that M01's systematic offset in the population is not relevant here because profile fitting is less biased than their aperture densitometry.) Scatter in the population becomes a systematic when considering a single cluster. However, by simultaneously fitting multiple clumps, this systematic is probably already greatly reduced. We empirically test this effect by varying the truncation radius and find that the results can change by up to 5%. We therefore assign a systematic of 5% due to this effect. The larger systematic is likely to be in the profile assumption. This systematic is likely to be on the same order as the mass sheet degeneracy systematic incurred if the profile assumption were dropped, which is quoted as 20% by Bradač et al. (2004).

In summary, the systematics include 20% for the profile assumption and/or mass sheet degeneracy, 10% for shear calibration, 5% for projections, and 5% for photometric redshift errors. We include only the latter three systematic errors in Table 3.9, where we assume an NFW profile accurately describes the matter density. This allows us to compare the X-ray and weak-lensing ρ_0 values. In table 3.10, we present a summary of the r_{500} and M_{500} values, where the the weak-lensing statistical and systematic error bars on ρ_0 are added in quadrature. It should be kept in mind that the absolute masses of the clusters depend on the profile assumption.

Cluster	Estimated r_s (Mpc)	*XMM* ρ_0 (10^{-26} g/cm^3)	*Chandra* ρ_0 (10^{-26} g/cm^3)	Combined X-ray ρ_0 (10^{-26} g/cm^3)	DLS ρ_0 (10^{-26} g/cm^3)
East	0.37	$3.9^{+1.0}_{-1.0}$	$5.2^{+1.6}_{-1.2}$	4.4 ± 0.8	$4.4 \pm 1.3 \pm 0.6$
Middle	0.31	$5.2^{+1.1}_{-0.7}$	$7.3^{+2.3}_{-1.7}$	5.8 ± 0.9	$6.8 \pm 1.5 \pm 0.8$
Main	0.60	$3.1^{+0.3}_{-0.2}$	$3.5^{+0.5}_{-0.4}$	3.2 ± 0.2	$2.2 \pm 0.4 \pm 0.3$
West	0.33	$6.4^{+1.0}_{-0.9}$	...	6.4 ± 1.0	$4.0 \pm 1.7 \pm 0.4$

Table 3.9 Estimated scale radii of NFW mass profiles and best-fit NFW central densities from *Chandra*, *XMM-Newton*, and DLS.

Cluster	X-ray r_{500} (Mpc)	X-ray M_{500} ($10^{14} M_{\odot}$)	Weak-lensing r_{500} (Mpc)	Weak-lensing M_{500} ($10^{14} M_{\odot}$)
East Cluster	$0.74^{+0.06}_{-0.07}$	$1.8^{+0.5}_{-0.5}$	$0.73^{+0.11}_{-0.13}$	$1.8^{+0.9}_{-0.8}$
Middle Cluster	$0.76^{+0.06}_{-0.06}$	$1.7^{+0.4}_{-0.4}$	$0.82^{+0.10}_{-0.12}$	$2.0^{+1.0}_{-0.7}$
Main Cluster	$1.09^{+0.04}_{-0.04}$	$5.2^{+0.3}_{-0.7}$	$0.89^{+0.10}_{-0.12}$	$2.7^{+1.0}_{-0.9}$
West Cluster	$0.79^{+0.06}_{-0.06}$	$2.2^{+0.5}_{-0.4}$	$0.60^{+0.15}_{-0.14}$	$1.1^{+0.8}_{-0.7}$

Table 3.10 X-ray and shear masses within r_{500} for the four clusters assuming an NFW matter density profile.

3.6 Discussion

Comparison of the X-ray and weak-lensing ρ_0 values indicates that these values are in agreement for the East, Middle, and West clusters. This agreement suggests that line-of-sight mass contributions have not significantly biased the weak-lensing measurements.

For the Main cluster, the X-ray-derived ρ_0 is higher than that from weak-lensing by about 2σ. The X-ray images of the Main cluster suggest it may be undergoing a merger with a subcluster (see Figure 3.1), and thus may be out of hydrostatic equilibrium. From the literature it is not obvious whether cluster mergers are expected to bias X-ray mass estimates high or low. Weak-lensing observations of 22 X-ray bright clusters at $0.05 < z < 0.31$ found X-ray temperatures higher by $40 - 75\%$ than those inferred from weak-lensing, for clusters with $T_X > 8$ keV (Cypriano et al. 2004). The largest discrepancy in this sample was for the two clusters with the highest X-ray temperatures ($T_X \sim 13$ keV), which both show signs of being out of dynamical equilibrium. It is a reasonable extrapolation to presume that all the clusters with $T_X > 8$ keV in their sample are unrelaxed, with the temperature of their intracluster medium boosted by shocks due to in-falling groups and mergers with other clusters.

However, recent hydrodynamic simulations indicate that unrelaxed cluster temperatures should be lower than those for relaxed clusters of the same mass (Kravtsov et al. 2006; Nagai et al. 2007). The reasoning for this is that over the course of a merger, the mass of the system increases faster than the conversion of the kinetic energy of the merging systems into thermal energy of the intracluster medium (Kravtsov et al. 2006). It has also been suggested from hydrodynamic simulations of merging clusters that X-ray mass estimates based on hydrostatic equilibrium can be biased high close to core-crossing, where a temperature boost occurs due to shocks, but can be biased low just before and after this temperature spike (Poole et al. 2006; Puchwein & Bartelmann 2007). This latter scenario is possibly supported by recent X-ray and weak-lensing observations of 10 X-ray luminous clusters at $z \sim 0.2$ (Zhang et al. 2007; Bardeau

et al. 2007). The X-ray observations of this sample were carried out with *XMM-Newton*, and the weak-lensing is from ground-based imaging with the CFH12k camera on CFHT. These authors report that four out of these ten clusters have consistent X-ray and weak-lensing mass estimates. Of the six clusters that show a mass discrepancy, half have higher and half have lower X-ray as compared to weak-lensing masses.

It is possible that the Main cluster in the A781 cluster complex is close to core-crossing as our X-ray mass estimate is biased high. It is also possible that a selection effect is occurring in the sample of Cypriano et al. (2004) where the clusters with $T_X > 8$ keV are in a state of high temperature boosting and thus close to core-crossing. Deeper X-ray observations of this A781 cluster and further comparisons of weak-lensing and X-ray mass estimates of known merging clusters will help to clarify the biases expected from dynamically unrelaxed systems.

The West cluster did not appear in our original shear maps, and we confirm here that it is a low significance weak-lensing detection (1-2σ). It was detected in the X-ray by chance as it fell within the same *XMM-Newton* pointing as the other three clusters. However, weak-lensing and X-ray data yield consistent mass estimates. We measure a very small core radius for this cluster ($r_c = 0.31'$), consistent with most of the emission coming from a compact core. Northwest of the East cluster, we also find an enhancement in both the galaxy distribution and lensing signal, and we find some indication of X-ray emission from that region. Further X-ray observations would allow us to study these lower mass systems in more detail.

Based on the limited information available, the velocity dispersion values appear broadly consistent with the East, Middle, and Main clusters having nearly equal masses (Geller et al. 2005). This agrees with the similarity in weak-lensing masses we present here (see Table 3.10). A detailed comparison of the cluster masses derived above with the velocity distributions is beyond the scope of this work. Study of the velocity distribution of the potentially merging component (Main cluster) could shed light on the epoch and geometry of the merger (see Gómez et al. (2000)).

3.7 Conclusion

Many cluster surveys will take place over the next few years at several different wavebands. Already considerable samples of X-ray and optically selected clusters have been compiled. In addition, sizeable microwave and shear-selected samples are close at hand. These surveys can probe with precision the growth of structure over cosmic time, and thereby open a new window on cosmology. However, the two main hurdles to overcome are relating cluster observables to

mass and characterizing the sample selection. By comparing weak-lensing and X-ray observations and mass estimates for clusters in the DLS shear-selected sample we hope to understand the systematic biases in both mass estimation methods and modes of cluster selection.

An analysis of the top shear-ranked mass distribution in the DLS sample reveals a complex of four clusters, the largest of which can be identified as A781. The four clusters are at distinctly different redshifts, as determined by optical spectroscopy, and the X-ray images suggest three are dynamically relaxed while the largest cluster appears to be merging with a small subcluster. Masses from both X-ray and weak-lensing observations were determined assuming an NFW profile for the matter density. Since neither sets of observations were deep enough to well constrain both the central density and scale radius of each cluster NFW profile, we estimated the scale radii using X-ray-derived isothermal β-model mass estimates and a relation describing concentration as a function of mass and redshift derived from cosmological hydrodynamic simulations. For each cluster profile, the same scale radius was used to determine the best-fit X-ray and weak-lensing central densities. We focus on the difference in central densities derived with each method as the central density scales linearly with mass.

We find that three out of the four clusters show agreement between their X-ray and weak-lensing derived central densities. The fourth and largest cluster has an X-ray derived central density higher than that derived from weak-lensing by about 2σ. This discrepancy is most likely due to the cluster's disrupted dynamical state. Recent weak-lensing observations of X-ray selected clusters and hydrodynamic simulations leave some ambiguity about whether dynamical disruption via cluster mergers biases X-ray mass estimates high or low. The direction of the bias may be related to the stage of the merger, e.g., whether it is close to core-crossing or more advanced. Deeper X-ray observations of this cluster to better resolve the merger and further comparisons between weak-lensing and X-ray-derived masses of known merging clusters will shed greater light on this issue.

Initial steps are being made by many groups to overcome the above mentioned hurdles regarding the use of clusters as precision tracers of structure growth. Our collaboration, for example, has *Chandra* and *XMM-Newton* data on a larger sample of DLS shear-selected clusters that we will be reporting on in future publications. Hopefully all these efforts will open a new window through which we can understand our universe.

Bibliography

Bardeau, S., Soucail, G., Kneib, J. P., Czoske, O., Ebeling, H., Hudelot, P., Smail, I., & Smith,

G. P. 2007, A&A, 470, 449

Benítez, N. 2000, ApJ, 536, 571

Bernstein, G. M., & Jarvis, M. 2002, AJ, 123, 583

Bradač, M., Lombardi, M., & Schneider, P. 2004, A&A, 424, 13

Carlstrom, J. E., Holder, G. P., & Reese, E. D. 2002, ARA&A, 40, 643

Cavaliere, A., & Fusco-Femiano, R. 1978, A&A, 70, 677

Cypriano, E. S., Sodré, L. J., Kneib, J.-P., & Campusano, L. E. 2004, ApJ, 613, 95

Dahle, H., Kaiser, N., Irgens, R. J., Lilje, P. B., & Maddox, S. J. 2002, ApJS, 139, 313

de Putter, R., & White, M. 2005, New Astronomy, 10, 676

Dickey, J. M., & Lockman, F. J. 1990, ARA&A, 28, 215

Dolag, K., Bartelmann, M., Perrotta, F., Baccigalupi, C., Moscardini, L., Meneghetti, M., & Tormen, G. 2004, A&A, 416, 853

Erben, T., van Waerbeke, L., Mellier, Y., Schneider, P., Cuillandre, J.-C., Castander, F. J., & Dantel-Fort, M. 2000, A&A, 355, 23

Evrard, A. E., Metzler, C. A., & Navarro, J. F. 1996, ApJ, 469, 494

Fischer, P., & Tyson, J. A. 1997, AJ, 114, 14

Gavazzi, R., & Soucail, G. 2007, A&A, 462, 459

Gehrels, N. 1986, ApJ, 303, 336

Geller, M. J., Dell'Antonio, I. P., Kurtz, M. J., Ramella, M., Fabricant, D. G., Caldwell, N., Tyson, J. A., & Wittman, D. 2005, ApJ, 635, L125

Gómez, P. L., Hughes, J. P., & Birkinshaw, M. 2000, ApJ, 540, 726

Gray, M. E., Ellis, R. S., Lewis, J. R., McMahon, R. G., & Firth, A. E. 2001, MNRAS, 325, 111

Heymans, C., et al. 2006, MNRAS, 368, 1323

Hughes, J. P., et al. 2004, in "Multiwavelength Cosmology", Astrophysics and Space Science Library, Volume 301, ed. Manolis Plionis, p.255

Ilbert, O., et al. 2006, A&A, 457, 841

Koopmans, L. V. E., et al. 2000, A&A, 361, 815

Kravtsov, A. V., Vikhlinin, A., & Nagai, D. 2006, ApJ, 650, 128

Margoniner, V., & Wittman, D. 2007, ApJ, submitted (arXiv:0707.2403)

Metzler, C. A., White, M., & Loken, C. 2001, ApJ, 547, 560

Metzler, C. A., White, M., Norman, M., & Loken, C. 1999, ApJ, 520, L9

Miralles, J.-M., et al. 2002, A&A, 388, 68

Muller, G. P., Reed, R., Armandroff, T., Boroson, T. A., & Jacoby, G. H. 1998, in Proc. SPIE Vol. 3355, p. 577-585, Optical Astronomical Instrumentation, Sandro D'Odorico; Ed., 577

Nagai, D., Vikhlinin, A., & Kravtsov, A. V. 2007, ApJ, 655, 98

Navarro, J. F., Frenk, C. S., & White, S. D. M. 1996, ApJ, 462, 563

Navarro, J. F., Frenk, C. S., & White, S. D. M. 1997, ApJ, 490, 493

Oke, J. B., Cohen, J. G., Carr, M., Cromer, J., Dingizian, A., Harris, F. H., Labrecque, S., Lucinio, R., Schaal, W., Epps, H., & Miller, J. 1995, PASP, 107, 375

Poole, G. B., Fardal, M. A., Babul, A., McCarthy, I. G., Quinn, T., & Wadsley, J. 2006, MNRAS, 373, 881

Press, W. H., Teukolsky, S. A., Vetterling, W. T., & Flannery, B. P. 1992, Numerical Recipes in C (2nd ed.; Cambridge: Cambridge University Press)

Puchwein, E., & Bartelmann, M. 2007, A&A, 474, 745

Sarazin, C. L. 1986, Reviews of Modern Physics, 58, 1

Schirmer, M., Erben, T., Hetterscheidt, M., & Schneider, P. 2007, A&A, 462, 875

Spergel, D. N., et al. 2003, ApJS, 148, 175

Umetsu, K., & Futamase, T. 2000, ApJ, 539, L5

Vikhlinin, A., Kravtsov, A., Forman, W., Jones, C., Markevitch, M., Murray, S. S., & Van Speybroeck, L. 2006, ApJ, 640, 691

Weinberg, N. N., & Kamionkowski, M. 2002, MNRAS, 337, 1269

White, M., van Waerbeke, L., & Mackey, J. 2002, ApJ, 575, 640

Wittman, D., Dell'Antonio, I. P., Hughes, J. P., Margoniner, V. E., Tyson, J. A., Cohen, J. G., & Norman, D. 2006, ApJ, 643, 128

Wittman, D., Margoniner, V. E., Tyson, J. A., Cohen, J. G., Becker, A. C., & Dell'Antonio, I. P. 2003, ApJ, 597, 218

Wittman, D., Tyson, J. A., Margoniner, V. E., Cohen, J. G., & Dell'Antonio, I. P. 2001, ApJ, 557, L89

Wittman, D. M., et al. 2002, in Survey and Other Telescope Technologies and Discoveries. Edited by Tyson, J. Anthony; Wolff, Sidney. Proceedings of the SPIE, Volume 4836, pp. 73-82 (2002)., 73

Wright, C. O., & Brainerd, T. G. 2000, ApJ, 534, 34

Zhang, Y.-Y., Finoguenov, A., Böhringer, H., Kneib, J.-P., Smith, G. P., Czoske, O., & Soucail, G. 2007, A&A, 467, 437

Chapter 4

Constrained Cluster Parameters from Sunyaev-Zel'dovich Observations

The material in this chapter also appears in print as "Constrained Cluster Parameters from Sunyaev-Zel'dovich Observations", Sehgal et al. 2005, ApJ, 635, 22.

4.1 Introduction

Observations of the Sunyaev-Zel'dovich (SZ) effect (Sunyaev & Zel'dovich 1972) offer the hope of revealing much about the properties of galaxy clusters and the evolution of large-scale structure. Several instruments are being built (ACT, SPT, APEX, Planck) that will make use of the SZ effect to produce deep galaxy cluster surveys, and upgrades to current experiments, such as SuZIE III, will produce deep targeted observations of known galaxy clusters. These surveys, in addition to measuring the number density of clusters, can, in principle, reveal each galaxy cluster's peculiar velocity, gas temperature, and optical depth, if the SZ information is fully exploited. The aim of this paper is to quantify some of the difficulties with determining these individual cluster parameters from future SZ measurements and to discuss what cluster parameters these future surveys can constrain.

The SZ effect is a spectral distortion of the cosmic microwave background caused by an intervening galaxy cluster. The hot gas in the intracluster medium inverse Compton scatters the microwave photons creating this distortion. For reviews of the SZ effect see Rephaeli (1995), Sunyaev & Zel'dovich (1980), Birkinshaw (1999), and Carlstrom et al. (2002). The dependence of this spectral distortion on the gas temperature (T), radial peculiar velocity (v), and optical depth (τ), including relativistic corrections, has been computed in several papers (Challinor & Lasenby 1998; Sazonov & Sunyaev 1998; Itoh et al. 1998; Nozawa et al. 1998; Molnar & Birkinshaw 1999; Dolgov et al. 2001). Since the amplitude of this distortion is also a function of frequency, SZ measurements at three different observing frequencies would ideally be enough to disentangle the three unknowns (T, v, τ) contributing to the SZ signal. Some first attempts to determine cluster temperatures using the relativistic SZ effect were

carried out by Pointecouteau et al. (1998) and Hansen et al. (2002), the former simulating clusters observed with Planck and the latter providing a temperature estimate of Abell 2163 with quite large uncertainties. More recently, Hansen (2004a) has developed code to extract cluster parameters using the SZ effect which results in rather large errors if given prospective data from upcoming surveys. The difficulty, as pointed out in Holder (2004) and Aghanim et al. (2003), is that there exist degeneracies among the physically interesting parameters (T, v, τ) that can best be broken by choosing one frequency relatively low (around 30 GHz) and placing the other two around 150 GHz and 300 GHz. In addition, the observations need to be of arcminute-resolution to resolve individual clusters. A 30 GHz observing band is not a realistic option for upcoming arcminute-resolution bolometer based instruments (such as ACT, SPT, and APEX) since high-sensitivity bolometers sharply lose sensitivity below 90 GHz and the single-dish diameter required for arcminute-resolution observations at 30 GHz is unrealistically large. In addition, large interferometers capable of observing at 30 GHz with arcminute-resolution can only view small areas of the sky at a time, making a large survey impractical. Thus it is important to determine what information about individual galaxy clusters these future SZ surveys will be able to constrain given the reality that they will have approximately arcminute-resolution observations at or above 90 GHz.

In this paper we make a preliminary investigation of information we can potentially extract from SZ measurements. In particular, we do not include the effects of a variety of real world complications including radio and infrared point sources, galactic dust, non-SZ microwave fluctuations or instrumental systematic effects. While these are certainly important considerations for any data set, the goal of this paper is to elucidate the maximum information about individual clusters we can in principle obtain. Rough estimates of the impact of these various contributions are briefly discussed in §4.8. Detailed analysis including these effects is in progress.

In the next section we briefly summarize the SZ effect. In §4.3 we investigate how varying observing frequencies and detector sensitivity affects parameter degeneracies and parameter extraction. In §4.4 a Markov chain/Fisher matrix method is used to determine which cluster parameters can be well constrained by future SZ measurements, and in §4.5 this method is applied to simulated Nbody+gasdynamics clusters and the results presented. In §4.6 we discuss the near-linearity of the SZ intensity shift with respect to τT_e, τv_z, and τT_e^2, and show the resulting close correspondence between the constrained effective parameters from 2D SZ images and line-of-sight integrals through the 3D cluster. In §4.7 we show that an independent measurement of T_e breaks the parameter degeneracy and use a simple analytical model to show that the velocity thus determined is approximately the optical-depth-weighted velocity

integrated along the cluster line of sight. We then use a Markov chain to calculate errors on cluster velocities and optical depths given X-ray temperature priors. In §4.8 we discuss sources of contamination to the SZ signal, and we conclude with a summary of the above.

4.2 SZ Effect

When microwave photons pass through the hot gas in the intracluster medium of a galaxy cluster, roughly 1% of the photons interact with the free electrons in the gas. These photons are inverse Compton scattered and energy is transferred from the hot electrons to the cool photons, causing a slight distortion of the microwave background spectrum. This up-scattering of photons causes the intensity of photons with frequencies below about 220 GHz to decrease while the intensity of photons with higher frequencies increases. This process is called the thermal SZ effect, and it causes an effective temperature shift relative to the mean microwave background temperature on the order of one part in 10^4. If the galaxy cluster has some bulk velocity with respect to the microwave background rest frame, then this will Doppler shift the scattered microwave photons and cause an additional spectral distortion. This further shift in the microwave spectrum is referred to as the kinematic SZ effect and is typically an order of magnitude smaller than the thermal SZ effect. The derivation of the combined SZ effect can be found in Sunyaev & Zel'dovich (1970) and Sunyaev & Zel'dovich (1972), and more recent papers (e.g. Itoh et al. (1998); Nozawa et al. (1998)) have included relativistic corrections to these derivations.

The expression for the SZ effect we use throughout this work is from Nozawa et al. (1998) and is given by

$$\begin{aligned}\frac{\triangle I_\nu}{I_0} = &\frac{X^4 e^X}{(e^X-1)^2}\tau\theta_e\big[Y_0+\theta_e Y_1+\theta_e^2 Y_2+\theta_e^3 Y_3+\theta_e^4 Y_4\big]\\ &+\frac{X^4 e^X}{(e^X-1)^2}\tau(\frac{v_{\rm tot}}{c})^2\big[\frac{1}{3}Y_0+\theta_e(\frac{5}{6}Y_0+\frac{2}{3}Y_1)\big]\\ &+\frac{X^4 e^X}{(e^X-1)^2}\tau\frac{v}{c}\big[1+\theta_e C_1+\theta_e^2 C_2\big] \qquad (4.1)\end{aligned}$$

where $I_0 = 2(k_B T_{CMB})^3/(hc)^2$, $X = h\nu/k_B T_{CMB}$, $\theta_e = k_B T_e/m_e c^2$, $v_{\rm tot}$ is the peculiar velocity, v is the peculiar line-of-sight velocity, $\tau = \sigma_T \int n_e dl$ is the optical depth, and the Y's and C's are numbers that depend on frequency in a well-defined way. Note that θ_e is equivalent to the well known Compton-y parameter which we will show is tightly constrained. The most dominant terms in this expression are proportional to τT_e, τT_e^2, and τv. It is also important to note that the above expression is independent of redshift. This makes the SZ effect a powerful probe of the high-redshift universe because the amplitude of the SZ signal

does not weaken at high redshift (for fixed T, v, τ), unlike X-ray and optical signals. Since this microwave intensity shift for a given frequency is a non-trivial function of the cluster's gas temperature, peculiar velocity, and optical depth, one could hope that choosing at least three well placed observing frequencies would allow these three cluster parameters to be separated and measured. In practice, the observing frequencies and sensitivities available to upcoming SZ surveys result in degeneracies among these parameters. These degeneracies are illustrated in the next section.

4.3 Parameter Extraction

4.3.1 Creating Likelihood Surfaces

To understand the intrinsic limitations in determining a galaxy cluster's gas temperature, peculiar velocity, and optical depth from multi-frequency SZ measurements, we create likelihood surfaces for these parameters and compare the 1-σ regions for various choices of observing frequencies and detector sensitivity. We do this by first assuming some region of gas with uniform temperature T_e, peculiar line-of-sight velocity v, and total optical depth τ. We neglect any transverse peculiar velocity since the full SZ effect generates a temperature shift on the order of one part in 10^4, and the transverse velocity component of the SZ effect contributes a temperature shift on the order of one part in 10^7.

Using the expression for the intensity shift given in equation 4.1, we calculate the change in intensity one would measure from our fiducial gas region at three different observing frequencies. We perform these calculations for several frequency sets. The first observing frequency set we choose to be (30, 150, 300 GHz), which is the optimal frequency set found by Holder (2004) and roughly that found by Aghanim et al. (2003). We also choose the sets (90, 150, 300 GHz) and (145, 225, 265 GHz), the latter being the frequencies planned for ACT (see Kosowsky (2003)). After obtaining the intensity shift for each of the three frequencies in each set, we change variables to the ratios $x_1 = \Delta I_{\nu_1}/\Delta I_{\nu_2}$ and $x_2 = \Delta I_{\nu_3}/\Delta I_{\nu_2}$, where ν_1, ν_2, and ν_3 are the three frequencies in a set. These ratios are independent of τ (though their errors depend on τ), so we have two equations and two unknowns (T_e and v). We eliminated τ so that we could more easily construct and view the likelihood surfaces of the remaining parameters. Assuming first $1\mu K$ detector noise per arcminute beam and then $10\mu K$ noise per beam, we step through the $T_e - v$ parameter space and calculate the likelihood of the model described by (T_e, v), given the underlying fiducial model, in the usual way. Thus, we create a 2-dimensional likelihood surface for the parameters T_e and v for each observing frequency set at both detector noise

levels. A 1-σ contour is then drawn for each likelihood surface by connecting all the points with $\chi^2 = 2.3$ (e.g. Press et al. (1997)).

4.3.2 Degeneracy Between Cluster Gas Parameters

The 1-σ contours we obtain from these likelihood surfaces verify that the set of frequencies 30, 150, 300 GHz puts tighter constraints on T_e and v than the other sets. With $1\mu K$ detector noise per arcminute beam, the set 145, 225, 265 GHz exhibits a clear degeneracy between the T_e and v parameters, and with $10\mu K$ detector noise per arcminute beam all three frequency sets show significant degeneracy. Figure 4.1 shows the comparison of 1-σ contours for 10 keV (1.2×10^8 K) gas with a line-of-sight velocity of 200 km/sec, optical depth of 0.012, and $1\mu K$ detector noise. We choose gas parameters corresponding to a hot cluster because it is the case which has the highest signal-to-noise. These parameter values roughly correspond to the known cluster MS 0451 (Reese et al. 2002). The gas temperature is constrained to within 0.5 keV and its velocity to within 25 km/sec at the 1-σ level for 30, 150, and 300 GHz observing frequencies (Figure 4.1a). Shifting the lowest frequency to 90 GHz increases these uncertainties by a factor of two (Figure 4.1b). Using observing frequencies at 145, 225, and 265 GHz results in temperature uncertainties of 6 keV and velocity uncertainties of 220 km/sec (Figure 4.1c). Figure 4.2 shows the 1-σ likelihood contours for 10 keV gas with a line-of-sight velocity equal to -200 km/sec, optical depth of 0.012, and $1\mu K$ detector noise. Comparing these to the previous group of figures indicates that a negative line-of-sight velocity somewhat increases the uncertainties obtained for all frequency sets, as has been pointed out in Aghanim et al. (2003). Adding a 30 GHz or 90 GHz observing frequency to the 145, 225, 265 GHz frequency set with $1\mu K$ noise greatly reduces the 1-σ regions and makes the temperature and velocity constraints as tight as for the 30, 150, 300 GHz and 90, 150, 300 GHz frequency sets respectively. These results confirm previous results by Holder (2004) and Aghanim et al. (2003). It is clear that measurements near the null of the SZ effect are not particularly useful for SZ studies from a signal-to-noise perspective, but such measurements will be useful for microwave observations that aim to minimize SZ contamination and as a useful diagnostic of point source contamination.

With $10\mu K$ detector noise per arcminute beam, Figure 4.3 shows the 1-σ contours for the same 10 keV gas region with 200 km/sec line-of-sight velocity and an optical depth of 0.012. The gas temperature is constrained to within 5 keV and the velocity to within 200 km/sec at the 1-σ level for the 30, 150, and 300 GHz set (Figure 4.3a). Increasing the lower frequency to 90 GHz constrains the temperature to within 8 keV and the velocity to within 250 km/sec (Figure 4.3b). The 145, 225, and 265 GHz frequency set gives 1-σ errors of 9 keV and 350

km/sec for temperature and velocity respectively with $10\mu K$ detector noise (Figure 4.3c). Thus to constrain the cluster parameters well using SZ observations alone (in the absence of SZ signal contamination from point sources or residual primary microwave background), one needs both a low frequency band (90 GHz or lower) and a detector sensitivity not much higher than $1\mu K$ per arcminute beam.

We also compare the 1-σ likelihood contours for gas with different Compton-y parameters keeping the observing frequencies fixed. In Figure 4.4a we see the 1-σ contour for a 7 keV gas region with an optical depth of 0.009, 200 km/sec line-of-sight velocity, $1\mu K$ detector noise, and observing frequencies at 30, 150, and 300 GHz. Figure 4.4b shows the 1-σ contour for a 3 keV gas region with an optical depth of 0.004 and the same line-of-sight velocity, detector noise, and observing frequencies. The 1-σ contour for the gas region with lower Compton-y parameter shows a larger parameter degeneracy for the same set of observing frequencies and detector noise. This is because a decrease in Compton-y parameter lowers the signal-to-noise. The signal-to-noise is reduced by two effects as one moves to lower mass clusters: a lower signal in all bands and reduced relative importance of relativistic effects. We have verified that the former is a more important contributor to parameter degeneracies than the latter. Table 4.1 lists the above 1-σ errors on T_e and v for differing observing frequencies, detector noise, and Compton-y parameters for convenient reference.

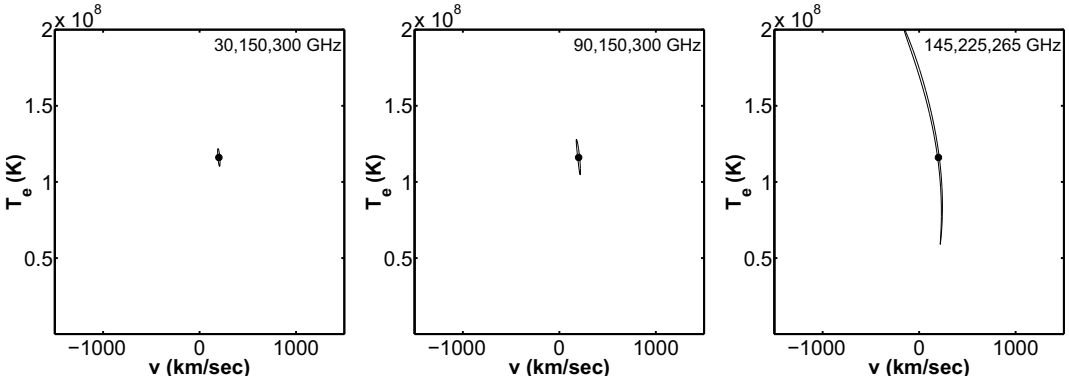

(a) (b) (c)

Figure 4.1 1-σ likelihood contours for a simulated region of gas of $T_e = 10$ keV (1.2×10^8 K), v = 200 km/sec, and $\tau = 0.012$ obtained by calculating the SZ effect for three different observing frequency sets assuming $1\mu K$ detector noise. The frequency sets are 1a) 30, 150, 300 GHz, 1b) 90, 150, 300 GHz, and 1c) 145, 225, 265 GHz. The SZ intensity shifts from the gas region are calculated using the formula in Nozawa et al. (1998), and the ratios of the intensity shifts at different frequencies in each set are computed to eliminate the dependence on optical depth. A dot (•) marks the input fiducial gas region.

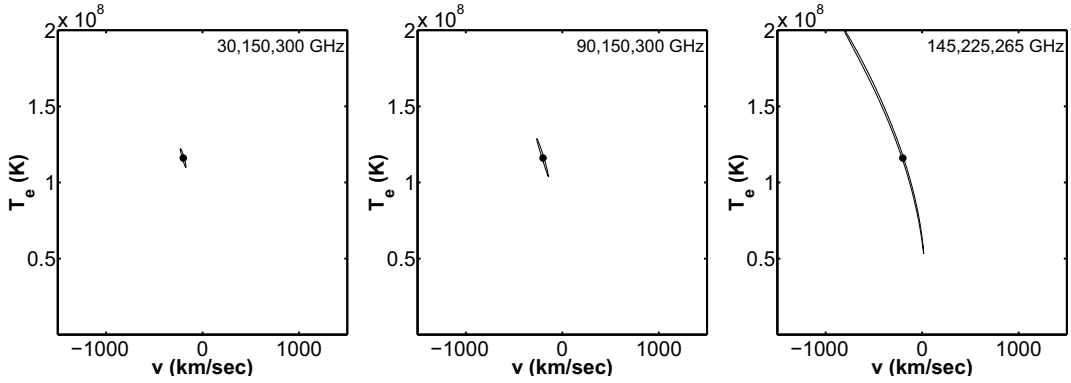

(a) (b) (c)

Figure 4.2 Same as Figure 4.1 except for v = -200 km/sec.

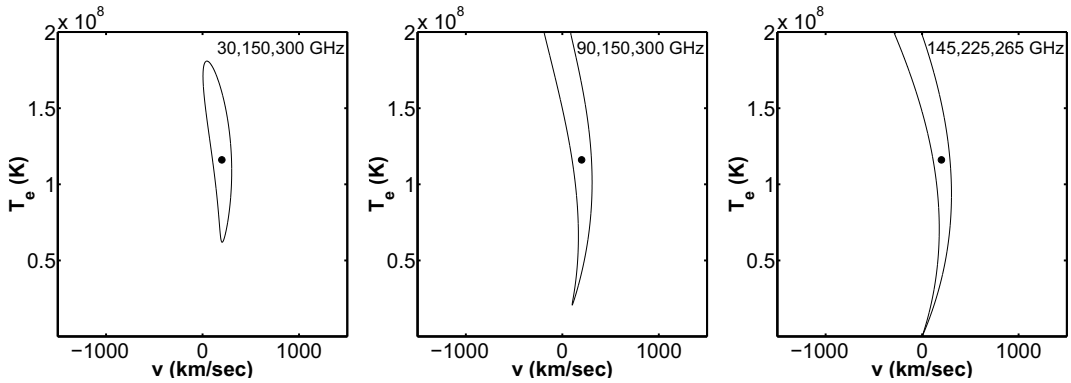

(a) (b) (c)

Figure 4.3 Same as Figure 4.1 except for detector noise of $10\mu K$.

4.4 Constrained Parameters From Future SZ Surveys

Despite the inability of upcoming experiments like ACT, SPT, and APEX to determine all of the cluster gas parameters, they will provide tight constraints on certain combinations of parameters. The next two sections explicitly demonstrate the parameter combinations which will be determined with good precision by these kinds of experiments.

4.4.1 Markov Chain Analysis

We create a Markov chain Monte Carlo (MCMC) using the parameters T_e, v, and τ to find realistic error regions for all three parameters. This MCMC is made using the Metropolis-Hastings algorithm which randomly steps through a parameter space and accepts all points whose likelihood is greater than the previous point. If the likelihood is less than the previous

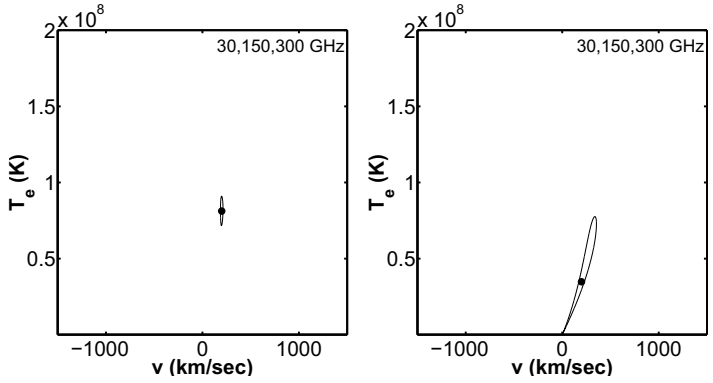

Figure 4.4 Same as Figure 4.1 except for gas T_e and τ values: a) $T_e = 7$ keV, $\tau = 0.009$; b) $T_e = 3$ keV, $\tau = 0.004$.

point, the current point is accepted with a probability given by the ratio of the two likelihoods. A comprehensive review of MCMCs can be found in Gilks et al. (1996); they were introduced into cosmology by Christensen & Meyer (2001), Christensen et al. (2001), Lewis & Bridle (2002), and Kosowsky et al. (2002). The region in the 3-dimensional parameter space containing 68% of all the points accepted in the chain we define as the 1-σ region. This 1-σ region is projected onto 2 dimensions in the figures below. Figure 4.5 shows the 1-σ regions generated by a MCMC for 10 keV gas with 200 km/sec line-of-sight velocity and an optical depth of 0.012. The frequency set 145, 225, and 265 GHz was used with $1\mu K$ detector noise per beam to simulate ACT observations. In the Markov chain, the parameter space was restricted to $T_e \in (0, 2 \times 10^8$ K (17 keV)), $\tau \in$(0, 0.02), and $v \in$(-1500 km/sec, 1500 km/sec), and 5 million steps were used with about 50% acceptance rate in the chain. In addition, each step was taken in all three parameter directions simultaneously with different step sizes in each parameter direction. From the 1-σ regions in Figure 4.5, we can see a clear degeneracy among all three parameters.

Figure 4.6 shows the same 1-σ region as Figure 4.5 except using the parameter directions τT_e, τT_e^2, and τv. We have verified that the MCMC in either variable set gives the same results, although it is significantly more efficient to use the second set of variables. We choose this set of parameters since these are the dominant terms in the intensity shift expression in equation 4.1. These figures demonstrate that the cluster parameters lie in a nearly 1-dimensional subspace of the 3-dimensional parameter space given by τT_e, τT_e^2, and τv. We can find two axes within this parameter space (both orthogonal to the degeneracy direction) along which the cluster parameters are tightly constrained and one axis (parallel to the degeneracy direction) along which the cluster parameters are largely unconstrained.

Observing Frequencies (GHz)	Detector Noise ($1\mu K$)	kT_e (keV)	v (km/sec)	τ	σ_{T_e} (keV)	σ_v (km/sec)
30, 150, 300	1	10	200	0.012	0.5	25
90, 150, 300	1	10	200	0.012	1	50
145, 225, 265	1	10	200	0.012	6	220
30, 150, 300	1	10	-200	0.012	0.5	50
90, 150, 300	1	10	-200	0.012	1	100
145, 225, 265	1	10	-200	0.012	6.5	400
30, 145, 225, 265	1	10	200	0.012	0.5	25
90, 145, 225, 265	1	10	200	0.012	1	50
30, 150, 300	10	10	200	0.012	5	200
90, 150, 300	10	10	200	0.012	8	250
145, 225, 265	10	10	200	0.012	9	350
30, 150, 300	1	7	200	0.009	1	50
30, 150, 300	1	3	200	0.004	3.5	200

Table 4.1 The 1-σ errors on T_e and v for different observing frequencies, detector noise, and gas parameters.

4.4.2 Fisher Matrix Determination of Constrained Parameters

The three orthogonal directions in this parameter space that allow us to tightly constrain the gas parameters in two directions with one direction unconstrained correspond to the principal axes of the 1-σ error ellipsoid which is projected in 2 dimensions in Figure 4.6. To find these principal axes we calculate a Fisher matrix at the most likely point found by the MCMC. The Fisher matrix describes the curvature of the likelihood surface at a given point in parameter space. It is expressed by the formula

$$F_{\alpha\beta} = \left\langle -\frac{d^2 \ln \mathcal{L}}{dp_\alpha dp_\beta} \right\rangle . \tag{4.2}$$

Since we have $\mathcal{L} \propto e^{-\chi^2/2}$, the Fisher matrix becomes $F_{\alpha\beta} = \frac{1}{2}\frac{d^2\chi^2}{dp_\alpha dp_\beta}$. Using

$$\chi^2 = \sum_{i=1}^{3} \left(\frac{\Delta I_{\nu_i}(\boldsymbol{p}) - \Delta I^o_{\nu_i}}{e_{\nu_i}} \right)^2 , \tag{4.3}$$

where $\boldsymbol{p} = (\tau T_e/(10^6 \text{ K}), \tau v/(1 \text{ km/sec}), \tau T_e^2/(10^{14} \text{ K}^2))$, $\Delta I^o_{\nu_i}$ is the observed ΔI_{ν_i}, and e_{ν_i} is the error on $\Delta I^o_{\nu_i}$, and averaging gives

$$F_{\alpha\beta} = \sum_{i=1}^{3} \frac{1}{(e_{\nu_i})^2} \frac{\partial \Delta I_{\nu_i}(\boldsymbol{p})}{\partial p_\alpha} \frac{\partial \Delta I_{\nu_i}(\boldsymbol{p})}{\partial p_\beta}. \tag{4.4}$$

(See Dodelson (2003) for a good explanation of the Fisher matrix and its applications.) The eigenvectors of the Fisher matrix evaluated at the minimum point of χ^2 correspond to the principal axes of the error ellipsoid.

This technique is essentially a version of principal component analysis (PCA). In PCA it is known that the principal components one finds depend on how the variables are scaled. There is no single correct scaling to choose, but the one that is widely preferred in physical uses is scaling all the variables to order unity, which has the advantage that all the variables are weighted the same. (Jackson (1991) provides a good overview of PCA.) We scale τT_e, τv, and τT_e^2 by 10^6 K, 1 km/sec, and 10^{14} K^2 respectively, which are characteristic cluster values for these variables.

The principal axes are linear combinations of the previous parameter directions such that

$$\boldsymbol{a} = \mathrm{C}(\boldsymbol{p}_*)\boldsymbol{p}, \tag{4.5}$$

where the rows of $\mathrm{C}(\boldsymbol{p}_*)$ are the eigenvectors of F, $\boldsymbol{a} = (a, b, c)$ is a point in the new parameter space, and $\boldsymbol{p}$ are the old parameter directions described above. The vector $\boldsymbol{p}_*$ describes $\boldsymbol{p}$ evaluated at the maximum likelihood point. Note $\mathrm{C}(\boldsymbol{p}_*)$ (and thus $\boldsymbol{a}$) will differ with $\boldsymbol{p}_*$, but the variation with $\boldsymbol{p}_*$ is fairly weak for realistic parameter regions. Roughly, the Fisher matrix eigenvectors are $\boldsymbol{e}_1 = (1, 0, 0)$, $\boldsymbol{e}_2 = (0, 0.4, 0.9)$, and $\boldsymbol{e}_3 = (0, 0.9, 0.4)$ normalized to unity. Therefore the a parameter is dominated by τT_e, and the b and c parameters are primarily linear combinations of τv and τT_e^2. Thus, SZ measurements provide precise measures of the y parameter and one linear combination of the kinematic SZ effect and the relativistic corrections.

Figure 4.7 shows that the gas parameters for this fiducial model are constrained to within 1% in the a direction, 3% in the b direction, and 70% in the c direction. For a 4 keV gas region with 200 km/sec line-of-sight velocity, an optical depth of 0.005, and detector noise of $1\mu K$, the gas parameters are constrained to within 4% in the a direction, 16% in the b direction, and 200% in the c direction. The gas parameters are constrained to within 8%, 22%, and 160% in the a, b, and c directions respectively for a 10 keV gas region with 200 km/sec line-of-sight velocity, an optical depth of 0.012, and $10\mu K$ detector noise.

The a and b parameters, which are linear combinations of τT_e, τT_e^2, and τv, are therefore well constrained by an ACT-like SZ survey with observing frequencies near 145, 225, and 265 GHz and $1\mu K$ detector noise. This technique can be applied to determine the constrained gas parameters from any multi-frequency SZ observations that are without arcminute-resolution observations at frequencies below 100 GHz or that have low frequency information but with a noise component considerably larger than $1\mu K$. By combining this gas information from SZ surveys with a data set that can constrain just one of the parameters T_e, τ, v (such as an X-ray survey of clusters that constrains T_e for each cluster), all three cluster gas parameters can be well determined.

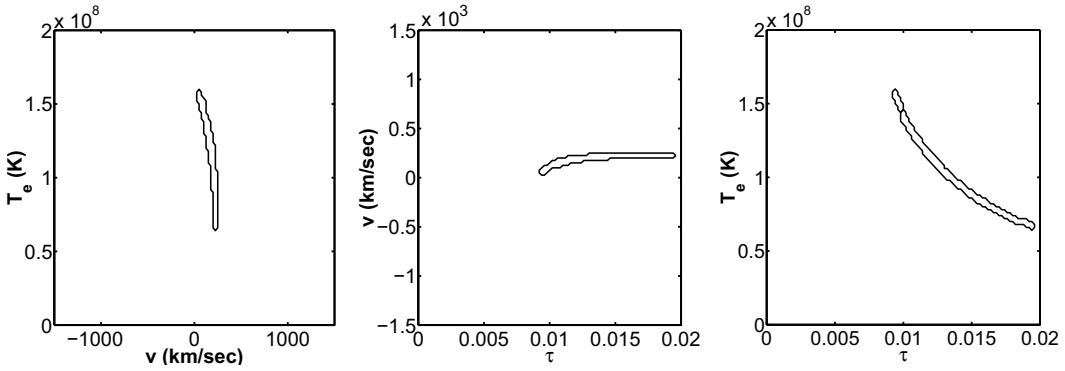

(a) (b) (c)

Figure 4.5 Projected 1-σ likelihood contours for the (T_e, v, τ) parameter space from SZ intensity shifts at 145, 225, and 265 GHz for a simulated gas region of $T_e = 10$ keV (1.2×10^8 K), $v =$ 200 km/sec, and $\tau = 0.012$ assuming $1\mu K$ detector noise.

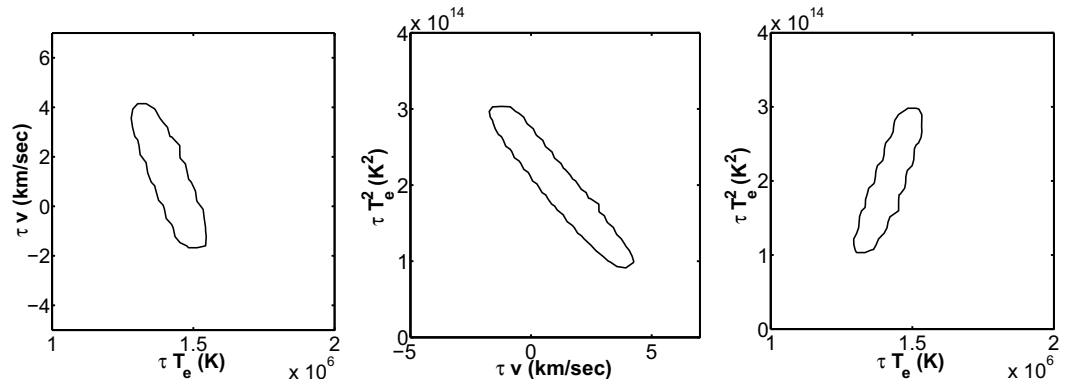

(a) (b) (c)

Figure 4.6 Same as Figure 4.5 except for the parameter space (τT_e, τv, τT_e^2), corresponding to the physical parameters expected to be important.

4.5 Results Using Simulated Clusters

We now apply this technique to simulated SZ observations which we generate using simulated galaxy clusters. In §4.5.1 we describe the two simulated clusters we use, one about 9 keV and the other about 3 keV, and in §4.5.2 we discuss how SZ simulations are created from these. The results of applying the technique in §4.4 to simulated ACT-like SZ maps of both clusters and to simulated Planck-like SZ maps of the 9 keV cluster are contained in §4.5.3.

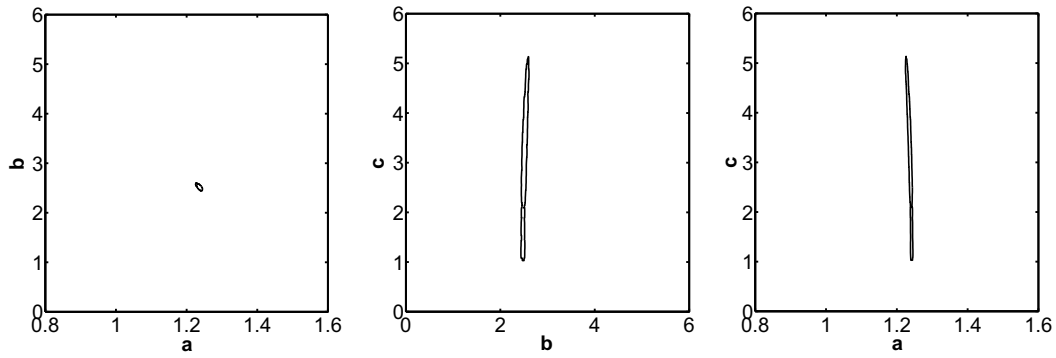

(a) (b) (c)

Figure 4.7 Same as Figure 4.5 except for the parameter space (a, b, c), the combinations of the physical parameters that are best constrained by SZ observations.

4.5.1 Cluster Simulations

The clusters we use are two high-resolution 3D cluster simulations that were made using the Adaptive Refinement Tree (ART) Nbody+gasdynamics code (Kravtsov 1999; Kravtsov et al. 2002). These clusters were simulated using a ΛCDM model with $\Omega_m = 0.3$, $\Omega_b = 0.043$, $h = 0.7$, and $\sigma_8 = 0.9$. Each cluster has a redshift of z=0.43 and is contained in a cube of side length 2 Mpc ($\simeq$ 6 arcminutes). Each grid element within the larger cube has a side length of 0.0078 Mpc ($\simeq$ 0.02 arcminute). The simulations track the density of dark matter particles, the density of gas particles, the gas temperature, and the 3-dimensional gas velocity for each grid element. One cluster is similar in size to the Coma cluster and has a mass of $\simeq 10^{15} M_{\odot}$, an optical depth of $\simeq 0.01$, and an average gas temperature of 9 keV. The other cluster is similar in size to the Virgo cluster and has a mass of $\simeq 2 \times 10^{14} M_{\odot}$, an optical depth of $\simeq 0.005$, and an average gas temperature of 3 keV. Both clusters have characteristic bulk velocities of several hundred km/sec. The morphology of the Virgo-size cluster indicates that it consists of a recent merger of two smaller clusters. These cluster simulations do not include the effects of gas cooling, stellar feedback, magnetic fields, and thermal conduction. For a more detailed cluster description see Nagai & Kravtsov (2003) and Nagai et al. (2003).

4.5.2 SZ Map Generation

To create a simulation of an SZ observation, we choose one of the cluster simulations and a set of observing frequencies. The SZ intensity shift that microwave photons would experience passing through each grid element is calculated using equation 4.1 and the gas temperature, gas density, and gas velocity of each element. Every ΔI is then integrated over a frequency band centered

around each observing frequency in the set. We use a 3 GHz frequency bandwidth, as opposed to a more realistic bandwidth of $\simeq 25$ GHz, for numerical convenience. However, the bandwidth size has a negligible effect on cluster constraints, which we verified by redoing some of our results with a 25 GHz bandwidth. Thus, for each frequency band we end up with an SZ cube of ΔI values. This cube is then projected along the line of sight into a two-dimensional SZ distortion of the sky. We do not include the primary microwave background in our simulations, assuming it is perfectly subtracted, since it varies on scales large compared to the cluster. The main effect of residual primary microwave contamination will be as a source of noise for extracting estimates of the peculiar velocity from the constrained parameters. Figure 4.8 and 4.9 show the 2D SZ images of the 9 keV and 3 keV clusters after this projection process for the frequency bands centered on 145, 225, and 265 GHz. After creating a 2D SZ image for each observing frequency band, we smooth each image by convolving it with a Gaussian beam, and increase the pixel size of our images to sizes realistic for upcoming SZ surveys by averaging together smaller pixels. Finally, Gaussian random noise of standard deviation equal to our chosen detector sensitivity is added to each 2D pixel.

We make SZ simulations using ACT instrument specifications for both the 3 keV and 9 keV clusters and using Planck specifications for the 9 keV cluster only. The ACT-like SZ images of the 9 keV cluster (assuming perfect microwave background and point source removal) are shown in Figure 4.10. For these images we use the frequency bands centered on 145, 225, and 265 GHz. We assume a beam size of 1 arcminute and choose a pixel size of 0.3' x 0.3'. Each 0.3 arcminute pixel is given $3\mu K$ of Gaussian random detector noise. Our results are not qualitatively different for moderately different noise levels between channels. Figure 4.11 shows SZ simulations of the 3 keV cluster with ACT specifications as above. For comparison, we also made maps appropriate to the Planck experiment, with a beam size of 4 arcminutes and detector noise of $16\mu K$ per 2' x 2' pixel, at the same frequencies as the ACT maps (which are similar to the actual Planck bands centered at 143, 217, and 353 GHz).

4.5.3 Parameter Constraints from Simulated 3D Clusters

We now apply the Markov chain/Fisher matrix technique described in §4.4 to the simulated ACT-like and Planck-like SZ images of the simulated clusters. The only change is that in equation 4.3 we assume $3\mu K$ noise for ACT-like images and $16\mu K$ noise for Planck-like images. The cluster parameters we constrain using this method are really effective parameters that correspond to integrals of the cluster parameters along a line of sight. The SZ intensity (eq. [4.1]) is not linear, so there is no guarantee that the sum of SZ signals of varying temperature

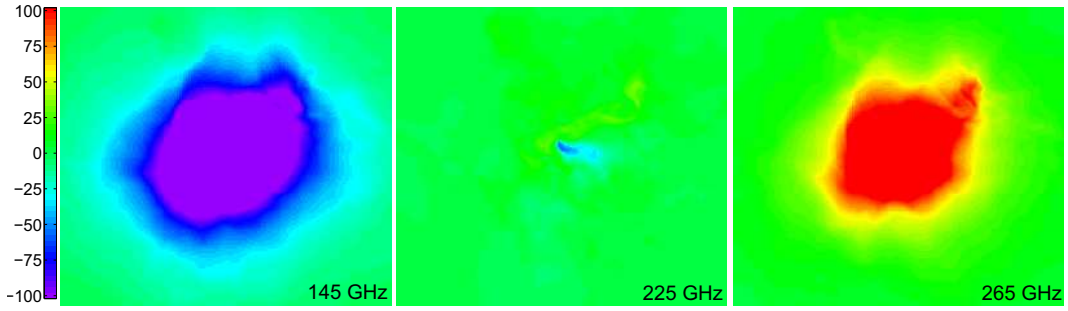

(a) (b) (c)

Figure 4.8 SZ simulations of a simulated Nbody+hydro cluster before smoothing and adding detector noise. The cluster is about $10^{15} M_{\odot}$, has an average gas temperature of about 9 keV, and is at z=0.43. Figures a, b, and c are of the 145, 225, and 265 GHz bands respectively. Each figure is about 6' x 6' with a pixel size of 0.02' x 0.02'. The images are converted to temperature differences from the mean microwave background temperature. The color scale is from -100μK to 100μK. Primary microwave background fluctuations and point source contamination are not included.

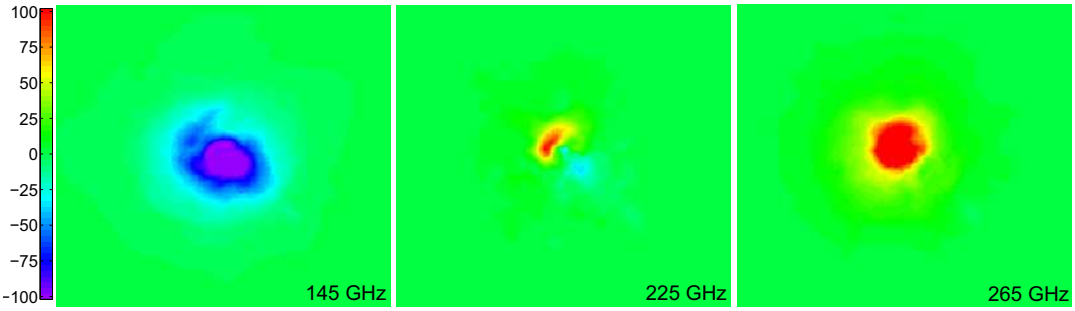

(a) (b) (c)

Figure 4.9 Same as Figure 4.8 except the cluster is about $2 \times 10^{14} M_{\odot}$ and has an average gas temperature of about 3 keV.

and velocity can be fit to a single temperature and velocity. We fit the resulting SZ intensity as a function of frequency to a model with a single temperature and velocity and call the constrained parameters $\boldsymbol{a}_{\rm eff}$; we discuss what integrals these effective parameters correspond to within the three dimensional cluster in §4.6.

Figure 4.12 shows the projected 1-σ contours for the $\boldsymbol{a}_{\rm eff}$ parameters for the central pixel of ACT-like SZ images of the simulated 9 keV cluster. We do this analysis on a pixel-by-pixel basis to potentially obtain the most information about cluster substructure. (See Nagai et al. (2003) for some discussion of substructure.) In a low signal-to-noise experiment or as a means to average out substructure, it could be advantageous to add together pixels. The 1-σ errors on $a_{\rm eff}$, $b_{\rm eff}$, and $c_{\rm eff}$ for this central pixel are 0.06, 0.5, and 5 respectively. The range of parameters

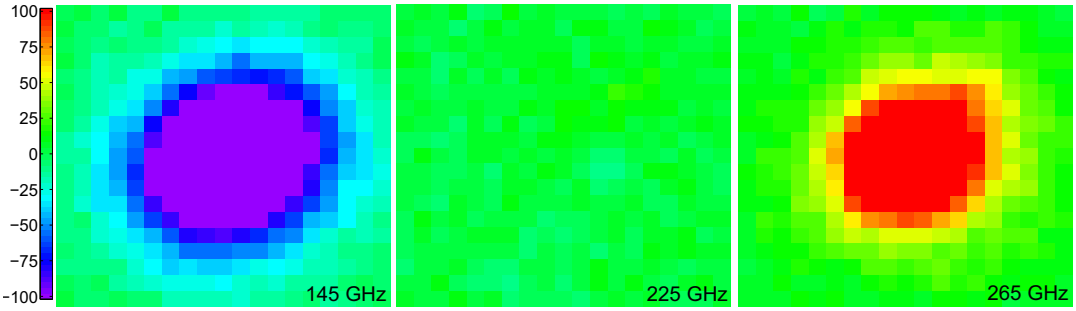

(a) (b) (c)

Figure 4.10 ACT-like SZ simulations of the 9 keV simulated cluster shown in Figure 4.8 with 1' resolution and $3\mu K$ gaussian random instrument noise in each 0.3' x 0.3' pixel. The remaining figure specifications are the same as in Figure 4.8.

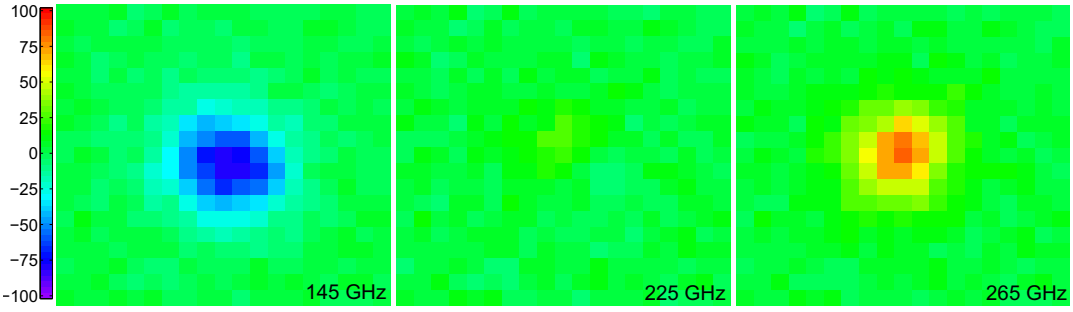

(a) (b) (c)

Figure 4.11 Same as Figure 4.10 except using the 3 keV simulated cluster shown in Figure 4.9.

$T \in (0, 2 \times 10^8$ K), $\tau \in (0, 0.02)$, and $v \in$ (-1500 km/sec, 1500 km/sec) correspond to ranges of about $a \in (0, 4)$, $b \in (-5, 20)$, and $c \in (-30, 24)$. Clusters with larger SZ signals (and thus larger T_e's and τ's) tend to have larger a, b, and c parameters, and this is borne out in the comparison of our results for the 9 keV and 3 keV clusters. Since the a, b, and c parameters have been scaled to roughly order unity for characteristic cluster values, the absolute errors are a meaningful reflection of how well the gas properties are constrained.

Similar results are obtained from the ACT-like SZ simulation of the 3 keV cluster and the Planck-like SZ simulation of the 9 keV cluster. Figure 4.13 shows the projected 1-σ contours for the central pixel of the ACT-like SZ images of the 3 keV cluster. These figures demonstrate $\sigma_{a_{\rm eff}} \simeq 0.02$, $\sigma_{b_{\rm eff}} \simeq 0.2$, and $\sigma_{c_{\rm eff}} \simeq 1.5$. Thus $a_{\rm eff}$, $b_{\rm eff}$, and $c_{\rm eff}$ are constrained to a small region of the available parameter space, with the first two components especially well-constrained. Figure 4.14 shows the projected 1-σ contours for the central pixel of the Planck-like SZ images of the 9 keV cluster. These figures show $\sigma_{a_{\rm eff}} \simeq 0.06$, $\sigma_{b_{\rm eff}} \simeq 0.7$, and $\sigma_{c_{\rm eff}} \simeq 3$, indicating again

that the measurements are providing strong constraints within the available parameter space.

These results demonstrate that the $a_{\rm eff}$ and $b_{\rm eff}$ cluster parameters are well constrained and $c_{\rm eff}$ is moderately well constrained by SZ observations typical of ACT and Planck, assuming perfect primary microwave background and point source removal.

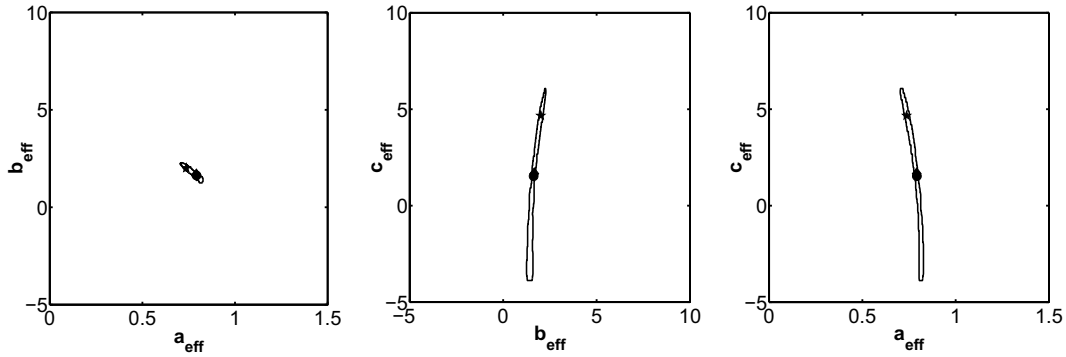

(a) (b) (c)

Figure 4.12 The projected 1-σ contours of the likelihood surface for the ($a_{\rm eff}$, $b_{\rm eff}$, $c_{\rm eff}$) parameter space from the central pixel of simulated ACT-like SZ images of a simulated 9 keV Nbody+hydro cluster. The likelihood contours are generated using a Markov chain and are for a given noise realization. The star (★) indicates the best fit $\boldsymbol{a}_{\rm eff}$ values from the Markov chain. The dot (•) indicates the best fit $\boldsymbol{a}_{\rm eff}$ values obtained with an ideal instrument without detector noise. A diamond shape (♦) marks the values of line-of-sight integrals through the three dimensional cluster.

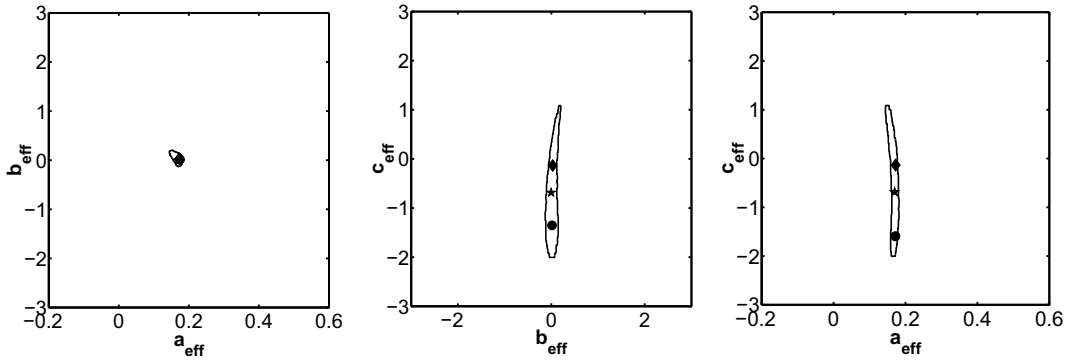

(a) (b) (c)

Figure 4.13 The projected 1-σ contours of the likelihood surface for the ($a_{\rm eff}$, $b_{\rm eff}$, $c_{\rm eff}$) parameter space from the central pixel of simulated ACT-like SZ images of a simulated 3 keV Nbody+hydro cluster. The symbols within the contours are as for Figure 4.12; note the axes are different scales.

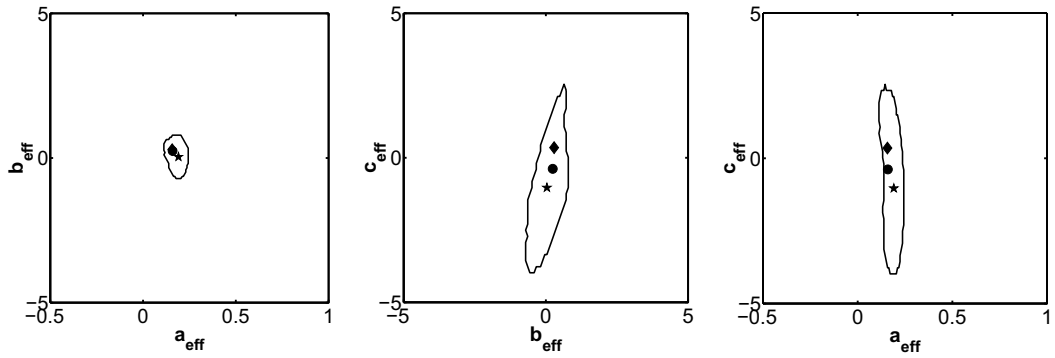

(a) (b) (c)

Figure 4.14 The projected 1-σ contours of the likelihood surface for the ($a_{\rm eff}$, $b_{\rm eff}$, $c_{\rm eff}$) parameter space from the central pixel of simulated Planck-like SZ images of a simulated 9 keV Nbody+hydro cluster. The symbols within the contours are as for Figure 4.12; note the axes are different scales.

4.6 Correspondence Between Constrained Effective Parameters and Line-of-Sight Integrals

The cluster gas parameters we have constrained in the previous sections using a projected two dimensional SZ image correspond to integrals along the line of sight of the three dimensional cluster. Previous studies of cluster projection effects have been done indicating that the temperature in principle obtainable from SZ measurements is really a Compton-averaged quantity (i.e. each line-of-sight integral of T_e is weighted by the Compton parameter) (Hansen 2004b; Knox et al. 2004). Here we show that the line-of-sight integrals corresponding to the $\boldsymbol{a}_{\rm eff}$ parameters are even more straightforward.

The reason for the simple correspondence is that the SZ intensity shift given by equation 4.1 is nearly linear with respect to τT, τv, and τT^2. These three terms are the most dominant terms in the expression and represent most of the change in intensity for temperatures of several keV and velocities of several hundred km/s. If ΔI_ν were exactly a function only of τT, τv, and τT^2 in equation 4.1, then ΔI_ν would be exactly a linear function of a, b, and c. In that case, the measured $\boldsymbol{a}_{\rm eff}$ would be equal to $\sum {\rm C}\boldsymbol{p}_i$, where C is given in equation 4.5, and the sum is over the gas properties $\boldsymbol{p}_i$ of each element i along the line of sight.

The full SZ intensity shift expression in equation 4.1 includes terms non-linear in τT, τv, and τT^2. However, the addition of these non-linear terms in the calculation of ΔI_ν integrated along a line of sight only introduces a slight bias between $\boldsymbol{a}_{\rm eff}$ and $\int {\rm C} d\boldsymbol{p}_i$. In Figures 4.12-4.14, within the 1-σ contours of $\boldsymbol{a}_{\rm eff}$, we indicate the best fit $\boldsymbol{a}_{\rm eff}$ found by the MCMC, for a

given noise realization, by a star (★). The best fit $\boldsymbol{a}_{\rm eff}$ obtained if the clusters are observed with an ideal instrument without detector noise are indicated by dots (•). Diamond shapes (⧫) mark the values of the line-of-sight integrals given by $\int \mathrm{C} d\boldsymbol{p}_i$ and calculated using the 3D cluster simulations. In Figure 4.12a, the difference between $a_{\rm eff}$ from an ideal, no noise instrument and from the line-of-sight integral is $\Delta a = 0.001$. The difference between $b_{\rm eff}$ from an ideal instrument and from the line-of-sight integral is $\Delta b = -0.03$. Clearly, in the absence of detector noise, the correspondence between $a_{\rm eff}$ and $b_{\rm eff}$ and the line-of-sight integrals is very close. Moreover, the difference between $a_{\rm eff}$ and $b_{\rm eff}$ and the line-of-sight integrals given realistic detector noise is still well within the 1-σ errors on $a_{\rm eff}$ and $b_{\rm eff}$ given by the MCMC. Similar results can be seen in Figures 4.13a and 4.14a. These simulations demonstrate an agreement to within 1-σ between the $a_{\rm eff}$ and $b_{\rm eff}$ parameters constrained by SZ measurements and line-of-sight integrals given by $\int \mathrm{C} d\boldsymbol{p}_i$.

Figure 4.15 shows this correspondence more explicitly. Plotted on the y-axis are best-fit $\boldsymbol{a}_{\rm eff}$ obtained via a MCMC using intensities from simulated noise-free SZ images of the 9 keV and 3 keV clusters assuming ACT-like observations. On the x-axis are plotted $\int \mathrm{C} d\boldsymbol{p}_i$ for the corresponding lines of sight. Four different lines of sight through both the 9 keV and 3 keV simulated clusters are plotted. These lines of sight are 0', 1', 1.5', and 2' from the central pixel of the simulated SZ images. Filled shapes correspond to the 9 keV cluster and unfilled shapes to the 3 keV cluster. For the $a_{\rm eff}$ and $b_{\rm eff}$ parameters, which can be well constrained, their equivalence to $\int \mathrm{C} d\boldsymbol{p}_i$ is extremely close. This confirms the near linearity of the SZ intensity shift with respect to the a, b, and c parameters. The $c_{\rm eff}$ parameters demonstrate some scatter around the $y = x$ line, and this is because the degeneracy in the c direction prevents a MCMC from settling on the correct $c_{\rm eff}$ value.

If we could tightly constrain $a_{\rm eff}$, $b_{\rm eff}$, and $c_{\rm eff}$ via SZ measurements, we could solve for the quantities τT_τ, τv_τ, and $\tau(T^2)_\tau$, where the subscript τ corresponds to optical-depth-weighted integrals (e.g. $T_\tau = \int T d\tau / \int d\tau$). From these one can find T_y, $\tau T_\tau / T_y$, and $v_\tau T_y / T_\tau$, following the algebra in Knox et al. (2004), where the subscript y corresponds to a pressure-weighted integral. Therefore SZ measurements would constrain the pressure-weighted temperature (arising from the relativistic corrections), the optical-depth-weighted velocity times a correction factor and the optical depth times a similar correction factor which is the ratio of different weighted temperatures. Since degeneracies will allow SZ measurements to constrain only $a_{\rm eff}$ and $b_{\rm eff}$, information from an external source will be needed to constrain the above physically interesting quantities.

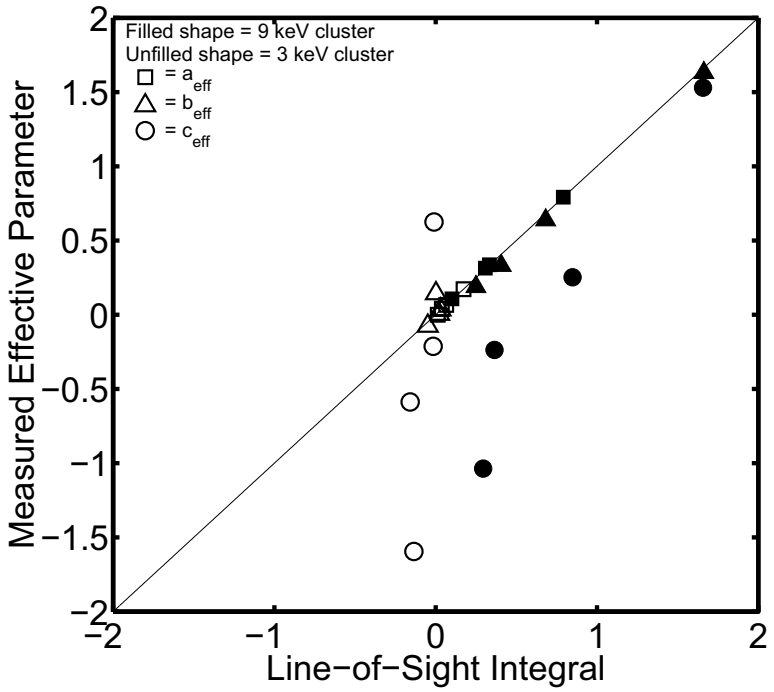

Figure 4.15 Best fit $\boldsymbol{a}_{\rm eff}$ from simulated, noise-free, ACT-like SZ images found using a Markov chain versus $\int C d\boldsymbol{p}$ integrated along the cluster line of sight. The results for four different lines of sight through both the 9 keV and 3 keV simulated clusters are plotted. The lines of sight are 0', 1', 1.5', and 2' from the central pixel of the simulated SZ images. $d\boldsymbol{p} = (Td\tau, vd\tau, T^2 d\tau)$, and C is a matrix of constants introduced in equation 4.5. $\square = a_{\rm eff}$, $\triangle = b_{\rm eff}$, and $\bigcirc = c_{\rm eff}$, and filled (unfilled) shapes correspond to the 9 keV (3 keV) cluster. Typical error bars for $1\mu K$ detector noise per 1' beam are $\pm$ 0.04, $\pm$ 0.3, and $\pm$ 3 for $a_{\rm eff}$, $b_{\rm eff}$, and $c_{\rm eff}$ respectively.

4.7 Breaking Parameter Degeneracy with an X-Ray Measurement of T_e

4.7.1 Measured Effective Velocity is approximately $\int v d\tau / \int d\tau$

Assuming contamination sources can be dealt with effectively, future SZ observations should be able to constrain two quantities given by

$$a_{\rm eff} \approx \tau(c_1 T_\tau + c_2 (T^2)_\tau) + c_3 \tau v_\tau \quad \text{and} \tag{4.6}$$

$$b_{\rm eff} \approx \tau(c_4 T_\tau + c_5 (T^2)_\tau) + c_6 \tau v_\tau, \tag{4.7}$$

where the c's are elements of the matrix C defined in equation 4.5. It is conceivable that temperature measurements from an X-ray survey of clusters could allow the determination of τ and v_τ.

Formally X-ray observations would need to provide a constraint on $c_i T_\tau + c_j (T^2)_\tau$, where the

c's are known constants. However, T_τ and $(T^2)_\tau$ are not obviously given by X-ray observations. An X-ray derived temperature is also not equivalent to T_τ. The two may differ by as much as 1 keV (Mathiesen & Evrard 2001). If X-ray observations gave $T_x = T_\tau$ and it was true that $(T_\tau)^2 = (T^2)_\tau$, then the effective velocity we would get from a MCMC, after adding the T_x prior, would be equal to v_τ. For our 9 keV simulated cluster, $(T_\tau)^2$ and $(T^2)_\tau$ agree to within 5% on average, and for our 3 keV simulated cluster, the two agree to within 12% on average.

To get an estimate of the biases incurred by not having the correct weighted temperatures, we assume $(T_\tau)^2 = (T^2)_\tau$ and add a temperature prior of T_τ to our MCMC. Adding a T_τ prior, in the manner we discuss further in §4.7.2, we find for the central pixel of the 9 keV cluster, from simulated, noise-free, ACT-like SZ images, an effective velocity of 230 km/sec from the MCMC and an optical-depth-weighted line-of-sight velocity of 218 km/sec from the three dimensional cluster simulation. For the central pixel of the 3 keV cluster SZ image, we find an effective velocity of -10 km/sec from the MCMC and an optical-depth-weighted line-of-sight velocity of -3 km/sec from the three dimensional cluster simulation. The bias between the velocity from the MCMC and v_τ is most likely due to the breakdown of the $(T_\tau)^2 = (T^2)_\tau$ assumption.

To quantify the bias incurred from T_x differing from T_τ, we add a $\pm$ 1 keV offset to our T_τ prior. We find for the central pixel of the 9 keV cluster SZ image, an effective velocity of 228 km/sec from the MCMC for both + and - 1 keV offsets. We find for the central pixel of the 3 keV cluster SZ image, an effective velocity of -45 km/sec from the MCMC for a + 1keV offset and an effective velocity of 6 km/sec for a - 1 keV offset. This would suggest a total bias between the measured effective velocity and v_τ of about 15 km/sec for the 9 keV cluster and between 10 and 40 km/sec for the 3 keV cluster.

4.7.2 MCMC Errors on $v_{\rm eff}$ and τ Given an X-ray $T_{\rm eff}$ Prior

To determine realistic errors on $v_{\rm eff}$ and τ from adding a measurement of $T_{\rm eff}$ to our simulated SZ data, we again use a MCMC. We weight each point in our MCMC by the factor $e^{-((T-T_{\rm eff})/\Delta T_{\rm eff})^2/2}$ where we calculate $T_{\rm eff} = \int T_e d\tau / \int d\tau$ from the 3D cluster simulation and $\Delta T_{\rm eff}$ is the assigned measurement error on $T_{\rm eff}$.

For a 1 keV error on $T_{\rm eff}$, our ACT simulation of the 9 keV cluster gives $\sigma_v = 20$ km/sec and $\sigma_\tau = 0.002$ for the central pixel. Our ACT simulation of the 3 keV cluster gives $\sigma_v = 60$ km/sec and $\sigma_\tau = 0.004$ for the central pixel. Assuming a 2 keV error on $T_{\rm eff}$, the ACT simulation of the 9 keV cluster gives $\sigma_v = 40$ km/sec and $\sigma_\tau = 0.004$, and the ACT simulation of the 3 keV cluster gives $\sigma_v = 100$ km/sec and $\sigma_\tau = 0.005$. Our Planck simulation of the 9 keV cluster

gives $\sigma_v = 500$ km/sec and $\sigma_\tau = 0.0024$ for a 1 keV error on $T_{\rm eff}$ and $\sigma_v = 560$ km/sec and $\sigma_\tau = 0.0062$ for a 2 keV error, for the central pixel. Table 4.2 lists these 1-σ errors for convenient reference.

The errors obtained on σ_v and σ_τ from our MCMC are smaller than those obtained using a Fisher matrix. However, the MCMC errors are more accurate than those from a Fisher matrix since a Fisher matrix approximates the likelihood surface by an ellipsoidal Gaussian, which can result in overestimated errors for likelihood surfaces with strong spatial curvature such as these. These results show that, in the absence of contamination from imperfect point source and primary microwave background removal, adding X-ray temperature measurements to the data from upcoming ACT-like SZ surveys can determine cluster peculiar velocities to within 100 km/sec or less. Large-scale velocity fields obtained from galaxy clusters out to high redshift could provide an interesting probe of dark matter and dark energy.

Simulated Experiment	Simulated Cluster Avg. Temp. (keV)	Error on Temp. Prior (keV)	σ_τ	σ_v (km/sec)
ACT-like	9	1	0.002	20
ACT-like	3	1	0.004	60
ACT-like	9	2	0.004	40
ACT-like	3	2	0.005	100
Planck-like	9	1	0.002	500
Planck-like	9	2	0.006	560

Table 4.2 The 1-σ errors on τ and v for ACT-like and Planck-like experiments using 9 keV and 3 keV simulated clusters with varying errors on the temperature prior $T_{\rm eff}$.

4.8 Sources of Contamination to the SZ Signal

Major sources of possible contamination have been neglected in this exercise. In particular, it is possible that primary and secondary microwave fluctuations and point sources (both radio and infrared) could be problematic.

Primary fluctuations are in some ways both the largest and the smallest concern. The fluctuation amplitudes are on the order of 100 μK and have the exact same spectral behavior as the kinematic SZ effect, providing a noise source that is an order of magnitude larger than the signal. However, these fluctuations will be highly coherent over the extent of the cluster, so the pixel-by-pixel component separation will naturally measure this extended emission. At that point, a simple spatial filter can be applied to remove the primary microwave fluctuations. This spatial filter will have the effect of removing roughly half of the cluster kinematic SZ signal

(Holder 2004), thereby reducing the signal-to-noise by approximately this same factor.

Secondary fluctuations will be dominated by kinematic SZ from the quasi-linear regime (the Vishniac effect; Vishniac (1987)) and the thermal SZ background. The kinematic SZ fluctuations are expected to be below the pixel noise, and therefore subdominant, the thermal SZ background will simply add noise to the component that is separated as thermal SZ. The rms is expected to be roughly 10 μK, which will most likely serve as the dominant source of noise for this component. However, this is much smaller than the expected thermal SZ signal from each cluster and should not impact the component separation process at a noticeable level.

Radio point sources that are uncorrelated with galaxy clusters are not a concern (Knox et al. 2004), but radio point sources within galaxy clusters can "fill in" the SZ decrement and severely impact cluster SZ measurements. This is a long-standing concern for low frequency SZ measurements (Moffett & Birkinshaw 1989), and could be a concern even at frequencies as high as 150 GHz. The spectra of radio sources up to such high frequencies are not well known, but very rough estimates can be made of the most likely contamination. Radio surveys at 1.4 GHz have been done of nearby Abell clusters (Ledlow & Owen 1996) and distant X-ray selected clusters (Stocke 1999) that find that a typical galaxy cluster has of order one radio source at 1.4 GHz that would be of order a few mJy at a cosmological distance. Detailed studies of spectra of bright radio sources indicate (Herbig & Readhead 1992) that typical radio sources have spectra that are falling and steepening with frequency. In particular, in their sample they found only a handful of sources that were as bright at 40 GHz as at 1.4 GHz. Most sources with rising spectra at 1.4 GHz eventually turned over and had lower fluxes at 40 GHz than at 1.4 GHz, indicating that studies based on spectral indices at low frequency will not provide accurate estimates of behavior at high frequencies. Assuming that cluster sources have the same spectral behavior and that the steepening at high frequencies continues, this would indicate that only a few percent of clusters will have a radio source contributing of order mJy flux at 150 GHz. In this handful of clusters, radio sources will be a concern, as this flux would be an order of magnitude larger than the pixel noise. However, in the majority of clusters the contamination due to cluster radio galaxies would be comparable to or smaller than the pixel noise.

Infrared point sources, consisting largely of dusty star forming galaxies, are likely to be a major source of contamination (Knox et al. 2004; White & Majumdar 2004). A detailed treatment is beyond the scope of this paper, but the results of Knox et al. (2004) suggest that hot clusters (with temperatures above about 6 keV) will have a large enough SZ signal that the infrared point sources can be estimated simultaneously with the thermal SZ and kinematic SZ signals, assuming an independent measure of the gas temperature. In this work we have found

that the three measurements by an ACT-like experiment provide only two effective constraints, suggesting that there is redundancy in the measurements and that an additional degree of freedom (infrared point sources) could be allowed without significantly degrading the constraints. The surest solution is to use ALMA to measure the relevant point source fluxes. As a point of comparison, ALMA could image 100 square degrees (comparable to the ACT survey area) to a point source sensitivity of 0.1 mJy at 140 GHz in less than 1 month. If one were to instead focus on the inner 2' of the largest 100 galaxy clusters, this would take several hours of observing time. Note that these same observations could be used to estimate the SZ effects, but the small primary beam of ALMA (due to the large telescopes) would require careful mosaicing of the cluster to avoid resolving out much of the cluster flux.

4.9 Discussion and Conclusions

Instruments such as ACT, SPT, APEX, and Planck will find thousands of galaxy clusters in the near future via SZ observations. In addition to determining the number density of clusters, which can put limits on cosmological parameters, these surveys will reveal information about the gas properties of individual clusters. Ideally, SZ observations would be made in at least three frequency bands with one frequency around 300 GHz, one around 150 GHz, and another either near 90 GHz or better yet near 30 GHz. Arcminute-resolution observations at those frequencies with $\simeq 1\mu K$ detector noise would tightly constrain the cluster gas temperature, line-of-sight velocity, and optical depth in the absence of excessive point source and primary microwave background contamination from imperfect subtraction. Without this set of SZ observations, parameter degeneracies prevent disentanglement of these three cluster parameters.

Current limitations in technology and instrument availability will make it impractical to obtain 30 GHz, arcminute-resolution, $1\mu K$ sensitivity, SZ observations of the majority of the clusters that will be found. SZ surveys that will have 90 GHz channels will still have parameter degeneracies resulting from detector noise $\simeq 10\mu K$. However, we find that upcoming SZ surveys will be able to tightly constrain two cluster gas parameters which are linear combinations of τT_e, τv, and τT_e^2. The constrained parameters are roughly τT_e and a single linear combination of the other two terms. We demonstrated that this is the case for both individual isothermal gas regions and for 3D simulated Nbody + hydro clusters.

The SZ intensity shift that microwave photons experience passing through a cluster is nearly a linear function of τT_e, τv, and τT_e^2, these being the most dominant terms in the intensity shift

expression. This near-linearity results in a close correspondence between the two effective parameters SZ surveys will constrain and simple line-of-sight integrals of these parameters through the three dimensional cluster. We illustrated this correspondence with our three dimensional cluster simulations. This will greatly simplify data analysis of multi-frequency SZ data: it will not be necessary (or useful) to model the intensity as a superposition of elements along the line of sight but instead the SZ effect can be modeled as a single gas element with a single effective temperature and velocity.

We have shown that a temperature constraint added to SZ data breaks the parameter degeneracy between τ, $T_{\rm eff}$, and $v_{\rm eff}$. Using the above linearity, we show that the effective velocity constrained by combining SZ with an independent temperature measure is approximately the optical-depth-weighted velocity integrated along the cluster line of sight. Since X-ray derived temperatures do not give us precisely the weighted temperature measurements that are required to determine $\int v d\tau / \int d\tau$ exactly, we find the measured effective velocity will be biased away from $\int v d\tau / \int d\tau$ by about 15 to 40 km/sec, with a smaller bias for hotter, relaxed clusters.

Errors on τ and $v_{\rm eff}$ are calculated via a Markov chain Monte Carlo method assuming a temperature prior in addition to SZ data. We find for ACT-like SZ simulations of our 9 keV cluster, $\sigma_v = 20$ km/sec and $\sigma_\tau = 0.002$ for a 1 keV error on $T_{\rm eff}$, and $\sigma_v = 40$ km/sec and $\sigma_\tau = 0.004$ for a 2 keV error on $T_{\rm eff}$. For our 3 keV simulated cluster, $\sigma_v = 60$ km/sec and $\sigma_\tau = 0.004$, and $\sigma_v = 100$ km/sec and $\sigma_\tau = 0.005$ for 1 keV and 2 keV errors on $T_{\rm eff}$ respectively. The Markov chain errors we find on $v_{\rm eff}$ and τ are smaller than those obtained via a Fisher matrix. A Fisher matrix overestimates the errors because the likelihood surface is strongly curved in this parameter representation, strongly violating the implicit assumption of ellipsoidal symmetry over the parameter region of interest. Note that the errors on velocities will be increased when residual primary microwave contamination is included, and that bulk flows within the clusters provide comparable noise in matching observed peculiar velocities to the true bulk velocity of the cluster (Nagai et al. 2003; Holder 2004; Diaferio et al. 2005).

If an independent cluster temperature estimate from X-ray spectroscopy is unavailable, temperature estimates can also be obtained from either the cluster velocity dispersion (Lubin & Bahcall 1993) or the cluster integrated SZ flux (Benson et al. 2004) and scaling relations. Since an accuracy of only 2 keV is required on an additional temperature measurement to obtain very interesting velocity estimates, the use of these scaling relations could prove to be a very beneficial tool.

As discussed in §4.8, contamination from primary microwave background fluctuations and

point sources add another source of noise that must be factored into these parameter constraints. Radio point sources due to emission from galaxy cluster members themselves and infrared point sources will both be non-negligible sources of SZ signal contamination. Studies of the effect point source contamination will have on cluster parameter extraction have been carried out by Knox et al. (2004) and Aghanim et al. (2004). Both studies have found that the contamination could potentially be serious; however the latter study considers the effect of point source contamination if no attempt is made to filter point sources out of the observations or model them into the parameter extraction routines. Moreover, even in the worst case point source contamination scenario, observations with an instrument such as ALMA will allow straightforward point source subtraction from SZ images. Clearly either filtering techniques or additional ALMA type observations will be needed to minimize both the point source and primary microwave background contamination of SZ signals.

Near-future SZ surveys will open the door to a wealth of information about galaxy clusters. Determining the number density of galaxy clusters as a function of redshift is potentially a strong probe of dark energy's equation of state and variability over time (Haiman et al. 2001; Holder et al. 2001; Hu 2003; Majumdar & Mohr 2003, 2004). However, galaxy clusters offer more information that can also yield cosmological information. The kinematic SZ signature of galaxy clusters can reveal large-scale velocity fields out to high redshift that can provide an alternative probe of large-scale dark matter and dark energy (Peel & Knox 2003). Cluster optical depth information yields cluster gas mass estimates, and optical depths are crucial to any of the tests that have been proposed using the (*extremely* difficult to measure) polarization of scattered microwave photons at the position of galaxy clusters (Kamionkowski & Loeb 1997). The gas parameters T_e, τ, and v of individual galaxy clusters are of direct interest for cluster astrophysics. Arcminute-resolution SZ observations can begin to probe cluster substructure and offer more information about cluster gas profiles and internal gas dynamics. In summary, SZ observations are entering new territory, where large scale surveys will offer new understandings of galaxy clusters and cosmology.

Bibliography

Aghanim, N., Hansen, S. H., Lagache, G. 2004, A&A, in press

Aghanim, N., Hansen, S. H., Pastor, S., & Semikoz, D. V. 2003, JCAP, 5, 6

Bennett, C. L. et al. 2003, ApJS, 148, 97

Benson, B. A., Ade, P. A. R., Bock, J. J., Ganga, K. M., Henson, C. N., Thompson, K. L., Church, S. E. 2004, AJ, 617, 829

Birkinshaw, M. 1999, Physics Reports, 310, 97

Borys, C., Chapman, S., Halpern, M., & Scott, D. 2003, MNRAS, 344, 385

Carlstrom, J. E., Holder, G. P., & Reese, E. D. 2002, ARA&A, 40, 643

Challinor, A., & Lasenby, A. 1998, ApJ, 499, 1.

Christensen, N., & Meyer, R. 2001, PhRvD, 64, 022001

Christensen, N., Meyer, R., Knox, L., & Luey, B. 2001, Classical Quant Grav, 18, 2677

Diaferio, A. et al. 2005, MNRAS, 356, 1477

Dodelson, S. 2003, Modern Cosmology, San Diego, CA: Academic Press

Dolgov, A. D., Hansen, S. H., Pastor, S., & Semikoz, D. V. 2001, ApJ, 554, 74

Gilks, W. R., Richardson, S., & Spiegelhalter, D. J.(Eds.), Markov Chain Monte Carlo in Practice, Boca Raton, FL: Chapman & Hall

Haiman, Z., Mohr, J. J., & Holder, G. P. 2001, ApJ, 553, 545

Hansen, S. H. 2004, MNRAS, 351, L5

Hansen, S. H. 2004, NewA, 9, 279

Hansen, S. H., Pastor, S., & Semikoz, D. V. 2002, ApJ, 573, L69

Herbig, T., & Readhead, A. C. S. 1992, ApJS, 81, 83

Holder, G. P. 2004, ApJ, 602, 18

Holder, G. P., Haiman, Z., & Mohr, J. J. 2001, ApJ, 560, L111

Hu, W. 2004, PhRvD, 67, 081304

Itoh, N., Kohyama, Y., & Nozawa, S. 1998, ApJ, 502, 7

Jackson, J. E. 1991, A User's Guide to Principal Components, New York: John Wiley & Sons Inc.

Kamionkowski, M., & Loeb, A. 1997, PhRvD, 56, 4511

Kosowsky, A. 2003, NewAR, 47, 939

Kosowsky, A., Milosavljevic, M., & Jimenez, R. 2002, PhRvD, 66, 063007

Knox, L., Holder, G. P., & Church, S. E. 2004, ApJ, 612, 96

Kravtsov, A. V. 1999, Ph.D. Thesis

Kravtsov, A. V., Klypin, A., & Hoffman, Y. 2002, ApJ, 571, 563

Ledlow, M. J., & Owen, F. N. 1996, AJ, 112, 9

Lewis, A., & Bridle, S. 2002, PhRvD, 66, 103511

Lubin, L. M., & , Bahcall N. A. 1993, ApJ, 415, L17

Mathiesen, B. F., & Evrard, A. E. 2001, ApJ, 546, 100

Molnar, S. M., & Birkinshaw, M. 1999, ApJ, 523, 78

Majumdar, S., & Mohr, J. J. 2004, ApJ, 613, 41

Majumdar, S., & Mohr, J. J. 2003, ApJ, 585, 603

Moffett, A. T., & Birkinshaw, M. 1989, AJ, 98, 1148

Nagai, D., Kravtsov, A. V., & Kosowsky A 2003, ApJ, 587, 524

Nagai, D., & Kravtsov, A. V. 2003, ApJ, 587, 514

Nozawa, S., Itoh, N., & Kohyama, Y. 1998, ApJ, 508, 17

Peel, A., & Knox, L. 2003, Nuclear Phys B Proc Supp, 124, 83

Pointecouteau, E., Giard, M., & Barret, D. 1998, A&A, 336, 44

Press, W. H, Teukolsky, S. A., Vetterling, W. T., & Flannery, B. P. 1997, Numerical Recipes in C, Second Edition, Cambridge, U. K.: Cambridge University Press

Reese, E. D., Carlstrom, J. E., Joy, M., Mohr, J. J., Grego, L., Holzapfel, W. L. 2002, ApJ, 581, 53

Rephaeli, Y. 1995, ARA&A, 33, 541

Sazonov, S. Y., & Sunyaev, R. A. 1998, ApJ, 508, 1

Sawicki, M., & Webb, T. M. A. 2004, ApJ, in press

Stocke, J. T. et al. 1999, AJ, 117, 1967

Sunyaev, R. A., & Zel'dovich, Y. B. 1970, Comments Astrophys. Space Phys., 2, 66

Sunyaev, R. A., & Zel'dovich, Y. B. 1972, Comments Astrophys. Space Phys., 4, 173

Sunyaev, R. A., & Zel'dovich, Y. B. 1980, ARA& A, 18, 537

Vishniac, E. 1987, ApJ, 322, 597

White, M. & Majumdar, S. 2004, ApJ, 602, 565

Chapter 5
Future Work

In the work described in Chapter 2, an analysis was performed of the expected cluster selection function for an ACT-like millimeter-band survey. This analysis relied on simulations which included the primary microwave background, galactic dust emission, radio and submillimeter galaxies uncorrelated with galaxy clusters, and the SZ signal from galaxy clusters. My future work involves improving these simulations to include the lensing of the microwave background by the intervening matter, the SZ signal from the full density field (not just cluster peaks), and radio and submillimeter galaxies whose clustering properties and correlation with galaxy clusters matches recent radio and submillimeter observations (Lin & Mohr 2007; Righi et al. 2007). These additional physical processes can have a significant effect on cluster mass and selection systematic errors. These new simulations will be run through a software pipeline already developed that simulates the ACT observing conditions and instrument, including realistic beams, detector noise, and atmospheric brightness fluctuations. In this way, one can more accurately test the theoretical predictions depicted in the right panel of Figure 1.2 and realistically evaluate the potential of millimeter surveys of clusters to constrain cosmology via the measurement of structure growth. This will also inform the SZ survey experiments about target signal-to-noise levels, sky area coverage, and additional data sets required to achieve desired dark energy constraints. In addition, this will have enormous value for creating the data reduction and analysis software pipeline through which ACT's actual data will be run.

In Chapter 3, weak-lensing and X-ray mass estimates were compared for four galaxy clusters that comprise the top-ranked shear-selected system in the DLS. X-ray follow-up observations of a larger sample of DLS clusters is in hand, as is deeper X-ray data on the A781 system. My future work will entail performing a similar analysis on this larger sample as well as delving into the details of the A781 system to better understand the robustness of these X-ray and weak-lensing mass estimation techniques. Such understanding, as mentioned above, is vital to efforts to measure cluster number density evolution as a function of cluster mass.

In the previous chapter, results were presented for the expected 1σ statistical errors on cluster peculiar velocities from an ACT-like instrument given ideal observations and a temperature

prior or lower frequency microwave observations. In future work, I aim to determine whether the relatively small errors one can obtain on peculiar velocities given idealized observations still remain when contaminating signals, such as radio and infrared galaxies or strong lensing of the primary microwave background by the galaxy cluster, are also included. Further work is also required to determine the best way of either obtaining a temperature surrogate with the equivalent of $\pm$ 2 keV errors for thousands of clusters or utilizing additional millimeter wavelength data at a fourth frequency band such as SPT will have and can also be provided by APEX or ALMA (Dobbs et al. 2006; Brown et al. 2004). Hopefully, testing these techniques on simulations, including additional possible data sets and all potential sources of systematic error, will yield positive results. If so, these methods can then be applied to the upcoming millimeter-wavelength data from ACT and SPT.

With these efforts and others we will hopefully develop galaxy cluster surveys into powerful probes of the growth of structure in the Universe and thereby learn about the nature of dark energy.

Bibliography

Brown, R. L., Wild, W., & Cunningham, C. 2004, Advances in Space Research, 34, 555

Dobbs, M., et al. 2006, New Astronomy Review, 50, 960

Lin, Y.-T., & Mohr, J. J. 2007, ApJS, 170, 71

Righi, M., Hernandez-Monteagudo, C., & Sunyaev, R. 2007, ArXiv e-prints (arXiv:0707.0288)

Vita

Neelima Sehgal

Education

2000–2008	Rutgers University, New Brunswick, NJ Ph.D. in Physics and Astronomy
1995–1999	Yale University, New Haven, CT B.S. in Physics and Math

Positions Held

2003–2008	Graduate Assistant in Astrophysics Department of Physics & Astronomy - Rutgers, the State University of New Jersey
2000–2003	Graduate Assistant in High Energy Theory Department of Physics & Astronomy - Rutgers, the State University of New Jersey
1999–2000	Research Assistant in Atomic Physics Department of Physics & Astronomy - Yale University
1999–1999	Research Assistant in Solar Physics Solar Physics Department - NASA Goddard

Publications

1. **N. Sehgal**, J. P. Hughes, D. Wittman, V. Margoniner, J. Anthony Tyson, P. Gee, I. dell'Antonio, "Probing the Relation Between X-ray-Derived and Weak-Lensing-Derived Masses for Shear-Selected Galaxy Clusters: I.A781", *The Astrophysical Journal*, (2008) **673**, p 163-175

2. **N. Sehgal**, H. Trac, K. Huffenberger, P. Bode, "Microwave Sky Simulations and Projections for Galaxy Cluster Detection with the Atacama Cosmology Telescope", *The Astrophysical Journal*, (2007) **664**, p 149-161

3. **N. Sehgal**, A. Kosowsky, G. Holder, "Constrained Cluster Parameters from Sunyaev-Zel'dovich Observations", *The Astrophysical Journal*, (2005) **635**, p 22-34

4. L. Ofman, V. M. Nakariakov, **N. Sehgal**, "Dissipation of Slow Magnetosonic Waves in Coronal Plumes", *The Astrophysical Journal*, (2000) **533**, p 1071-1083